Max-Planck-Institut für Extraterrestrische Physik
Garching bei München

NEW CONSTRAINTS ON GAMMA-RAY BURSTS

FRANCESCO BERLATO

Vollständiger Abdruck der von der Fakultät für Physik der Technischen Universiät München zur Erlangung des akademischen Grades eines

Doktors der Naturwissenschaften

genehmigten Dissertation.

Vorsitzender:		Prof. Dr. Alejandro Ibarra
Prüfer der Dissertation:	1.	Priv.-Doz. Dr. Jochen Greiner
	2.	Prof. Dr. Elisa Resconi

Die Dissertation wurde am 02.09.2020 bei der Technischen Universiät München eingereicht und durch die Fakultät für Physik am 12.10.2020 angenommen.

Abstract

Gamma-ray bursts have been one of the prime contenders for the astrophysical neutrinos seen by IceCube, yet counterpart searches were so far unsuccessful. To investigate the lack of detections, this thesis aims to place better constraints on these sources. This is achieved, firstly, by improving the locations, and thus spectral parameters, measured by the Fermi Gamma-ray Burst Monitor, and secondly, by testing the photospheric emission model for GRBs, which is found to perform significantly worse than optically-thin synchrotron emission.

Zusammenfassung

Gammastrahlungsausbrüche waren einer der Hauptkandidaten für die von IceCube detektierten astrophysikalischen Neutrinos, doch die Suche nach elektromagnetischen Gegenstücken war bisher erfolglos. Um diesen Mangel an Detektionen zu untersuchen, zielt diese Arbeit darauf ab, diese Quellen besser einzugrenzen. Hierzu werden erstens die Lokalisierungen und damit auch die spektralen Parameter, die vom Fermi Gamma-ray Burst Monitor gemessen wurden, verbessert und zweitens das photosphärische Emissionsmodel getestet, welches die existierenden Daten deutlich schlechter beschreiben kann als optisch dünne Synchrotronemission.

Contents

Introduction **9**

1 Gamma-ray Bursts **13**
- 1.1 Introduction and history of the observations . . . 13
- 1.2 Observing and localizing GRBs . . . 16
- 1.3 Prompt emission . . . 18
  - 1.3.1 The compactness problem . . . 19
  - 1.3.2 The fireball model . . . 20
  - 1.3.3 Optically thin synchrotron emission . . . 23
  - 1.3.4 Emission from a dissipative photosphere . . . 25
  - 1.3.5 Dissipation mechanisms . . . 27
  - 1.3.6 Polarization . . . 29
- 1.4 Long-wavelength emission following GRBs . . . 30
  - 1.4.1 Afterglow . . . 30
  - 1.4.2 Kilonovae . . . 32
- 1.5 GRBs as multi-messenger sources . . . 32
- 1.6 Tackling the open issues in GRB science . . . 34

2 The Fermi space telescope **35**
- 2.1 Introduction . . . 35
- 2.2 The Large Area Telescope . . . 35
- 2.3 The Gamma-ray Burst Monitor . . . 36

3 Statistics considerata **41**
- 3.1 Introduction . . . 41
- 3.2 χ^2 and Poisson statistics . . . 41
- 3.3 Bayesian approach . . . 42
  - 3.3.1 Model checking . . . 44

4 Improved GRBs localizations **47**
- 4.1 Localizing with GBM . . . 47
- 4.2 BALROG localization performance . . . 49
  - 4.2.1 BALROG localizations with spectral templates . . . 51
- 4.3 Search for systematics . . . 52
  - 4.3.1 Systematics and statistical fluctuations . . . 58
  - 4.3.2 Systematics and size of the error regions . . . 60
- 4.4 Conclusions and further studies . . . 61

5 Test of the photospheric emission model 63
5.1 Introduction 63
5.2 The model 64
5.3 Sample selection and fitting methodology 66
5.4 Fit results 68
5.5 Discussion 76
5.6 Conclusions 81

Conclusions and outlook 83

Appendix A: location tables 85

Appendix B: spectral fit results 87

Appendix C: phase space plots 103

Bibliography 115

Introduction

Since their discovery more than 50 years ago, gamma-ray bursts (or GRBs for short) have been one of the most studied sources in high energy astrophysics, yet they still are one of the most mysterious objects in the Universe. They consist of bright flashes of gamma-rays with durations ranging anywhere from the fraction of a second to several thousands of seconds. As explained in more detail in Chapter 1, GRBs are thought (and to a certain extent confirmed) to be produced by the death of massive stars, either through supernova explosions or merger of compact objects, e.g. neutron stars, in distant galaxies. These progenitors are believed to produce highly relativistic jets, which allow the observation of bursts even at cosmological distances.

Since GRBs can be seen as coming from any direction of the sky at any time in an unpredictable way, this implies that observing them can be quite challenging for non-dedicated instruments, aside from serendipitous detections. In the previous decades various missions specifically designed to observe GRBs have been developed and launched to space, one of those is the still currently operational Fermi Gamma-ray Burst Monitor, GBM (Meegan et al., 2009). This detector is able to perform an almost constant all-sky monitoring, a remarkable achievement which comes however at a price. As explained more in detail in Chapter 2, GBM is not an imaging instrument and is not able to reconstruct separately source's position and spectrum. This has important consequences on how the source reconstruction is carried out, as detailed in Chapter 4, and also means that the process is particularly challenging and that the achieved locations suffer from much larger error regions compared to other types of gamma-ray instruments. The situation is even worse if the source reconstruction method suffers from systematics, as is in fact the case for GBM.

On the other hand, by releasing the constraint of needing to have an all-sky field-of-view, it is possible to design much more performing instruments (at least in terms of localization ability), such as e.g. coded mask detectors. Perhaps the best example of this kind of approach is another dedicated GRB instrument, the *Swift* space telescope. Its gamma-ray coded mask detector, the Burst Alert Telescope, BAT (Barthelmy et al., 2005)), is able to localize GRBs with far greater precision then GBM, at the price of a much smaller field-of-view. Furthermore *Swift* has also at its disposal two additional instruments for follow-up observations, an X-ray telescope, XRT (Burrows et al., 2007), and an optical-UV telescope, UVOT (Roming et al., 2004), making *Swift* a far more versatile instrument.

Yet GBM still holds a unique and fundamental role in modern observations due to its ability of constantly monitoring the entire sky, which is not matched by any other instrument currently operational. No GRB is like another and even a single event can be of extreme scientific relevance, especially now that multi-messenger astronomy is becoming more and more relevant. GBM suffers however from systematics which, as demonstrated in this thesis and also in previous studies (Burgess et al., 2018; Berlato et al., 2019), arise from the use of a wrong reconstruction methodology. This constitutes a serious drawback to the overall performance of the instrument, especially given that the locations provided by GBM are of essential importance for counterpart searches, be it the afterglow (the longer-lasting lower energy emission following a GRB, see Chapter 1) or any possible neutrino or gravitational wave signal. A better localization corresponds to a higher chance of finding counterparts, which will help in better constraining the underlying physics of these objects.

The study of the emission mechanisms producing the GRBs has made great progress in the past couple of decades, thanks to both the improved computational power and the more refined theoretical models. In this regard, the two best candidates to explain the observed GRBs' spectra are emission from either synchrotron (Katz, 1994; Tavani, 1996) or a dissipative photosphere (Pe'er and Ryde, 2017; Beloborodov and Mészáros, 2017). These two models, both detailed in Chapter 1, have been part of a long-standing debate which has yet to produce any conclusive evidence for any of the two to prevail. In fact, both of these models fail to provide the complete picture.

The limitations of the current theoretical models became clear with the observation of GRB 170817A[1], the first simultaneous detection of an electro-magnetic and gravitational signal, generated by a neutron star merger (Goldstein et al., 2017; Abbott et al., 2017). This event confirmed the long-standing theory that at least part of the observed short bursts (that is with duration < 2 s, see Chapter 1) are produced by mergers of neutron stars (Eichler et al., 1989; Narayan et al., 1992). From an observational standpoint, GRB 170817A is a very faint GRB, with a luminosity $\sim$ 1000 times smaller than the weakest short burst detected before then (Bégué et al., 2017). It was observable only due to its extreme proximity, with a redshift of just $z \sim 0.01$, corresponding to about 40 Mpc (Soares-Santos et al., 2017). Its unusual features challenge the conventional picture of GRBs, where the emission is generated by either synchrotron or a dissipative photosphere. Conventionally, the emitted radiation is assumed to be beamed in relativistic jets which allow the burst to be observed even at cosmological distances. It needs however to be noted that, if GRB 170817A was a standard short burst observed off-axis, then both synchrotron and photospheric emission would produce inconsistent results (Bégué et al., 2017), thus strongly hinting that both of these models are most likely still not able to describe the complete picture. The discrepancies could possibly still be accounted for by assuming either more complex emission mechanisms, such as e.g. synchrotron self Compton (Bégué et al., 2017) or through a different structure of the jets, such as the presence of a cocoon surrounding the relativistic jet (Gottlieb et al., 2018; Kasliwal et al., 2017). In fact, recent observation of GRB 190114C (MAGIC Collaboration et al., 2020) further confirmed the existence of a very high energy ($\gtrsim$ 100 GeV) synchrotron self-Compton component during the later stages of the emission. Regardless, GRB 170817A demonstrates that a complete description of GRBs is still far away and that both more observations and improved theoretical models are necessary to achieve a better understanding of the underlying physics.

As such, the scope is of this thesis is two-fold. On one hand it aims to improve the quality of the reconstructed Fermi-GBM GRB locations, increasing thus the chances of successful direct identification of multi-messenger and multi-wavelength signals. On the other hand the thesis also tests the viability of photospheric emission through spectral fitting of the numerical spectra generated by the code developed by Pe'er and Waxman

---

[1] GRBs are commonly identified by a 6 digit number, indicating the year, month and day, following the format YYMMDD. If there's more than a detection in one day, a capital letter (e.g. A,B,C) is appended to the number for each GRB.

(2005), which contributes to better constrain the underlying physics. In particular, the sample utilized is the same as the one in Burgess et al. (2020), where synchrotron is fitted to an extensive sample of GRB spectra, achieving a success rate of $\sim 95\%$. This allows for a direct one to one comparison between the two models.

The thesis is structured in the following way. Chapter 1 provides an overview of the main GRB observables as well as a summary of the relevant physics. Chapter 2 introduces then the instrument and the data products to be used in the following chapters. Chapter 3 and Chapter 4 discuss the statistical and methodological approach to burst localization in GBM, showing how a better fitting algorithm can greatly improve the localization performance of the instrument. Chapter 5 analyzes the viability of the photospheric model through spectral fitting of a sample of GRBs and compares it to the previous results achieved by synchrotron fits. Finally, a summary of the achieved results and a discussion of the possible next steps are given in the conclusions.

Chapter 1

Gamma-ray Bursts

1.1 Introduction and history of the observations

The discovery of GRBs dates back to 1967, when the Vela satellites, detectors developed by the US to monitor possible secret nuclear tests, first saw strong gamma-ray signals coming from the outer space. While many theoretical explanations were proposed for these puzzling signals, due to the poor performance of the gamma-ray detectors available back then, their origin was uncertain. It was in the 90's that the understanding of these sources took a leap forward thanks to newer, more sophisticated instruments being available. The Compton Gamma-ray Observatory, with its dedicated GRB detector BATSE (Burst and Transient Spectrometer Experiment) allowed to establish that these sources are isotropically distributed in the Universe, suggesting that their origin is not in the Milky Way, but in distant galaxies (Meegan et al., 1992). Due to the gamma-ray detectors' limited localization ability, it was initially impossible to obtain a constraining position of a GRB. This implied that redshift measurements were not possible, since one could not correctly identify the host galaxy (that is the galaxy where the object resides) in such a large sky region.

This standstill came to an end in 1997, when the space telescope Beppo-SAX managed to detect GRB 970228 in the X-ray band, finally allowing for a precise location to be obtained. This was also the first time a counterpart to the burst's gamma-rays was detected in another wavelength (Costa et al., 1997). Thanks to the precise position allowed by an X-ray instrument, it was then possible to also find the first optical counterpart and obtain the first ever redshift measurement for a GRB (Metzger et al., 1997). This longer-lasting lower energy emission following the initial gamma-ray release takes the name of *afterglow*. Later observations showed that afterglows can range anywhere from X-rays to radio, with the emission shifting gradually from higher to lower energies with time. On the other hand, the initial gamma-ray emission phase takes the name of *prompt emission*.

Successive optical afterglow detections allowed for more redshift estimates, which further confirmed the hypothesis that GRBs are located in far away galaxies, at cosmological distances. This also implied that the total energy released must have been extremely large: if GRBs were to emit isotropically, this would correspond to energies up to $E_{iso} \sim 10^{55}$ erg, which is roughly on the same order of magnitude of the Sun mass energy. This extreme energetics, which could hardly be explained otherwise, also suggested that the emission needed to be collimated in jets. This hypothesis was later on validated by afterglow observations, which indicated (as will be explained more in detail in Sec. 1.4.1) the presence of jets with opening angles of the order of $\sim 5^{\circ}$ (Harrison et al., 1999; Gehrels and Mészáros, 2012).

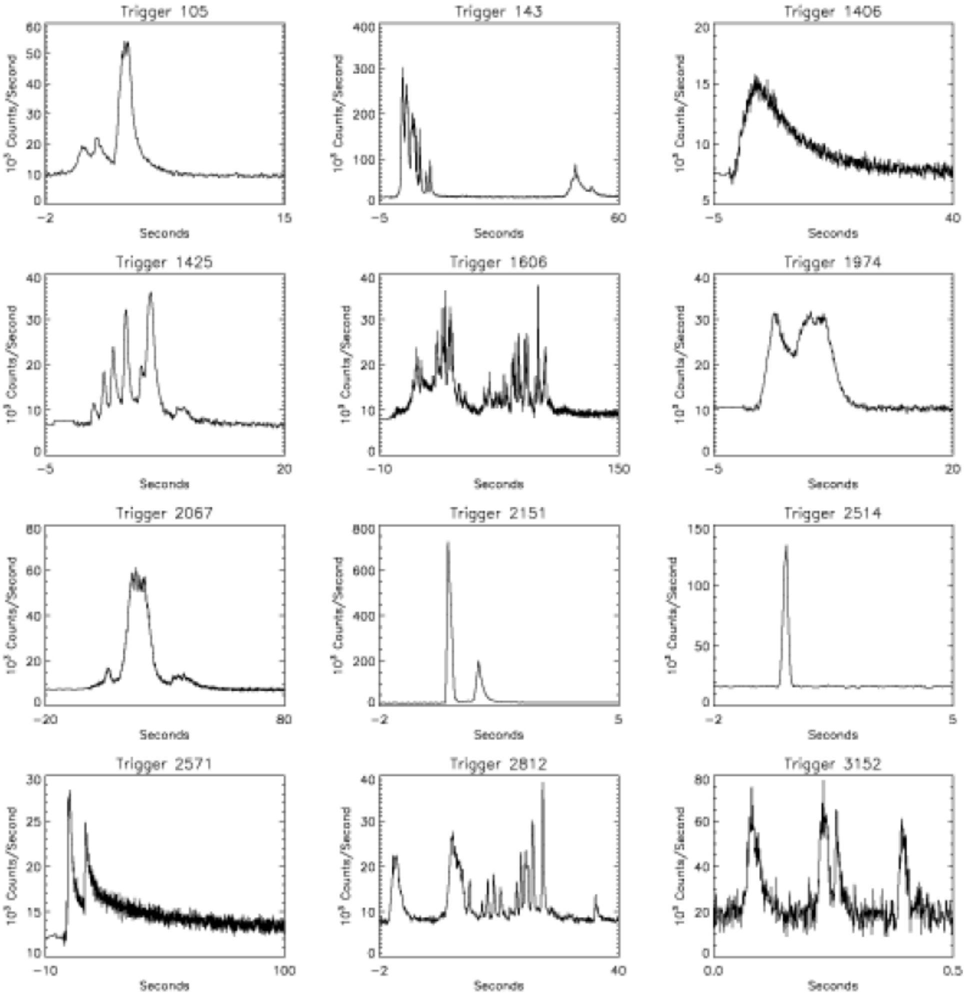

Figure 1.1: Examples of GRB lightcurves from the BATSE detector (Fishman and Meegan, 1995; Mészáros, 2006).

Another peculiarity of GRBs is that they exhibit extreme variability, reaching the millisecond timescales (Golkhou et al., 2015), which implies that the emitting region needs to be very small, of the order of ct_{var}, where c is the speed of light and t_{var} the measured variability timescale. These characteristics indicate that the astrophysical sources producing GRBs need to be associated with compact objects, such as neutron stars or black holes. From an observational standpoint GRBs' lightcurves differ greatly from case to case. They can exhibit a single sharp spike or there can be multiple peaks, which can often partially overlap with each other, as shown in Fig. 1.1. No burst is truly like another, which further complicates the process of understanding the physics behind these objects. GRBs also exhibit a highly varying range of duration timescales, which is usually estimated with the T_{90}, the time interval necessary to accumulate 90% of the burst fluence (i.e. time-integrated photon flux). T_{90} values can range from tens of milliseconds up to several thousands of seconds. Interestingly, the distribution of the T_{90} displays two components (see Fig. 1.2), which suggested that GRBs could be broadly classified as belonging to either one of two different classes, *long* or *short* (Kouveliotou et al., 1993) depending on whether $T_{90} > 2$ s (long) or $T_{90} < 2$ s (short). There is of course some overlapping between the two components of the distribution, as visible in Fig. 1.2, which implies that this classification is somewhat fuzzy.

Regardless, these two subsets of the GRB's population have been associated with two

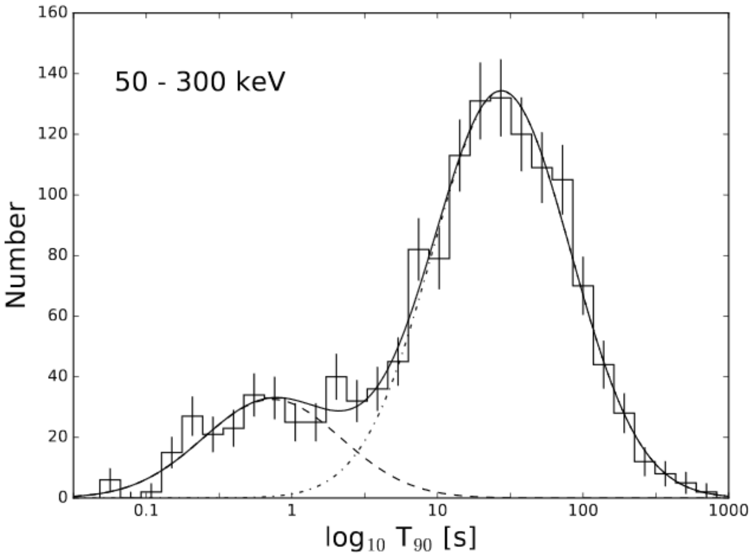

Figure 1.2: The T_{90} distribution from the third Fermi Gamma-ray Burst Monitor catalog (Narayana Bhat et al., 2016).

different types of progenitors, core-collapse supernovae (the so called collapsar or hypernova scenario) for long GRBs and merger of compact objects (either two neutron stars or a neutron star and a black hole) for short GRBs (Eichler et al., 1989). Observations of GRB 980425 and supernova SN 1998bw in the same error region seemed to indicate that long GRBs are produced by particularly energetic supernova events (Galama et al., 1999). Later on, this hypothesis was confirmed with the observation of GRB 030329 and SN 2003dh (Hjorth et al., 2003; Stanek et al., 2003). As for short GRBs, at least a fraction of them were hypothesized to be generated by the merger of two neutron stars (Eichler et al., 1989; Narayan et al., 1992). This event would produce either a black hole directly or an hyper massive neutron star, an unstable system which would collapse to a black hole shortly after its creation. This hypothesis was recently confirmed thanks to the simultaneous observation of GRB 170817 performed by the gravitational wave detectors LIGO/Virgo and the gamma-ray detection from Fermi-GBM (Abbott et al., 2017; Goldstein et al., 2017). Another fraction of the observed short GRBs could also be produced by a neutron star and black hole merger (Mészáros, 2006), though this hypothesis has not yet been confirmed through direct observations. This distinction between the progenitors for long/short bursts is also supported by afterglow observations, which showed that long GRBs are associated with star forming regions, while short bursts are not (Piran, 2004; Mészáros, 2006). This difference can be explained by taking into account the following. Long bursts are thought to be produced directly by the death of massive stars (through core collapse supernovae), which are typically very short-lived. As such, long GRBs are far more likely to take place in galaxies with high star formation rates. Conversely, short GRBs are not produced directly at the moment of the star death, but only when a merger between two compact objects takes place. For this to happen, it is first necessary for the two objects to lose angular momentum through emission of gravitational waves, which allows them to gradually get closer to each other, until they finally merge and the short burst can take place.

It should also be noted that current findings have proven that the long/short classification does not capture the complete picture of the GRB population. Most notable is the case of ultra-long GRBs (Levan et al., 2014), which are bursts with durations $\gtrsim 10^3$ s, with typical T_{90} values of a few thousands of seconds. This GRBs are very rare and are thought to originate from different progenitors than the long and short ones. Possible candidates are accretion from the envelope of very large progenitor stars (such as blue supergiants), tidal disruption events due to black-holes destroying e.g. a white dwarf, or the formation of a magnetar, a neutron with extremely strong magnetic fields of the order of $B \sim 10^{15}$ G, see e.g. Greiner et al. (2015).

As a final remark, it needs to be pointed out that there exists a class of sources with GRB-like features, known as X-ray flashes (XRFs), but which emission peaks in the X-rays instead of the gamma-rays. They are thought to constitute an extensions of the GRB population, though it is not completely clear whether the differences are purely spectral (less energetic emission), geometric (higher redshift, larger viewing angle) or a combination of the two (Heise et al., 2001).

1.2 Observing and localizing GRBs

Due to being short-lived transients, GRBs are very challenging sources to observe. They can appear at any point in time in any region of the sky in a unpredictable manner. To detect and study them, during the past decades various dedicated detectors have been designed and launched to space. This section presents an overview of the current main instruments and detection methods, with a particular focus on the localization aspect.

The two main currently operational GRB instruments are the *Swift* space telescope and the Gamma-ray Burst Monitor on-board the Fermi spacecraft. Aside these two, there are also other high energy detectors which observe bursts more or less frequently, such as KONUS, the Fermi-LAT or INTEGRAL for example. While *Swift* and GBM are both dedicated GRB instruments, the approach they take to observation is radically different, as explained in this section.

The *Swift* space telescope is composed of three different instruments, a coded aperture gamma-ray detector (BAT), a X-ray telescope (XRT) and an optical-ultraviolet telescope (UVOT). While XRT and UVOT are very useful instruments for follow-up observations, only BAT can detect the initial gamma-ray emission of the burst, thanks to its large field-of-view of 1.4 sr (Barthelmy et al., 2005). BAT is a coded aperture telescope, which implies that the actual detector is located behind a mask, that is a layer of high density material with holes shaped in a known pattern. The mask casts a shadow by letting only the photons passing through the holes reach the detector, as shown in Fig. 1.3. The shadow's shape depends on the position of the source relative to the spacecraft and can be used, through specific algorithms, to reconstruct the object position. Note that this implies that BAT's field-of-view is always partially occulted by its own mask. However, one major limitation of this method is that is works only for soft gamma-rays, since it is impossible to completely absorb higher energy photons with a mask of reasonable thickness.

Nonetheless BAT is able to achieve remarkably precise position for a gamma-ray instrument, with uncertainties of the order of a few arcminutes (Barthelmy et al., 2005). This first localization can also be used for follow-up observations by the other two instruments, XRT and UVOT. Overall *Swift* is able to detect and localize ~ 90 bursts per year, which allows ground-based observers to measure a redshift in about 30% of the cases (see https://swift.gsfc.nasa.gov/archive/grb_table/).

On the other hand, GBM adopts a completely different approach to detection. Instead of using a coded aperture telescope, it relies on having a multitude of scintillation de-

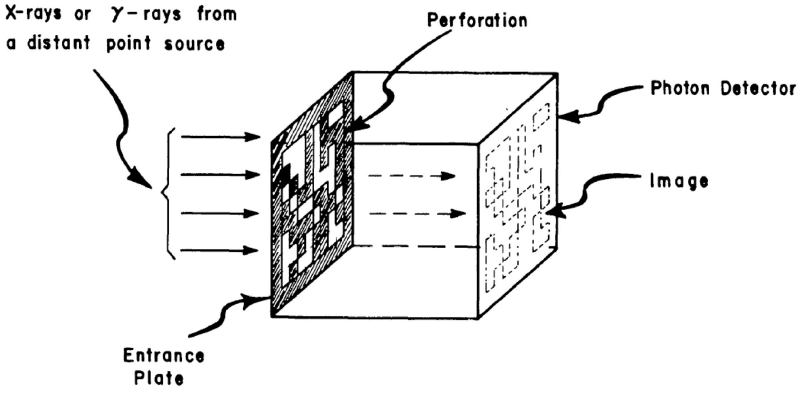

Figure 1.3: A diagram showing the basic structure of a coded aperture detector (Dicke, 1968).

tectors mounted around the Fermi spacecraft (Meegan et al., 2009). This allows GBM to achieve an all-sky field-of-view (minus the region occulted by the Earth), potentially being able to detect GRBs from any direction. In practice, this allows the instrument to observe $\sim$ 240 bursts per year, which makes GBM the most prolific GRB detector in history with its twelve years of operation. While a more detailed explanation of the instrument is given in Chapter 2, to briefly summarize, the measurement process in GBM consists in measuring count rates (which are proportional to the photon flux) in each of the detectors and energy channels. These counts depend simultaneously on both the source's spectrum and position relative to them, which implies that GBM is not able to generate images of sources (at least not in a conventional way). The localization is instead performed through a "comparison" of the rates measured in the different detectors. This approach to burst detection has both advantages and disadvantages if compared to *Swift*'s. On one hand GBM achieves an all-sky field-of-view, on the other this comes at the price of a much worse precision (i.e. larger errors) for the obtained position compared to *Swift*'s, with uncertainties typically of the order of a few degrees. Additionally it must be noted that the energy window of the two instruments is not the same, with *Swift*/BAT being able to observe only up to 300 keV compared to the $\sim$ 40 MeV of GBM, which however has no ability to do follow-up X-ray/optical observations.

An alternative localization method is provided by the *Interplanetary Network* (IPN) through triangulation. When different space missions are able to detect the same GRB, it is possible to use the difference in arrival times of the signal to perform a triangulation and locate the source, but for that to be possible the different spacecrafts need to be located far enough from each other. Part of the IPN are, among the others, Fermi, *Swift*, INTEGRAL and KONUS. The triangulated position's precision depends on many factors, but of primary importance are the number of detectors and their relative distance to each other. On the other hand, since the triangulation method relies solely on the difference of arrival times of the signal in different instruments, as long as the detectors are sensitive enough to detect a signal above the background their independent ability to localize the burst does not matter. It is necessary to have at least two instruments to perform a triangulation, though the resulting error region is usually not very constraining in that case, see e.g. Fig 1.4. With three or more detectors the IPN triangulation is typically much more constraining than the GBM's positions. For a more detailed explanation of the triangulation method, refer to Hurley et al. (2013).

There are of course other instruments and methods of detection available, but they are usually less reliable or consistent. For example, the Fermi-LAT is potentially able to

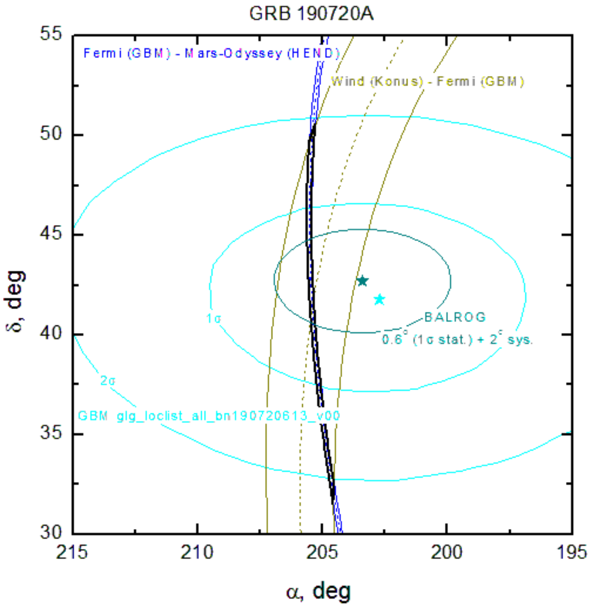

Figure 1.4: An example of IPN triangulation for GRB 190415A (Svinkin, Dmitry). In this particular case, the burst was detected by Fermi-GBM, KONUS and Mars-Odyssey. The blue and brown circles correspond to the sky regions which the different detector combinations are able to delimit. The overall 68% probability region corresponds to the area defined by the black lines. The cyan and dark green circles correspond to GBM-only localizations performed with two different algorithms (more on that in Chapter 4)

.

detect high energy photons emitted from GRBs, but due to the bursts' photon flux being much weaker at higher energies and the instrument's smaller field-of-view, it is able to observe GRBs only in a small fraction of cases. To put the numbers into perspective the LAT detected 186 bursts in its first 10 years of operation (Ajello et al., 2019), less than 8% of what GBM managed to observe in the same time interval, with its 2385 GRBs detected (see https://fermi.gsfc.nasa.gov/ssc/data/access/gbm/). That of course doesn't imply that detections by other non-dedicated instruments aren't important for other uses aside localization, such as spectral fitting, but shows how challenging it is to consistently detect and localize GRBs unless dedicated detectors are available. Ultimately all methods and instruments here presented have their own advantages and shortcomings and this proves how important it is to have simultaneous observations of the same burst as often as possible, so to obtain the maximum amount of information from each event.

1.3 Prompt emission

The term prompt emission refers to the initial release of gamma-rays from a GRB. During the last few decades its understanding has advanced greatly, thanks to both better instruments and more refined theoretical models, however a clear and complete description is still far from being achieved. It is known that at the origin of the emission is the formation of a compact object, either through a core-collapse supernova or a merger of neutron stars, or possibly of a neutron star and a black hole too (Mészáros, 2006). Regardless of the specific progenitor, during the event gravitational energy is converted to radiation, mostly gravitational waves and neutrinos plus a much smaller (10^{-2} – 10^{-3} of the total energy released) electro-magnetic component through the gamma-rays (Mészáros, 2006).

The observed gamma-ray spectrum peaks in the energy region comprised from a few tens of keV up to a few MeV. There are currently no models based on a single emission mechanism (e.g. synchrotron) which can explain the entirety of the observed GRBs. As such, it has been common practice to use empirical functions for spectral fitting instead, the most popular one being the *Band function* (Band et al., 1993), which is defined as follows

$$F(E) = A \begin{cases} \left(\frac{E}{E_{piv}}\right)^{\alpha} e^{-\frac{E}{E_b}} & \text{if } E \leq (\alpha-\beta)E_b \\ \left(\frac{E}{E_{piv}}\right)^{\beta} e^{\beta-\alpha} \left(\frac{(\alpha-\beta)E_b}{E_{piv}}\right)^{\alpha-\beta} & \text{if } E > (\alpha-\beta)E_b \end{cases} \tag{1.1}$$

where F is the differential flux (i.e. the number of photons per unit of energy, time and area), A is the amplitude of the function at 100 keV, α and β are respectively the low and high energy indices, E_b is the break energy (which sets the position of the peak, $E_{peak} = (2+\alpha)E_b$) and E_{piv} is the pivot energy (usually fixed to 100 keV), which just sets the reference value for A. The Band function is essentially a power-law with an exponential cut-off at lower energies which is then smoothly connected to a power-law higher energy component. While there is no underlying physical process in the definition of the Band function, it has often been used as a proxy to test the viability of emission models, particularly for the case of synchrotron emission, as described later in Sec. 1.3.3.

The following sections provide a summary of the current state of knowledge of the prompt emission, from the generally accepted elements to the more uncertain and still currently debated aspects of the emission.

1.3.1 The compactness problem

One of the most important characteristics of the prompt emission is that it exhibits non-thermal features, i.e. it is not compatible with a simple blackbody spectrum. On the other hand, a naive calculation (neglecting redshift corrections, which are of the order of a few) of the optical depth would produce extremely large values, i.e. the photons scatter many times before being released. This would imply that the radiation reaches thermal equilibrium and that the spectrum should be approximately thermal, in stark contrast with the observations. This generates an apparent paradox known as the *compactness problem*, which, as shown here, can be solved by the presence of relativistic motion.

In the source's frame, photons can produce pairs through $\gamma\gamma \rightarrow e^+e^-$ if they satisfy (neglecting an angular factor) the condition $\sqrt{E_1E_2} > m_ec^2$, where $E_{1,2}$ are the photons' energies and m_e the electron mass (Piran, 1999). The pair production optical depth is then given by the following equation (Piran, 1999)

$$\tau_{\gamma\gamma} = \frac{f_p\sigma_T F D^2}{R^2 m_e c^2} \tag{1.2}$$

where f_p is the fraction of the photon pairs meeting the energy requirement, σ_T is the Thomson cross-section, F is the observed fluence, D the distance of the source and $R \sim ct_{var}$ is the size of the emitting region. Using typical values one finds that $\tau_{\gamma\gamma} \sim 10^{13}$. This extremely large optical depth would imply that pairs are copiously produced and these particles can then Compton scatter with the lower energy photons, ending up greatly increasing the overall optical depth. In that case, thermal equilibrium should be quickly reached and the GRB spectra would be a blackbody, thus in conflict with the data from observations. The solution of this apparent paradox lies in the presence of relativistic motion. If the emitting region is moving at relativistic speeds towards the observer, two corrections come into play in Eq. 1.2. First, due to blueshifting, the fraction of photons meeting the energy requirement in the source frame is actually much lower than what initially inferred from the observations. The correction takes the form of $f_p \to \Gamma^{-2\alpha} f_p$, with Γ Lorentz factor and α high energy spectral index of the observed photons. Second, the size of the emitting region as inferred from the variability is wrong, and is instead $R \to \Gamma^2 R$. Overall, the previous estimate of the optical depth changes as $\tau_{\gamma\gamma} \to \Gamma^{-(4+2\alpha)}\tau_{\gamma\gamma}$. To observe a non-thermal spectra, the optical depth needs to be $\tau_{\gamma\gamma} \lesssim 1$, which implies typical values for the Lorentz factors of $\Gamma \gtrsim 100$ (Piran, 1999). Relativistic motion is thus able to solve the compactness problem and explain the presence of non-thermal spectral features in a self-consistent way.

1.3.2 The fireball model

The most widely accepted physical model used to describe emission from GRBs is the *fireball model* (Paczynski, 1986; Goodman, 1986). It is based on the idea that, with the formation of the compact object (regardless of the specific mechanism generating it), an energy of the order of few solar masses is released in a timescale which can be as short as a few milliseconds (Piran, 2004; Mészáros, 2006). In the process, gravitational energy is converted to radiation, mostly gravitational waves in the frequency range $10^2 - 10^3$ Hz and electron neutrinos with typical energies of $10 - 30$ MeV, plus a smaller ($10^{-3} - 10^{-2}$ of the total energy released) electro-magnetic component (Mészáros, 2006). The resulting outflow forms a so-called *fireball*, which is a rapidly expanding ejecta composed by a plasma of baryons, e^+e^- pairs and photons, most likely also containing a significant amount of magnetic field energy (Mészáros, 2006). The fact that the fireball needs to be expanding can be deduced from the observations, which imply a luminosity greatly exceeding Eddington's limit, $L_E = 4\pi GMm_pc/\sigma_T$. This value sets the maximum luminosity a gravitationally bound object can reach before its own radiation pressure causes it to expand and lose mass through some wind or outflow.

Due to the fireball's large initial optical depth, the photons cannot escape and the outflow expands adiabatically. Particles are accelerated until they reach a maximum Lorentz factor determined by the initial random internal energy per particle, also known as *entropy*, $\Gamma_{max} \equiv \eta = E_0/M_0c^2$ with M_0 mass of the ejecta (Mészáros, 2006). The radius at which this occurs is known as the *saturation radius* r_s and beyond this point the Lorentz factor does not increase anymore due to the fact there's no more energy to convert. Note that the ejecta can reach the value defined by η only if the fireball is still optically thick at the saturation radius, otherwise the the photons would escape too soon and the acceleration process would come to a halt prematurely.

Moreover the fireball, due to the reasons detailed in Sec. 1.3.1, needs to be expanding relativistically. This has important implications on the baryon content (also called *baryon load*) of the outflow. Since even very small number densities of baryons will end up dominating the mass of the ejecta, the baryon load cannot be too large. If that was not the case, then the outflow would become too "heavy" and the fireball would not be able to reach relativistic speeds, in contrast with what required by the observations.

The relativistic fireball is initially transparent only to gravitational waves, but as it expands it quickly also becomes transparent to neutrinos first and later on to photons too. While the fireball model itself makes no prediction regarding the angular distribution of the ejecta, simple arguments regarding the overall energetics already suggest that the emission is beamed into relativistic jets (Piran, 2004). Compared to a spherically symmetric scenario, this allows to lower the overall energy required by the explosion by a factor of $\sim \theta_{jet}^2/2$, assuming two relativistic jets with small aperture angle θ_{jet}. Note however that due to relativistic beaming even with a spherically symmetric outflow, only radiation

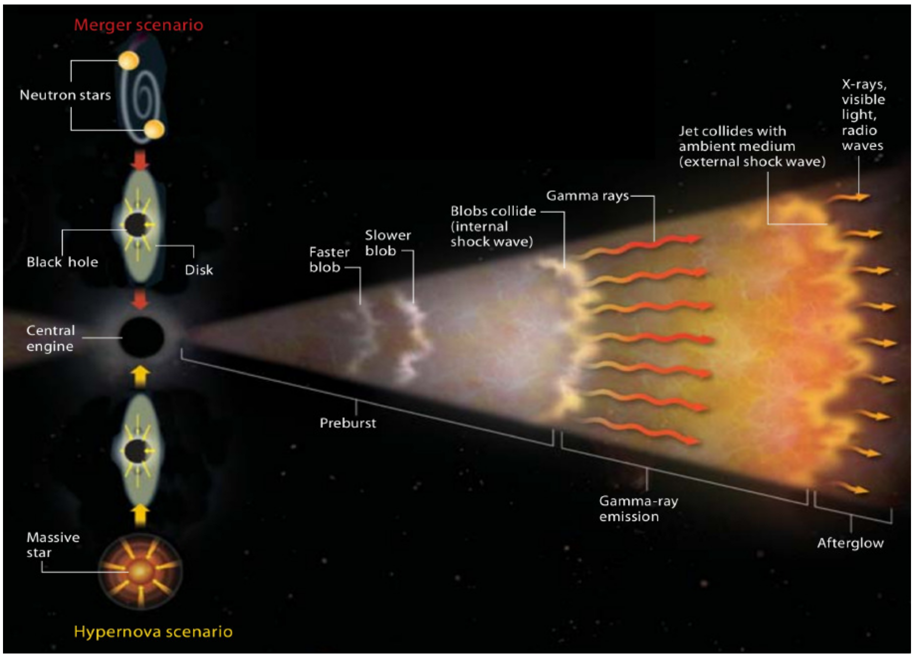
Merger scenario
Neutron stars
Black hole
Disk
Central engine
Massive star
Hypernova scenario
Faster blob
Slower blob
Blobs collide (internal shock wave)
Gamma rays
Jet collides with ambient medium (external shock wave)
X-rays, visible light, radio waves
Preburst
Gamma-ray emission
Afterglow

Figure 1.5: A schematic of a GRB. Credit: NASA.

emitted within an angle $\sim 1/\Gamma$ is visible to the observer. As detailed later on in Sec. 1.4.1, the jet scenario is further confirmed by afterglow observations, which lightcurves display typical changes in the slope known as *jet breaks*. These occur whenever the Lorentz factor decreases enough to enable the observer to see the entirety of the jet, $1/\Gamma \sim \theta_{jet}$. From this point onwards, since the jet is already fully visible, a further decrease in Lorentz factor won't contribute to increase the observable emitting surface. Thus, from afterglows' observations, typical jet angle values of $5-10°$ are estimated (Beloborodov and Mészáros, 2017).

What is however highly uncertain is the structure itself of the jets, which are often simply assumed to be uniform within their aperture angle, with the burst having then negligible off-axis emission. This is the scenario described by the so-called *top-hat* model. On the other hand, if the jets have any kind of non-uniform angular profile (e.g. power-law or gaussian), they are said to be *structured*. In general the structure of the jets is still not very well understood, especially because it is very hard to disentangle the geometrical dependence from the spectral dependence in the prompt emission.

The presence of jets also implies that, unless the burst is located at extremely small redshifts (in which case off-axis emission may be observable), it will be detected only if seen on-axis, that is the angle between the line-of-sight and the jet is $\theta \lesssim \theta_{jet}$. The observer thus sees the radiation emitted by the fireball as blueshifted due to the outflow moving in its direction, which also increases the apparent brightness of the object. In general, if the jet is observed at an angle θ, the Doppler factor of the emitted radiation is (neglecting redshift corrections)

$$D = [\Gamma(1-\beta\cos\theta)]^{-1} \tag{1.3}$$

where Γ is the Lorentz factor of the relativistic shell and β is its speed divided by c. In the simplest case, $\theta \sim 0$ and $\Gamma \gg 1$ (i.e. an ultra-relativistic jet pointing straight into the observer), the Doppler factor is $D \sim 2\Gamma$.

The fireball is assumed to start expanding from a generic radius r_0, which represents the size of the inner engine. This expansion is initially adiabatic due to the very large optical depth of the plasma. The fireball pressure is dominated by radiation, which can be described as a gas with adiabatic index $p = 4/3$ (Mészáros, 2006). Taking thus into account that energy and entropy are conserved during this first phase, it's easy to show that the Lorentz factor of the fireball grows linearly until reaching the value defined by the entropy, η, at the saturation radius r_s, that is

$$\Gamma(r) = \begin{cases} \frac{r}{r_0} & \text{for } r \leq r_s \\ \eta & \text{for } r > r_s \end{cases} \tag{1.4}$$

Note that this equation holds under the assumption of the fireball remaining optically thick at least until r_s. In the opposite case, the photons would escape too soon and the acceleration process would come to a halt (Pe'er, 2015). In the same way, it is possible to derive a law for the evolution of the temperature of the fireball in the observer frame (Pe'er, 2015):

$$T_{obs}(r) = \begin{cases} T_0 & \text{for } r \leq r_s \\ T_0 \left(\frac{r}{r_s}\right)^{-\frac{2}{3}} & \text{for } r > r_s \end{cases} \tag{1.5}$$

where $T_0 = \left(\frac{L}{4\pi r_0^2 ac}\right)^{\frac{1}{4}}$ is the temperature at the base of the fireball, with L being the luminosity of the fireball and a being the Stefan constant. Once again, this relation only holds as long as the fireball is optically thick.

As the fireball expands, its Thomson scatter optical depth τ decreases until the outflow eventually becomes transparent, i.e. the photons are able to escape. The surface where this happens, conventionally defined by $\tau = 1$, takes the name of *photosphere*. To find the radius of the photosphere r_{ph}, one can solve the following equation for the Thomson optical depth

$$\int_{r_{ph}}^{\infty} n_e \sigma_T \Gamma(1-\beta) dr \simeq n_e \sigma_T \frac{r_{ph}}{2\Gamma} \tag{1.6}$$

where n_e is the electron density, σ_T is the Thomson cross-section and it was made use of the approximation $1 - \beta \simeq \frac{1}{2\Gamma}$ for $\Gamma \gg 1$. If n_e is equal to the baryon density (which is equivalent to assuming that the baryon content is dominated by protons), given by $n_p = L/(4\pi r^2 m_p c^3 \eta \Gamma)$, the photospheric radius is then given by (Pe'er, 2015)

$$r_{ph} = \frac{L\sigma_T}{8\pi m_p c^3 \eta \Gamma^2} \tag{1.7}$$

where, past the saturation radius r_s, $\Gamma \equiv \eta$. Note however that strictly speaking the value of r_{ph} provided by Eq. 1.7 is valid only for on-axis (with respect to the observer) emission. Photons seen as coming from an angle follow a different optical path and this implies that the value of the photospheric radius changes with the angle (Pe'er, 2015).

Since photons cannot escape before reaching the photosphere, it could naively be expected that the spectrum emitted by a fireball would be described by a blackbody distribution, since radiation should have had the time to achieve thermal equilibrium. This however does not match the strongly non-thermal features present in the observations. To achieve such spectra, there is the need for one additional element to the model, which is the presence of a *dissipation mechanism*, that is some kind of physical process able to accelerate particles and produce the observed non-thermal features. The fireball model itself does not specify which mechanism is exactly at work in the ejecta and, depending on which energy form is dominating the outflow (i.e. kinetic or magnetic) there are different possible candidates, outlined in Sec. 1.3.5.

1.3.3 Optically thin synchrotron emission

One of the simplest, yet physically motivated models used to explain GRBs' spectra is synchrotron emission, that is the radiation emitted by charged particles (in particular electrons) accelerated to relativistic speeds in a magnetic field. Synchrotron could in principle produce the observed non-thermal spectra, although the emission needs to take place in an optically thin region, otherwise the photons would be absorbed/scattered and the spectrum would no longer be described by pure synchrotron. For a single particle, the power of the emitted radiation in the local frame is given by the following equation (Dermer and Menon, 2009)

$$P_{syn} = \frac{16\pi}{3}\left(\frac{q^2}{mc^2}\right)^2\left(\frac{B^2}{8\pi}\right)c\beta_{par}^2\gamma_e^2\sin^2\psi \tag{1.8}$$

where q is the charge of the particle, m its mass, c the speed of light, B the magnetic field, β_{par} the speed of the particle (divided by c) along the direction of the magnetic field, γ is the Lorentz factor of the particle and ψ is the pitch angle (i.e. the angle between the particle velocity vector and the magnetic field). In practice, in an astrophysical plasma, emission is dominated by electrons due to the dependence of the power on the inverse of the squared mass $P_{syn} \propto m^{-2}$. Assuming that in the local frame the pitch angle distribution is isotropic, the $\sin^2\psi$ factor is averaged to $2/3$. Furthermore, if $\gamma_e \gg 1$ for the electrons, it is possible to rewrite Eq. 1.8 into

$$P_{syn} = \frac{4}{3}c\sigma_T U_B\gamma_e^2 \tag{1.9}$$

where $\sigma_T = \frac{8\pi}{3}\left(\frac{q^2}{mc^2}\right)^2$ is the Thomson scattering cross-section and $U_B = \frac{B^2}{8\pi}$ is the energy density associated to the magnetic field. To compute the power emitted in the observer frame P_{obs}, it is necessary to correct for the relativistic effects by multiplying Eq. 1.9 by Γ^2, the square of the bulk Lorentz factor of the ejecta. For a single electron, the characteristic observer energy of the synchrotron photon is

$$E_{peak} = \frac{\hbar q_e B}{m_e c}\gamma_e^2\Gamma \tag{1.10}$$

which depends linearly on both Γ and B. It is possible to associate a cooling timescale to synchrotron emission (Piran, 2004), which, in the fluid frame, is simply given by the ratio between the total particle energy and the power of the emitted radiation

$$t_{syn} = \frac{\gamma_e m_e c^2}{P_{syn}} = \frac{3m_e c}{4\sigma_T U_B\gamma_e\Gamma} \tag{1.11}$$

which is thus dependent on the photon energy, $t_{syn} \propto E^{-\frac{1}{2}}$. This sets a limit to the variability for optically thin synchrotron, since the observed lightcurves cannot include peaks of shorter duration than t_{syn} (Piran, 2004). This is of course valid only for a single electron, whereas in a realistic scenario one needs to consider an electron distribution in terms of γ and integrate over it to calculate the overall emitted spectrum. This distribution is usually assumed to be a power-law $\frac{dN_e}{d\gamma} \propto \gamma^{-p}$, comprised between a minimum γ_{min} and a maximum $\gamma_{max} \gg \gamma_{min}$ Lorentz factor. The assumption of a power-law may seem arbitrary,

but it is in reality very loose, since various different physical processes are able to generate such distribution, such as Fermi acceleration or magnetic reconnection (Piran, 2004; Dermer and Menon, 2009; Sironi and Spitkovsky, 2014). If no cut-off γ_{max} is assumed, the power-law index needs to be $p > 2$ in order for the energy not to diverge. Note that, from a physical standpoint particles cannot reach arbitrarily large values of γ, since at some point they will be cooling as fast as they are being accelerated. It can be shown however that typical values of γ_{max} are extremely large and do not realistically impact the power-law approximation (Piran, 2004).
To compute the spectrum emitted by a distribution of electrons, it is necessary to know how much energy is present in both particles and magnetic field. While ideally this should predicted by a model on the basis of physical principles, in practice this is most often not feasible. Thus the two microphysical parameters ϵ_e and ϵ_B are introduced to quantify the fraction of the energy contained respectively in the electrons and in the magnetic field:

$$\begin{aligned}\epsilon_e &= \frac{U_e}{U} \\ \epsilon_B &= \frac{U_B}{U} = \frac{B^2}{8\pi U}\end{aligned} \tag{1.12}$$

where U is the total thermal energy density. From these two parameters it is possible to derive both the magnetic field B and the minimum Lorentz factor of the electron distribution, $\gamma_{min} \simeq \epsilon_e \frac{m_p}{m_e} \frac{p-2}{p-1}$ (Pe'er, 2015). γ_{min} is of particular importance because it specifies where, in terms of energy, most of the electrons are. Since most of the electrons have γ_e values close to γ_{min}, this defines the typical energy of the emitted photons (Piran, 2004). In fact, synchrotron exhibits two distinct cooling regimes (Sari et al., 1998a; Piran, 2004), depending on whether the electrons are losing a significant fraction of their energy due to the synchrotron emission during the timescale set by the hydrodynamics of the outflow, t_{hyd}. These two regimes are named *fast* and *slow* cooling (Sari et al., 1998b). The critical value separating the two is given by Eq. 1.13

$$\gamma_c = \frac{3 m_e c}{4 \sigma_T U_B \Gamma t_{hyd}} \tag{1.13}$$

which is the Lorentz factor of an electron cooling on the hydrodynamical timescale, obtained by imposing $t_{syn} = t_{hyd}$ (Piran, 2004). In the fast cooling regime $\gamma_c < \gamma_{min}$ and all electrons cool quickly. Conversely, in the slow cooling scenario $\gamma_c > \gamma_{min}$ and only the high energy tail of the electrons' ($\gamma_e > \gamma_c$) distribution cools (Piran, 2004), which implies that slow cooling is a less efficient regime, since the bulk of the electron population $\gamma_e \sim \gamma_{min}$ does not cool (Piran, 2004).

It can be shown that these two cooling regimes correspond to different spectral slopes at lower energies. In particular, the maximum value of the slope of the spectrum is $-3/2$ for fast cooling and $-2/3$ for slow cooling. This gave rise already in the 90's to the so-called "line-of-death" problem (Preece et al., 1998), when the low energy slope of many GRB spectra was found to be incompatible with synchrotron emission. Until recent times however synchrotron was not being tested by fitting it directly to the data, but simply by comparing the spectral slopes computed through empirical function fits (such as the Band function) to the range of values allowed by optically thin synchrotron. This method was proven to produce inaccurate results in Burgess et al. (2020), where a direct synchrotron fit to a large sample of GRB spectra resulted a 95% acceptance rate for the model.

As an additional remark, it's also possible that some physical effects may be distorting the synchrotron spectral shape. One of these, for example, is *jitter radiation*, which

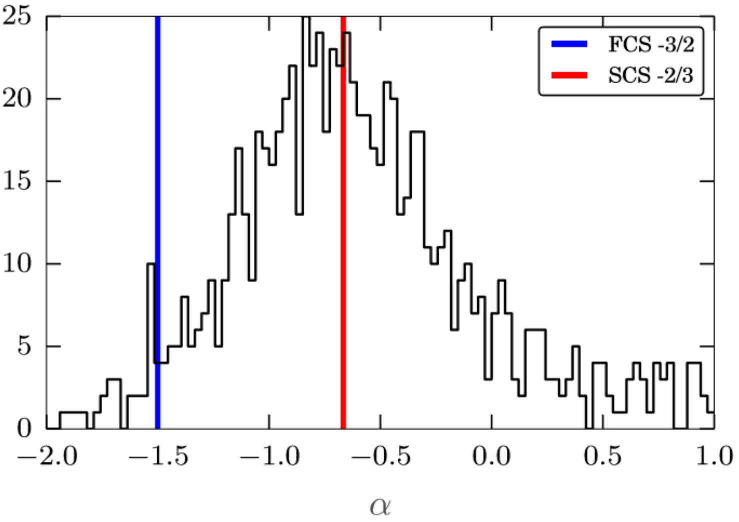

Figure 1.6: The distribution of the Band function's low energy index α for a sample of Fermi-GBM GRBs. The colored lines denote the position of the limits for fast cooling synchrotron (FCS, in blue) and slow cooling synchrotron (SCS, in red). Figure from Burgess et al. (2015).

occurs when the magnetic field is highly non-uniform, i.e. the magnetic field changes significantly on a scale smaller than the Larmor radius of the emitting electrons (Medvedev, 2000).

1.3.4 Emission from a dissipative photosphere

Photospheric emission, in its simplest implementation, corresponds to a purely thermal spectrum emitted by the fireball at the photosphere, where the outflow becomes transparent and radiation can escape. In this case the spectral shape is completely defined by the temperature of the plasma at the photosphere, which is given by substituting $r = r_{ph}$ in Eq. 1.5 (Pe'er, 2015):

$$T_{ph} = T_0 \left(\frac{r_{ph}}{r_s} \right)^{-\frac{2}{3}} \tag{1.14}$$

valid under the assumption of $r_s < r_{ph}$. The observed luminosity of the thermal component is then given by $L_{th}^{obs} = \Gamma^2 4\pi r_{ph}^2 \sigma T_{ph}^4 \propto L^{\frac{1}{3}} \Gamma^{\frac{8}{3}} r_0^{\frac{2}{3}}$, where σ is the Stefan-Boltzmann constant and the factor Γ^2 is meant to take into account relativistic beaming.
Observations have however long ruled out a pure blackbody spectrum, which implies that either the thermal component is sub-dominant (i.e. other mechanisms such as synchrotron dominate the emission) or heavily modified by some other physical processes. The latter case is the scenario described by the so-called *dissipative photosphere* models, which could in principle be able to reproduce the observed non-thermal spectra. These models are typically very complex and try to include all of the relevant physical interactions taking place in the relativistic outflow. These normally include all electron/photon processes, such as Compton scattering, pair production/annihilation, synchrotron emission and self-absorption etc., see e.g. Fig 1.7. Some implementations of the dissipative photosphere also take into account proton-neutron interactions, which may play an important role in the generation of the observed spectrum (Vurm and Beloborodov, 2016).

It should be noted however that even without the aforementioned dissipative processes, the spectral component produced by the photosphere is expected to deviate from a pure thermal distribution to some extent. Some broadening of the blackbody component can

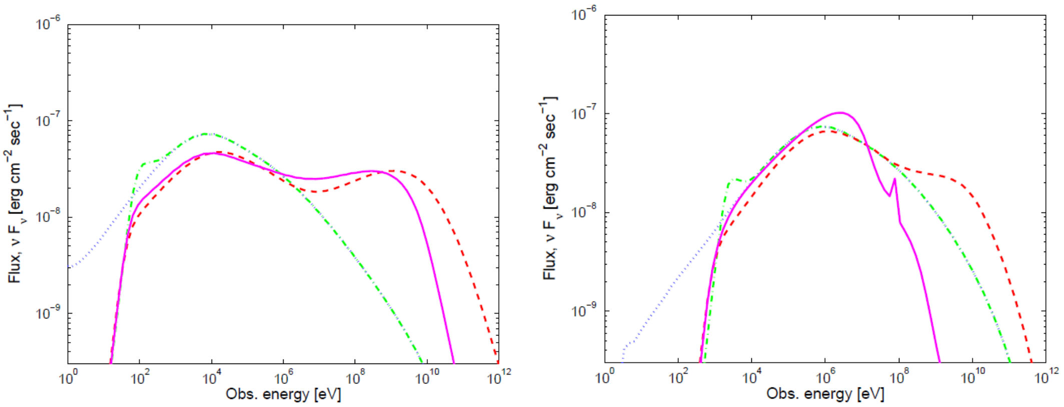

Figure 1.7: Two example spectra for optically thin (left) and sub-photospheric (right) dissipation. The different lines show the various components of the spectra: cyclo-synchrotron only (dotted), synchrotron emission and self-absorption only (dash-dotted), same plus Compton scattering (dashed) and finally all processes, including pair production (solid). Figures from Pe'er and Waxman (2005).

take place due to the fact that the outflow does not suddenly become transparent at r_{ph}: the photosphere is in reality "fuzzy" and r_{ph} simply denotes the radius at which $\tau = 1$, that is where the photons have a probability e^{-1} of escaping from the plasma (Pe'er and Ryde, 2017). To this effect, the contribution due to geometrical broadening needs also to be added, which is caused by the fact that the radiation reaching the observers comes from different parts of the jet (but still within the beaming angle $\sim 1/\Gamma$). Photons coming from different regions of the jet follow different optical paths which will cause a "limb darkening" effect, with radiation coming from an the edges appearing colder than the one coming from on-axis (Pe'er and Ryde, 2017). It should be noted however that these broadening effects alone are not sufficient to explain the observed non-thermal GRB spectra. These effects overall contribute to change a hypothetical thermal spectrum to a pseudo-blackbody, that is a thermal distribution which is subject to some broadening. Even with these effects being taken into account, it is however not possible to consistently describe the observations with a thermal distribution and some kind of dissipative process needs to be present so to provide a non-thermal component.

A very important factor for determining how much the spectrum generated by a dissipative photosphere deviates from a blackbody is where the dissipation takes place with respect to the photosphere. Regardless of the specific mechanism involved in the dissipation process, if it takes place deep inside the ejecta ($r_d \ll r_{ph}$) any initial non-thermal component will end up being thermalized due to the photons scattering many times before reaching the photosphere. If the dissipation takes place below the photosphere, but not too deep inside the outflow, the non-thermal component does not get completely thermalized and modifies the otherwise thermal spectrum emitted by the photosphere. The exact spectral shape depends thus very strongly on the optical depth τ at which the dissipation takes place, as shown in Fig. 1.8. When the dissipation takes place in the optically thin regime ($r_d \gtrsim r_{ph}$) the thermal component is relegated to a minor role (often probably undetectable by detectors such as GBM) and synchrotron and synchrotron self-Compton (SSC) dominate the emission.

Historically, the presence of a steep low energy component ($\alpha = 1$ for a pure blackbody) or the width observed in Band function fits has been taken to be indirect evidence against synchrotron emission and in favor of a thermal component (Pe'er and Ryde,

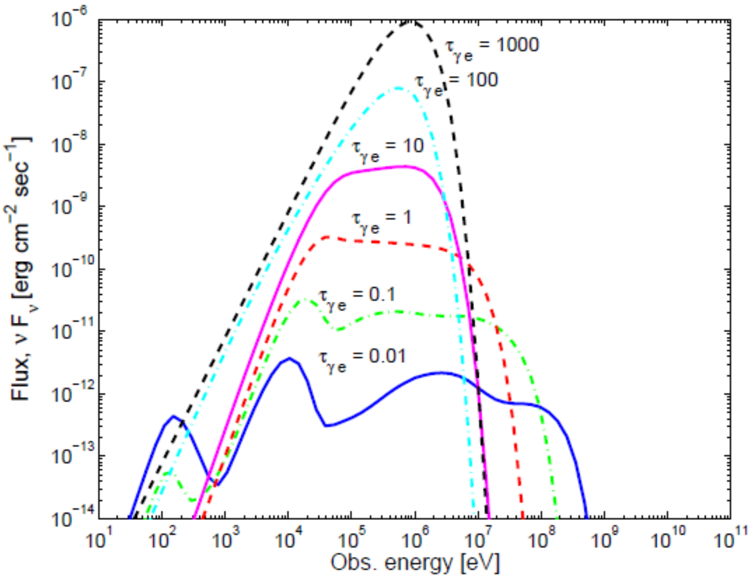

Figure 1.8: Example spectra of the dissipative photosphere model developed by Pe'er and Waxman (2005). Here $\tau_{\gamma e}$ indicates the Thomson optical depth at the dissipation radius. Note the strong dependence of the spectral shape on $\tau_{\gamma e}$: it starts as pseudo-thermal at large $\tau_{\gamma e}$, but as the dissipation radius gets closer to photosphere ($\tau_{\gamma e} = 1$) and then goes beyond it, the different physical components (thermal, synchrotron, inverse Compton etc.) of the model become more and more distinct. In particular, in the optically thin regime (blue line) the emission is dominated by synchrotron and synchrotron inverse Compton. Figure from Pe'er and Ryde (2017).

2017). This approach was however proven to produce unreliable interpretations of the data (Burgess, 2019; Burgess et al., 2020), and only direct fitting of the physical models can produce definitive results.

Due to the complexity of the simulations, generating numerical spectra requires considerable computational power, thus dissipative photosphere models have only been fitted to a very limited extent, see e.g. Ahlgren et al. (2015, 2019a,b). Most often these complex models were simply tested by evaluating their ability to reproduce the spectral shapes and peak positions given by Band function fits and not by fitting them directly to the data, which requires the generation of a very large table models. Chapter 5 addresses this problem by studying the viability of the dissipative photosphere model developed by Pe'er and Waxman (2005) by generating a large table model and fitting it directly to Fermi-GBM data.

1.3.5 Dissipation mechanisms

One of the limitations of the fireball model is that it does not specify in which way the energy of the outflow (kinetic and magnetic) is converted to radiation. This section provides a summary of the main dissipation mechanism candidates, with particular focus on internal shocks and magnetic reconnection.

The internal shock theory was developed back in the 90's (Paczynski and Xu, 1994; Rees and Meszaros, 1994) and describes a scenario in which the energy dissipation is generated by collisions between shells within the relativistic outflow. Due to the unsteadiness of the inner engine, a variable number of these shocks can take place during a single GRB and even complex lightcurves with several peaks can in principle be explained by the presence of multiple shocks (Beloborodov and Mészáros, 2017). Internal shocks thus convert kinetic energy to radiation through the collision of two or more shells with different Lorentz factors within the relativistic outflow, offering a natural explanation to the high variability

observed in many GRBs, as explained in the following.
In the simplest scenario, two shells with similar Lorentz factors $\Gamma_1 \sim \Gamma_2 \equiv \Gamma$ and $\Gamma_1 - \Gamma_2 \sim \Gamma$ are produced by the inner engine on a timescale $\delta t \sim r_0/c$. Shell 1 will catch up and collide with the slower moving shell 2 at the radius $r_{coll} \simeq c\delta t\Gamma^2$ (Piran, 2004). δt is intuitively identified as being the variability timescale, which is ultimately set by the size of the inner engine, providing thus a natural way of explaining the high variability observed in many GRBs by assuming the formation of a compact object is taking place with the burst. For a single shock between two shells of mass m_1, m_2 and Lorentz factor Γ_1, Γ_2, conservation of four-momentum yields the following final Lorentz factor (Kobayashi et al., 1997)

$$\Gamma_f = \left(\frac{m_1\Gamma_1 + m_2\Gamma_2}{m_1/\Gamma_1 + m_2/\Gamma_2}\right)^{\frac{1}{2}} \tag{1.15}$$

The efficiency of the dissipated kinetic energy is then given by

$$\epsilon_d = 1 - \frac{(m_1 + m_2)\Gamma_f}{m_1\Gamma_1 + m_2\Gamma_2} \tag{1.16}$$

This implies that to achieve high dissipation efficiency similar masses and largely different Lorentz factors are required. For example, for $\Gamma_1/\Gamma_2 = 10$ and $m_1 = m_2$, $\epsilon_d \gtrsim 40\%$, but this holds true only for a first collision, consecutive shocks will have progressively lower efficiencies (Pe'er, 2015). More likely values for the shells' conditions produce efficiencies in the range 1 – 10% (Mochkovitch et al., 1995). Moreover, dissipated energy does not directly translate to emitted radiation, since particles need to first be accelerated to high energies and then emit photons through some mechanism, e.g. synchrotron. As such, the main drawback of the internal shock scenario is its very low efficiency in converting kinetic energy to emitted radiation (Pe'er, 2015).
It must also noted that shocks don't necessarily take place only within the outflow, they can also occur between jet and the circum-burst medium (CBM) surrounding the progenitor. These shocks, known as *external shocks*, take place at much larger radii ($r \gtrsim 10^{17}$ cm) compared to the internal shock scenario. The larger collision radius implies however that this mechanism cannot explain the high variability present in many of the observed GRBs and thus this scenario is unable to explain prompt emission. On the other hand, external shocks are however able to consistently describe the afterglow emission, as explained later on in Section 1.4.1.

In contrast to the internal shock scenario, it is also possible that most of the energy of the jet is actually not kinetic, but magnetic (i.e. the jet is Poynting dominated). This is the case of magnetized outflows, which arise for example in the case of the formation of a magnetar, a neutron star with extremely strong magnetic fields, $B \gtrsim 10^{15}G$ (Pe'er, 2015). This object is thought to be formed as an intermediate step before the progenitor ultimately collapses to a black hole (Usov, 1992; Thompson, 1994; Pe'er, 2015). The amount of energy stored in the magnetic field is commonly parametrized by the magnetization parameter σ

$$\sigma = \frac{L_M}{L_K} = \frac{B^2}{4\pi\Gamma^2 n m_p c^2} \tag{1.17}$$

which is simply the ratio between the magnetic (or Poynting) and kinetic energy flow. In an highly magnetized jet $\sigma \gg 1$. Due to the fast rotation of the magnetar, changes in polarity of the magnetic field are possible on a scale $\lambda \sim 2\pi c/\Omega$, where Ω is the angular velocity of the central object (Coroniti, 1990; Pe'er, 2015). Where these changes occur, magnetic field lines can undergo a rearrangement known as magnetic reconnection. This process converts part of the energy of the magnetic field into kinetic energy and can accelerate particles. The mechanism cannot generally be described analytically and requires complex magneto-hydrodynamical simulations to be studied (Sironi and Spitkovsky, 2014; Granot, 2016), however one of its main advantages is that it can in principle reach much higher efficiencies if compared to the typical internal shock scenario, though how large this value can be is still unclear (Pe'er, 2015).

It should also to be mentioned that there are other types of mechanisms that can convert the energy within the outflow to radiation. One of those is based on the presence of free neutrons in the jet, which are produced by photo-disintegration of nuclei. Since p-n collisions have a lower cross-section than proton Thomson scattering, they end up having different velocities, which leads to some friction between the two types particle species. This results in $p - n$ collisions, which produce pions. These pions decay and produce positrons e^+, which radiate synchrotron emission and interact through Compton scattering with the thermal photons. These processes ultimately produce a non-thermal spectrum peaking around 1 MeV (Beloborodov, 2010; Pe'er, 2015).
Finally, there are also hybrid models, such as the Internal-collision-induced Magnetic Reconnection and Turbulence (ICMART), where both internal shocks and magnetic reconnection take place (Zhang and Yan, 2011). In the scenario described by the ICMART model, the shocks dissipate only a small quantity of energy (thus avoiding efficiency issues), but distort the magnetic field lines, allowing for magnetic reconnection to occur and act as the main dissipation mechanism (Zhang and Yan, 2011).

1.3.6 Polarization

Polarization measurements are potentially one of the best tools available to discriminate between different emission models for the prompt emission. From an observational standpoint, such measurements have proven to be very challenging and the results from different instruments are often inconsistent (Gill et al., 2020). To measure polarization in the gamma-ray energy range, instruments rely on the azimuthal asymmetry present in the Klein-Nishina cross-section for Compton scattering. In principle this allows to reconstruct both the polarization angle and the polarization fraction (i.e. the fraction of polarized radiation) of the incoming photons, but in practice this procedure is made difficult by the usually low photon statistics available and by the presence of significant background. The currently available polarization measurements are thus not very constraining and were not able to shed much light on the underlying physics of GRBs, see e.g. Gill et al. (2020) for a summary. There is however evidence for the presence of a change in polarization angle during the prompt mission, as inferred independently from the GAP (Yonetoku et al., 2011) and POLAR (Produit et al., 2018) instruments (Yonetoku et al., 2012; Burgess et al., 2019).

For non-dissipative photospheric emission, the maximum value for the polarization fraction is expected to be $\Pi \lesssim 15\text{–}20\%$ (Gill et al., 2020), though this estimate can change quite significantly when considering instead dissipative emission. On the other hand, a single constraining measurement with polarization fraction $50\% \lesssim \Pi \lesssim 65\%$ or measuring consistently $\Pi \gtrsim 20\%$ in a a large burst sample would strongly point in favor of synchrotron emission (Gill et al., 2020). It's also important to keep in mind that the observed polarization is affected by the geometry of the jet and the angle at which it is observed. This effects can be complex to quantify, especially given how little is known

about the jet structure.
Overall, polarimetry is one of the best candidates to successfully discriminate between different physical models for the prompt emission, but it is currently held back by the lack of instruments able to provide more constraining measurements.

1.4 Long-wavelength emission following GRBs

1.4.1 Afterglow

The longer-lasting, lower energy emission following the initial release of gamma-rays is known as *afterglow* and it can range anywhere from X-rays to radio, shifting gradually from higher to lower energies. Afterglows are observed when the burst's relativistic jets collide with the circum-burst medium (CBM) surrounding the progenitor (Rees and Meszaros, 1992; Paczynski and Rhoads, 1993), a scenario which is described by the *external shock* model. The observed emission is very well characterized by synchrotron radiation from a power-law population of electrons, in an analogous way as what described in Sec. 1.3.3. Afterglows lightcurves are typically characterized through the use of power-law segments, which express the dependence of the flux on time and frequency, $F \propto t^{-\alpha}\nu^{-\beta}$. The observed values of the indices identify precise aspects of the dynamics and geometry of the outflow (Sari et al., 1998c), as is here summarized.
The theoretical framework, already developed back in the 70's by Blandford and McKee (1976), describes a scenario in which a spherically symmetric ultra-relativistic shell of width $\sim r/\Gamma^2$ propagates through a generic external medium surrounding the progenitor (Piran and Granot, 2001). When the outflow collides with the CBM, two shocks are produced: one moving forward (forward shock) and one moving backwards into the ejecta (reverse shock). The forward shock is the one responsible for the main afterglow emission, while the reverse shock produces (at least in a fraction of cases) a so-called *optical flash*. This transient is very short-lived ($\sim$ 10 min) and in most cases it is not observed at all (Gill et al., 2020). The main focus of this section is however on the forward shock generating the main afterglow emission.
In the simplest scenario of the Blandford-McKee solution, the CBM has uniform density, but further generalizations include radial mass density profiles in the form of a power-law, $\rho = Ar^{-k}$. Of particular interest is the case $k = 2$, which describes a wind, that is the envelope lost by the progenitor prior to the GRB explosion. Under the assumption of the system being adiabatic, that is the energy losses due to radiation having negligible effect on the overall hydrodynamics, energy conservation yields the following (Piran and Granot, 2001)

$$E = \frac{\Omega}{3-k} A r^{3-k} \Gamma^2 c^2 \tag{1.18}$$

where Ω is the solid angle covered by the outflow, with $\Omega = 4\pi$ for a spherically symmetric solution (in the case of jets $\Omega \approx 2\pi\theta_{jet}^2$). This equation defines a natural length scale, known as *Sedov length*:

$$l_S = \left[\frac{(3-k)E}{\Omega A c^2}\right]^{\frac{1}{(3-k)}} \tag{1.19}$$

The Sedov length defines the radius at which the ejecta sweeps up a mass of the external medium equivalent to the outflow's initial energy. In the simplest case of a spherically symmetric outflow in a uniform medium ($k = 0$ and $\rho \equiv \rho_0 = 4\pi m_p n_0$, assuming the mass to be dominated by protons) the Sedov length is simply $l_S = (3E/4\pi m_p c^2 n_0)^{1/3}$. This implies that l_S also defines where the transition from the initial ultra-relativistic regime (i.e. Blandford-McKee solution) with $\Gamma \gg 1$ to a Newtonian regime $\Gamma \approx 1$ takes place. In the lightcurve, this corresponds to an *achromatic break*, that is a change in the slope of the flux lightcurve present at all frequencies (Piran and Granot, 2001).

Considering instead the more realistic case of jetted emission, the afterglow becomes more complicated to describe. For simplicity, it is here assumed that the jets are uniform, with small aperture angles θ_{jet}. During the first phase of the emission, as long as $\Gamma \gtrsim \theta_{jet}^{-1}$, relativistic beaming prevents the observer from seeing the entirety of the jet, which implies that it is initially not possible to discriminate between jetted and spherically symmetric emission. When the ejecta slows down to $\Gamma \approx \theta_{jet}{}^{-1}$, the relativistic beaming effect subsides and the jet becomes fully visible. This implies that a further decrease in speed of the outflow will not increase anymore the emitting surface visible to the observer. This corresponds to a change of the steepness in the flux lightcurve known as *jet break*. As previously mentioned in Sec. 1.3.2, the presence of these transition points in afterglow observations constitutes strong evidence for the presence of relativistic jets during the prompt emission. Additionally, while in the ultra-relativistic regime the motion of the jet is conical (i.e. the angular spread is negligible), at later times sideways expansion of the jet becomes relevant. This can produce an additional break in the lightcurve, though its position depends on the speed with which this sideways expansion takes place (Piran and Granot, 2001).

It should also be noted that various assumptions here considered are likely violated for at least part of the emission. For example, the adiabatic approximation can be violated at the very early stages of the afterglow emission, when the system may be in a radiative regime, where energy losses due to radiation can be large enough to affect the hydrodynamics of the outflow (Piran, 2004). Moreover the shape and internal structure of the jets play also an important role in characterizing the afterglow emission and a uniform jet approximation may deviate significantly from reality.

Finally, additionally to pure synchrotron emission, there are at least two other effects to take into account: synchrotron self-absorption (SSA) and synchrotron self-Compton (SSC). SSA is an absorption mechanism where the population of electrons responsible for the emission of the synchrotron photons is also absorbing part of them. In practice, this translates in a steep slope $\propto \nu^{\frac{5}{2}}$ at lower energies. Note that this mechanism is unimportant for the prompt emission and the first part of the afterglow, as it only matters when the emission shifts to longer wavelengths, such as radio (Piran, 2004).

SSC is instead thought to be responsible for the observation of very high energy photons (up to hundreds of GeV, see e.g. MAGIC Collaboration et al. (2020)) soon after the prompt emission is detected (Zhang et al., 2020). The existence of such high energy component is also suggesting that the conditions to produce high energy neutrinos are likely to be present, see Sec. 1.5. In this case, the neutrino production could be delayed with respect to the prompt emission and take place instead during the afterglow phase (Waxman and Bahcall, 2000). In such scenario, neutrinos with energies up to $\sim 10^{19}$ eV would be produced through Δ resonance (see Sec. 1.5) by the interaction between high energy protons (with energies $\lesssim 10^{20}$ eV) and optical-UV photons produced by the afterglow's reverse shock. The corresponding neutrino flux may however be too weak to be detected by the current generation of detectors (Nir et al., 2016; Thomas et al., 2017).

1.4.2 Kilonovae

In the case of neutron star mergers, in addition to the jetted emission responsible for gamma-rays and afterglow, another component is expected to be present, the so-called *kilonova* (Li and Paczyński, 1998; Metzger et al., 2010). The kilonova emission occurs when, during the merger, a small fraction of the mass of the binary system (of the order of $10^{-4} - 10^{-2}\ M_{\odot}$) is expelled due to tidal and/or hydrodynamical forces (Metzger et al., 2010; Ascenzi et al., 2019). The resulting outflow is mildly relativistic (with speeds of $\sim 0.1c$) and is expected to be highly rich in neutrons, implying thus a high rate of element synthesis through r-process. The following radioactive decays power then a thermal optical/infrared/ultraviolet transient, with typical luminosities ranging from 10^{40} to 10^{44} erg/s (Metzger et al., 2010). The first of these transients was detected only in relatively recent times, with the observation of GRB 130603B (Tanvir et al., 2013). Of particular importance is also the fact that kilonova emission is expected to be roughly isotropic, implying that it is in principle possible to observe these transients even from off-axis angles, i.e. when the relativistic jets are not pointing onto the observer. This was most likely the case for the particularly significant kilonova detection of GW/GRB 170817 (Troja et al., 2018).

The kilonova ejecta can present multiple components depending on the lanthanide content (i.e. high Z elements formed through r-process synthesis). An outflow with very little or no lanthanide content would move faster due to its lower mass and appear “bluer”, thus the name of *blue kilonova*. Conversely, a lanthanide rich ejecta would move slower and appear “redder”, i.e. a *red kilonova* (Ascenzi et al., 2019). The distinction between these two components arises due to the two different forces acting as ejection mechanisms: the matter which is ejected by tidal forces is expected to be richer in neutrons (i.e. larger lanthanide content through r-process) while the matter expelled by hydrodynamical forces would instead be poor in neutrons (Ascenzi et al., 2019).

The theoretical predictions regarding kilonovae were largely confirmed with the exceptional observation of GW/GRB 170817, which provided an unprecedented amount of data thanks to the many instruments being involved in the observations (Metzger et al., 2010). Kilonovae remain however challenging to observe and identify, both because they require very precise localization (from e.g. X-ray detectors observing the afterglow) and also because the kilonova emission doesn’t peak right away after the burst, but typically 1-2 days after the GRB has occurred (Metzger et al., 2010), so instruments may often not be observing during the optimal time window.

1.5 GRBs as multi-messenger sources

GRBs are deemed to be good candidates for multi-messenger observations and, at least for short GRBs, detection of a simultaneous EM-GW signal has been proven to be possible (Abbott et al., 2017; Goldstein et al., 2017). GRBs are not only gravitational waves sources, but they are also thought to dissipate a significant fraction of their energy through the emission of neutrinos (potentially up to very high energies), which could in principle be observed by today’s neutrino detectors, such as e.g. IceCube (Aartsen et al., 2017). In GRBs, an efficient channel to produce neutrinos is through pion decay $\pi^- \rightarrow \mu^- \ \overline{\nu}_\mu$ or its π^+ equivalent, in which case pions are produced through $p\gamma$ or pp interactions. The $p\gamma$ process requires the photon to have an energy of about $\sim$ 200 MeV in the proton frame so to be able to create Δ particles (m_Δ = 1.2 GeV) through a resonance (Piran, 2004). These particles can then decay into pions, which in turn decay to neutrinos with typical energies of $\sim$ 50 MeV in the proton frame. Given that protons are moving at relativistic speeds with a Lorentz factor γ_p in the observer frame, neutrinos are observed having energies a

factor γ_p higher. With this mechanism neutrinos with energies up to 10^{19} eV can be produced, assuming the photon flux is large enough and that there are no significant energy losses for the pions before they decay (Piran, 2004).
Observation of astrophysical neutrinos is however extremely challenging: even with very large detectors such as IceCube, the event statistics is very poor and the reconstruction difficult. As of now, with the exception of the serendipitous observation of supernova SN 1987A (Burrows and Lattimer, 1987), the only identified neutrino source is the blazar (i.e. an active galactic nucleus with its jet pointing in the observer direction) TXS 0506+056 (IceCube Collaboration et al., 2018). Moreover, neutrinos produced by GRBs could also lack an electro-magnetic counterpart, which would make the identification of the neutrinos as part of the GRB emission most likely impossible. In the core-collapse scenario, this would be the case for bursts with *chocked jets*, i.e. when the jet cannot manage to pierce through the stellar envelope and no gamma-ray emission is detectable. These GRBs could constitute a significant fraction of the unidentified astrophysical neutrinos in the detectors. The findings in IceCube Collaboration et al. (2018) seem however to indicate that a significant fraction of the observed IceCube neutrinos may be produced by active galactic nuclei (AGNs), though how large this fraction is still under debate. Nonetheless, GRBs are still good candidates to explain a large part of the remaining flux, although there has been no successful identification so far. From a detection standpoint, compared to AGNs, they present both advantages and disadvantages. Since GRBs are transients, their detection and localization is very challenging: observation is only possible in a narrow time window and the reconstructed gamma-ray position is often not very constraining. Precise localizations from e.g. X-rays or optical instruments are available only in a fraction of cases. If one assumes that the neutrinos are emitted mainly during the prompt emission (Mészáros, 2015), this allows however to set a narrow time window for the neutrino-electromagnetic coincidence searches, which can yield a higher significance for a potential simultaneous signal. In the AGN and other steady sources cases instead, the position is well known, but the time of potential neutrino emission is not.

As of now, there are two major obstacles to GRB neutrinos detection, namely the location and spectrum of these sources. Most of the currently detected bursts are from Fermi-GBM observations, which are often not very constraining in terms of localization, especially due to the fact that large positional systematics are present, as detailed in Chapter 4. A large position uncertainty from the gamma-ray observation on top of the often not very constraining neutrino localization implies that, even if a simultaneous signal was to be detected, it would be impossible to confirm that it is produced by the same source due to the low resulting significance. Furthermore, the many unknowns about the electromagnetic emission in GRBs affect the predicted neutrino flux, which as of today still remains very uncertain.

Similar arguments can also be made for gravitational wave signals. As previously mentioned, GRBs have been theorized to be strong sources of gravitational waves. This was observationally confirmed in 2017, with the simultaneous detection of a gamma-ray signal together with LIGO's observation of gravitational waves from a binary neutron start merger (Abbott et al., 2017; Goldstein et al., 2017). While gravitational waves detectors are continuously improving, the detection of binary neutron star mergers is still very challenging, since it requires the event to take place close enough so that the GW instruments can detect it, but also that the gamma-ray signal is bright enough to be seen by detectors such as Fermi-GBM. Much like neutrinos, correct identification of gravitational waves' counterparts also relies on having gamma-ray locations as constraining as possible.

1.6 Tackling the open issues in GRB science

Gamma-ray bursts, with their extreme luminosities which allow them to be detected even at cosmological distances, constitute one of the best candidates to explore the high redshift Universe. Yet these sources, even after decades of studies, remain poorly understood. There are a multitude of issues still afflicting the study of these objects, arising from both the difficulty in observing GRBs and the complexity in modeling them from a theoretical standpoint. This thesis thus tries to tackle both of these problems.

First of all is the issue of the locations provided by GBM. While the instrument can reliably observe a large number of bursts every year, the localizations the instrument provides are most often not very constraining, even more so since the detector is affected by significant systematics. This implies that follow-up multi-wavelength observations (but also multi-messenger searches, see Sec. 1.5) become much more difficult to carry out and are much more likely to turn out unsuccessful. This constitutes a significant problem, especially given how much importance afterglow observations and redshift measurements hold when studying GRBs and their host environments.

On the other hand, the understanding of the physical processes involved in the prompt emission is also struggling to advance. This is the case not due to the lack of a theoretical framework, but due to its insufficient testing performed so far. As previously mentioned in Sec. 1.3.4, due to being very computationally expensive, physical models have been directly fitted to GRBs only to a very limited extent. Most often they have just been compared to the spectral shapes of empirical functions fits (e.g. Band function fits), methodology which has been proven to be unreliable for performing physical inference (Burgess et al., 2020) and thus doesn't allow for proper estimation of the physical parameters of the source.

As such, the purpose of this thesis is twofold: Chapter 4 addresses the issue of poor localizations, showing that a better statistical methodology can vastly improve Fermi-GBM positions and almost completely remove its systematics, while Chapter 5 shows how fitting physical models to GRBs can help constrain the physical conditions of the source, which can also be used to improve the accuracy of the predicted neutrino flux from theoretical models.

Chapter 2

The Fermi space telescope

2.1 Introduction

The Fermi space telescope (formerly known as GLAST) is a space observatory designed to observe gamma-ray sources. Launched on June 11, 2008, it is still currently operational. It is composed of two separate instruments: a pair production telescope, the *Large Area Telescope* (LAT), and a *Gamma-ray Burst Monitor* (GBM). The spacecraft is orbiting around the Earth at an altitude of 565 km every $\sim$1.5 h and is able to scan the whole sky through a rocking motion, i.e. the spacecraft changes its pointing from one hemisphere to the other every orbit, allowing for a roughly uniform sky exposure (Atwood et al., 2009). Overall, Fermi can observe photons with energies comprised within 8 keV and 300 GeV.

2.2 The Large Area Telescope

The LAT is a pair production telescope designed to observe photons ranging from $\sim$20 MeV up to more than 300 GeV, providing a field-of-view of 2.4 sr (Atwood et al., 2009). Correct reconstruction of photons below 100 MeV is however very challenging due to severe energy dispersion and as such the use of these events for data analysis requires particular care through a technique known as LAT Low Energy (LLE), see Pelassa et al. (2010) for more details. LLE data is nonetheless very useful for GRB spectral analysis and will be used, whenever available, to better constrain the high energy components in the fits performed in Chapter 5. While in terms of number of detected bursts LAT is a far less prolific detector than GBM, the instrument has nonetheless been able to provide a number of important observations of high energy emission from GRBs (Ackermann et al., 2013; Ajello et al., 2019). Furthermore, the LAT is also designed to be automatically repointed to any burst of particular interest detected by GBM through an automated algorithm (Meegan et al., 2009). If a burst is thus detected by the LAT, the reconstructed location is far more precise than GBM's.
The LAT is composed of two main parts, a *tracker* and a *calorimeter*. The tracker consists in a series of 16 layers of single-sided silicon strip detectors (SSDs), which purpose is to track the trajectories of the pairs. To provide the necessary cross-section to produce the pairs, tungsten plates are inserted in between the tracker layers. Each of the SSDs can only measure the position along one direction, so consecutive layers are rotated by 90° with respect to each other in order to provide a two-dimensional position measurement (Atwood et al., 2009).

The second part of the LAT is a calorimeter composed by 96 cesium iodide (CsI)

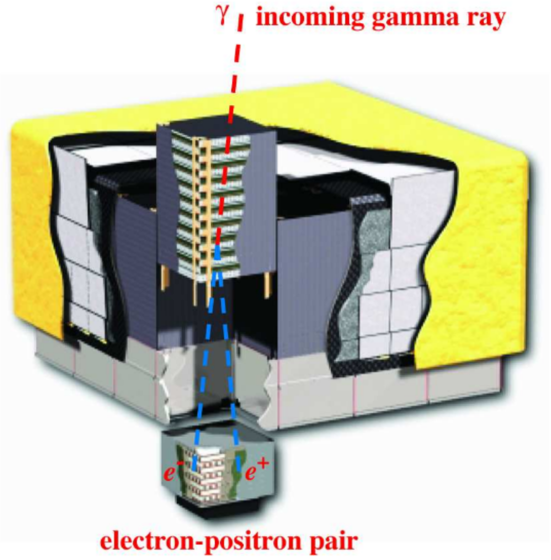

Figure 2.1: A schematic of the LAT and its measurement process. Incoming photons interact with the tungsten plates in the tracker, creating an $e^{-}e^{+}$ pair. The trajectories of these particles are then measured by the tracker, while their energies are measured by the calorimeter. Figure from Atwood et al. (2009).

scintillation bars coupled to photo-multiplier tubes (PMTs) for read-out. The crystals are arranged in a hodoscopic fashion, i.e. consecutive layers are rotated by 90° with respect to each other. This allows the calorimeter to also provide some positional information about the energy deposition along the bars through the different amount of scintillation light being collected at the opposite ends of the crystal (Atwood et al., 2009).
The instrument is also surrounded by a plastic anti-coincidence detector (ACD) to avoid triggers due to charged particles from cosmic rays.

2.3 The Gamma-ray Burst Monitor

The Gamma-ray Burst Monitor (GBM) is an instrument primarily designed to observe gamma-ray bursts, though it is also able to detect other gamma-ray transients such as solar flares, terrestrial gamma-ray flashes etc. GBM observes the energy band comprised between 8 keV and 40 MeV, an energy window which captures most of the GRBs' emission (Meegan et al., 2009). The instrument is the main focus of this chapter, as it provides the vast majority of the data being used in Chapter 4 for localizations and in Chapter 5 for spectral fitting. The instrument is operating at all times, except during the transit through the South Atlantic Anomaly (SAA). This region, which roughly encompasses South America and the South Atlantic Ocean, corresponds to a zone of weaker geomagnetic field, which implies that there's a much higher flux of charged particles compared to the other regions of equal altitude. This area greatly increases the background in scientific instruments and can potentially even cause damage, if they are not turned off during the transit. As such, GBM does not collect data while flying over this location, which reduces the total observation time by $\sim$15% (Fermi website).
The instrument can potentially detect GRBs from any direction in the sky, but in practice the detector array is optimized for detection from the upper hemisphere of the spacecraft, since the lower one is for the most part occulted by the Earth. GBM detects roughly 240 bursts per year, of which about 17% are short GRBs (Connaughton et al., 2015), and is thus the most prolific GRB detector in history, with more than 2700 detected GRBs as of now (Fermi-GBM data).

GBM consists of an array of 14 detectors (see Fig. 2.2), each pointing in a different direction so to provide an overall all-sky field-of-view to the instrument. Each of these detectors is a unit composed of a scintillation crystal coupled to a photo-multiplier tube (PMT), one of which is shown in Fig. 2.2. There are 12 thallium activated sodium iodide (NaI(Tl), denoted by a "n" from now on) detectors for low energy photons (8 – 1000 keV) and two bismuth germanate (BGO, denoted by a "b") detectors for higher energies (0.2 – 40 MeV). The NaI crystals are cylinders with dimensions of 12.7×1.27 cm, while the BGO crystals are thicker, with a size of 12.7×12.7 cm (Meegan et al., 2009).

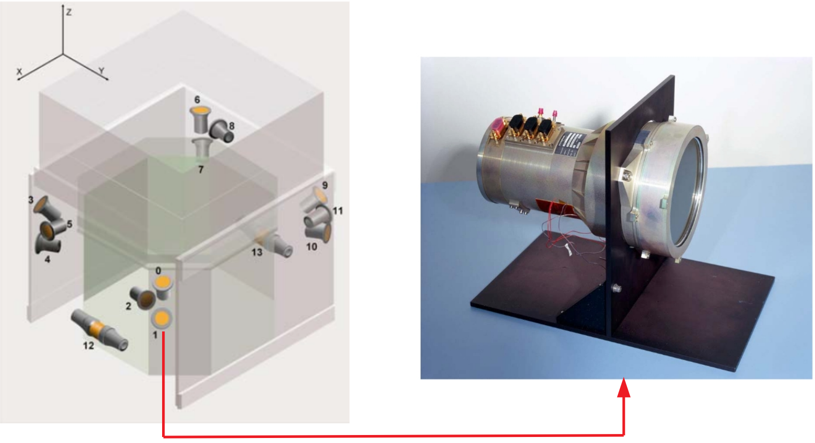

Figure 2.2: On the left, a schematic of the detector array composing GBM (NaIs from 1 to 12, 13 and 14 for BGOs). On the right, a photo of one of the NaI detectors. Original figures from Meegan et al. (2009).

For each detector and energy channel a count rate is measured. These counts depend on both the spectrum and the position of the source through the change in the corresponding effective area, as shown in Fig. 2.3. It is important to understand that the measured counts are simultaneously affected by both spectrum and position and as such it is impossible to separate the source reconstruction process in a location fit and a spectral fit, unless e.g. there is external data from another instrument providing a position for the source.

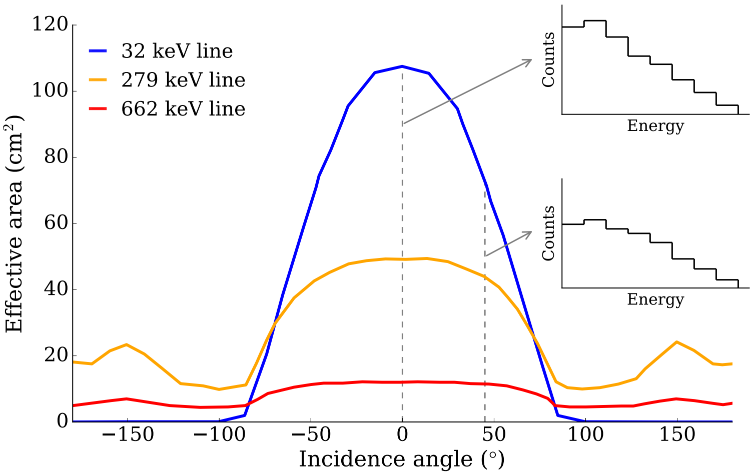

Figure 2.3: Photopeak effective area curves for a single NaI detector for varying incidence angle (i.e. angle between the incoming photon and detector boresight). Figure from Berlato et al. (2019).

The reconstruction process is further complicated by the presence of significant energy dispersion: the counts in each energy channel do not necessarily belong to source photons of the corresponding energy bin, but may be generated by higher energy photons instead. This can happen due to various possible reasons, such as e.g. scattering on passive materials or other parts of spacecraft, partial absorption of the photons in the crystals etc. This implies that for photons of a certain energy emitted by the source, counts can be generated not only in the corresponding energy bin, but also in all the lower energy channels.

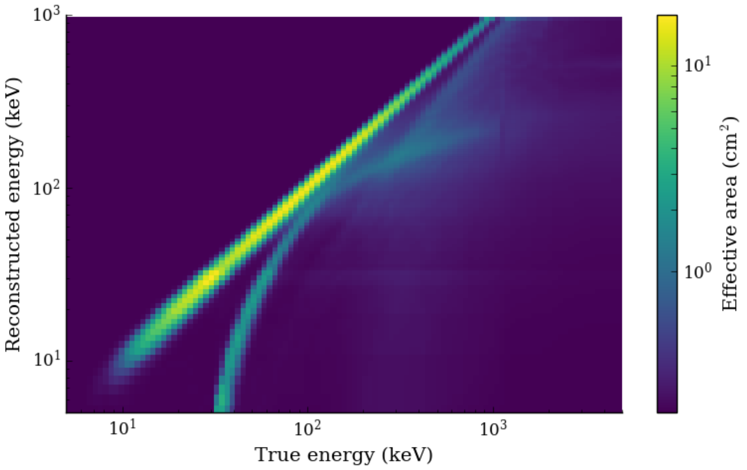

Figure 2.4: A graphical representation of the response matrix for one of the NaI detectors. For an ideal instrument without energy dispersion, the effective area would be non-zero only along the diagonal (within the limits of the energy resolution of the instrument).

The detector response is thus not a one-to-one correspondence between true and reconstructed energy, but there is always some "smearing" of the reconstructed energy to lower values, see Fig. 2.4. This has the important consequence that the response matrix is not invertible, since there is no unique correspondence between true and reconstructed photon energies.

In practice this implies that, even if the position of the source is known, it is impossible to directly invert the response and reconstruct the flux in each energy channel. It is however still possible to reconstruct both the source's spectrum and position through an approach known as *forward-folding*. The main idea of this method relies on testing different combination of parameters (in general both positional and spectral) by convolving that particular source configuration through the detector response and comparing the counts obtained by that test configuration to the actual ones. The process is then repeated until the most likely parameter combination is found. The details on how this is performed in practice depend on the specific fitting methodology, as detailed in Sec. 4.1.
To obtain reliable results from the fitting, an accurate instrument response is of utmost importance. In GBM, this response is composed of three different components (Kippen et al., 2007; Meegan et al., 2009; Bissaldi et al., 2009):

1. **Direct response**: this is the count rate measured by the instrument if the photons reach directly the detectors. This response has been generated through simulations and also measured directly through laboratory calibrations.

2. **Spacecraft scattering model**: since photons can be absorbed and scattered by the different spacecraft parts, an additional response component needs to be taken into account. This was computed through the use of GEANT4 simulations.

3. **Atmospheric scattering**: the source's photons will also be scattered by the Earth's atmosphere, and this will cause an additional component which needs to be taken into account. Again, this response is obtained through simulations.

These three different components of the response all affect the final measured counts and, through the fitting process, the accuracy of the reconstructed source parameters. As discussed more in detail in Sec. 4.3, an inaccurate response can introduce systematics in the source reconstruction process.

Finally, GBM regularly produces various different types of data products (see Tab. 2.1), but in the scope of this thesis only trigdat (trigger data) and TTE (Time Tagged Event) data will considered. Both of these data types are automatically generated when a trigger of any kind occurs.

Table 2.1: The main GBM data products (Meegan et al., 2009). Trigdat data is the only data available right after a trigger. For further information, refer to GBM Data Products Description.

Data type	Description	Resolution
Trigdat	Low resolution trigger data	Energy: 8 channels Time: 0.064 - 8.192 s
TTE	High resolution trigger data	Energy: 128 channels Time: 2 μs
CSPEC	Continuous high energy resolution	Energy: 128 channels Time: 4.096 s
CTIME	Continuous high time resolution	Energy: 8 channels Time: 0.256 s

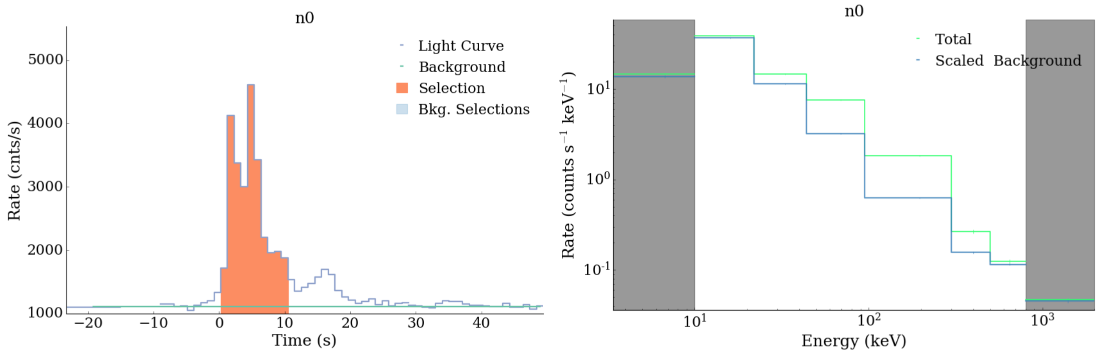

Figure 2.5: Example of GBM trigdat data for detector n0 for GRB 150201.574. On the left, the lightcurve with the selected source interval (orange filling) and the fitted background (light blue line). Counts are rebinned for easier visualization. On the right, the corresponding count spectrum. The first and the last energy channels are grayed-out since they are not used for fitting.

Trigdat data is almost immediately (~10 min) generated and down-linked after an event is triggered in GBM. This very short delay comes however at the price of a much lower resolution: the detector counts are binned both in energy (8 channels) and in time, with a variable resolution ranging from 64 ms close to the trigger time to 8.192 s farther away, see Fig. 2.5. This is done to minimize the amount of data which needs to be processed and transferred, so that the data files are available as quickly as possible. This is the data type commonly used for GRB localization and it is employed for counterpart (multi-wavelength and/or multi-messenger) searches. A further complication is that, from the total 8 energy channels, the first (due to significant absorption of the photons by the passive materials) and the last (due to pile-up of the counts from photons with energies greater than the maximum allowed by the detector) need to be excluded when fitting.

On the other hand, TTE data is available only a few hours after the trigger, but carries much more detailed information: for each detector, the count data is binned in 128 energy channels and unbinned in time. This data type is down-linked several hours after the trigger, usually too late to be used for counterpart searches (e.g. afterglow), but it is very important for spectral fitting due to the finer energy resolution. Chapter 4 relies on trigdat data for the localization performance study and systematics searches, while Chapter 5 employs instead TTE data for the spectral fitting.

Chapter 3

Statistics considerata

3.1 Introduction

The scope of this chapter is to briefly discuss the different statistical approaches to the source reconstruction process in gamma-ray detectors, with particular focus on what is used for GBM. As previously explained in Chapter 2, this procedure cannot in general be separated in a positional and spectral fit: both of them need to be performed at the same time. As will be shown in Chapter 4, failure to do so introduces systematics in the source reconstruction process. This issue can however be avoided by making use of the proper statistical treatment.

In high-energy astrophysics the signal, that is the counts measured by the detector, follows Poisson statistics, which naturally describes data from counting experiments. The normal approximation is generally not valid, as the counts can be a very small. As explained in the next section, this has important consequences on how the fitting is performed and on which form the likelihood function takes. In the measured counts, together with the source's signal, there exists always a background component, which also generally follows Poisson statistics (though in many cases the associated counts are large enough that it can be approximated to a normal or truncated normal distribution). In many cases the background component is of the same order or even dominant when compared to the source's signal and as such correct statistical modeling of this contribution is of fundamental importance for achieving correct results in the reconstruction process.

The following sections thus provide a brief summary of the differences between the main fitting approaches. Sec. 3.2 shows how different statistics affect the fitting method, while Sec. 3.3 details the approach used for fitting and model checking in this thesis.

3.2 χ^2 and Poisson statistics

Historically, the most common fitting method in astronomy has been the χ^2 minimization (see e.g. Andrae et al. (2010) for a review) due to its ease of computation. This procedure involves the minimization of the following quantity

$$\chi^2 = \sum_{i=1}^{n} \left(\frac{y_i - f(x_i, \vec{\alpha})}{\sigma_i} \right)^2 \tag{3.1}$$

where y_i are the measured values at position x_i, σ_i are the uncorrelated gaussian uncertainties of the data, $\vec{\alpha}$ is the vector of parameters describing the model and $f(x_i)$ is the expected value at x_i. If the measured values are normally distributed, this minimization process is equivalent to computing the maximum likelihood for the model. In case they are not, there is no correspondence between the two methods. While gaussian distributed quantities are common in physics, they are certainly not the rule and using χ^2 minimization when its assumptions are not valid can produce incorrect results.

More generally in high energy astrophysics the measured quantities, such as the counts measured per energy/time bin, follow Poisson statistics, that is

$$P(n) = \frac{\lambda^n e^{-\lambda}}{n!} \tag{3.2}$$

which represents the probability of measuring n counts given the expected value λ in a particular bin. Note that only in the limit of large λ the Poisson distribution becomes a gaussian, using a normal distribution to describe the counts would generally lead to incorrect results. The different statistics implies that the χ^2 minimization method is no longer applicable and that the likelihood takes a different form.

It's important to keep in mind that the quantity following Poisson statistics is always the total signal (source plus background). The background component can be estimated through an off-time (before and/or after the source is active) or off-position (pointing away from the source) measurement. The obtained value cannot however be considered as a constant to be subtracted from the total signal, since this neglects the background uncertainties and can produce negative source counts, which are unphysical and cannot be accounted for by a Poisson distribution. Failure to properly incorporate the background uncertainties in the model can produce inaccurate results in the final parameter estimation obtained through the fit and is one of the potential sources of systematics.

3.3 Bayesian approach

In contrast to the frequentist definition, which views probability as the frequency of a particular outcome in the limit of an infinite amount of trials, the bayesian approach sees probability as a value quantifying the amount of information available regarding a certain event. Notably, this also implies that any prior belief or knowledge regarding the outcome affects the estimated probability. As the name implies, this approach is based on the Bayes' theorem, that is

$$P(A|B) = \frac{P(B|A)P(A)}{P(B)} \tag{3.3}$$

where and $P(x)$ is the probability of x and $P(x|y)$ is the conditional probability of x given y. This general probabilistic statement can in practice be used to draw information on the parameters of a model to be fitted to the data. Suppose the data D is fitted with model $\mathcal{M}$, described by the vector of parameters $\vec{\alpha}$. Then the Bayes theorem takes the following form

$$P(\vec{\alpha}|D) = \frac{P(D|\vec{\alpha})P(\vec{\alpha})}{P(D)} \tag{3.4}$$

where the different terms have the following meaning:

- $P(\vec{\alpha}|D)$ is the *posterior distribution*, which describes how likely a certain parameter configuration is, given the information provided by both the data $P(D|\vec{\alpha})$ and any prior knowledge or belief given by $P(\vec{\alpha})$.
- $P(D|\vec{\alpha})$ is the *likelihood*, that is the probability of measuring the data given a specific parameter vector $\vec{\alpha}$ of model $\mathcal{M}$.

- $P(\vec{\alpha})$ is the *prior distribution*, which quantifies how likely a certain parameter configuration is a priori. This knowledge usually comes from previous experiments, observations or theoretical constraints.
- $P(D)$ is the *evidence*, that is the probability of measuring the data under the assumption of model $\mathcal{M}$ being the true model (integrating over all possible parameter configurations). This term plays a secondary role in analyses due to the fact that it merely acts as an overall normalization factor and as such can be neglected in most cases.

Regardless of the specific type of problem, the objective of a bayesian analysis is ultimately to reconstruct the posterior distribution describing the model's parameters, which is formally computed by integrating the second term of Eq. 3.4 over $\vec{\alpha}$ (i.e. all possible parameter configurations), that is

$$P(\vec{\alpha}|D) = \int \frac{P(D|\vec{\alpha})P(\vec{\alpha})}{P(D)} d\vec{\alpha} \tag{3.5}$$

Solving this integral analytically is generally not possible and in practice it is almost always necessary to make use of numerical methods. There are multiple ways to approach the problem, but most commonly what is done is to employ Monte Carlo integration, which relies on approximating the integral through sampling techniques. This operation is usually performed through the use of Markov chain Monte Carlo (MCMC) methods (see e.g. Betancourt (2017) for a review), though there are also alternatives such as MULTINEST (Feroz et al., 2009), which is used in Chapter 4 and 5 for fitting respectively locations and spectra. Regardless of the specific approach, sampling the posterior distribution is generally a much more computationally demanding task when compared to standard frequentist methods such as the maximum likelihood, which, from a numerical standpoint, constitutes just a minimization problem. This is the main reason why the bayesian approach to data analysis wasn't very common until even just a couple of decades ago, however, with the rapid improvement of the available computational power, it is now possible to perform such analyses in reasonable times, depending of course on the complexity of the problem.

Once the posterior is available, it is possible to compute the probability distribution of a single parameter in the model simply by marginalizing, that is integrating, over the other parameters, as in the following

$$P(\alpha_i|D) = \int \frac{P(D|\vec{\alpha})P(\vec{\alpha})}{P(D)} d\vec{\alpha}_{k\neq i} \tag{3.6}$$

where the integration is performed over all the α_k with $k \neq i$. A common way to display the marginal distributions is through the use of the so-called corner plots, such as the one displayed in Fig. 3.1. The figure displays the results of one of the spectral fits from Chapter 5. The precise meaning of the parameters is not relevant in the context of this chapter, what is interesting to observe is the shape of the distributions themselves. Depending on the “strength” of the data and the ability of the model to describe it, it can be more or less difficult to constrain some parameters. For example, the parameter ϵ_B in the figure, is in this case poorly constrained, retaining for the most part the shape of its prior, a log uniform distribution. Note that this does not constitute a problem in itself, it just implies that either the data is too weak to constrain the value of the parameter, or that the parameter itself has relatively poor predictive power in the context of the model, i.e. the other variables have a far greater impact on the measurable quantities, i.e. the detector counts.

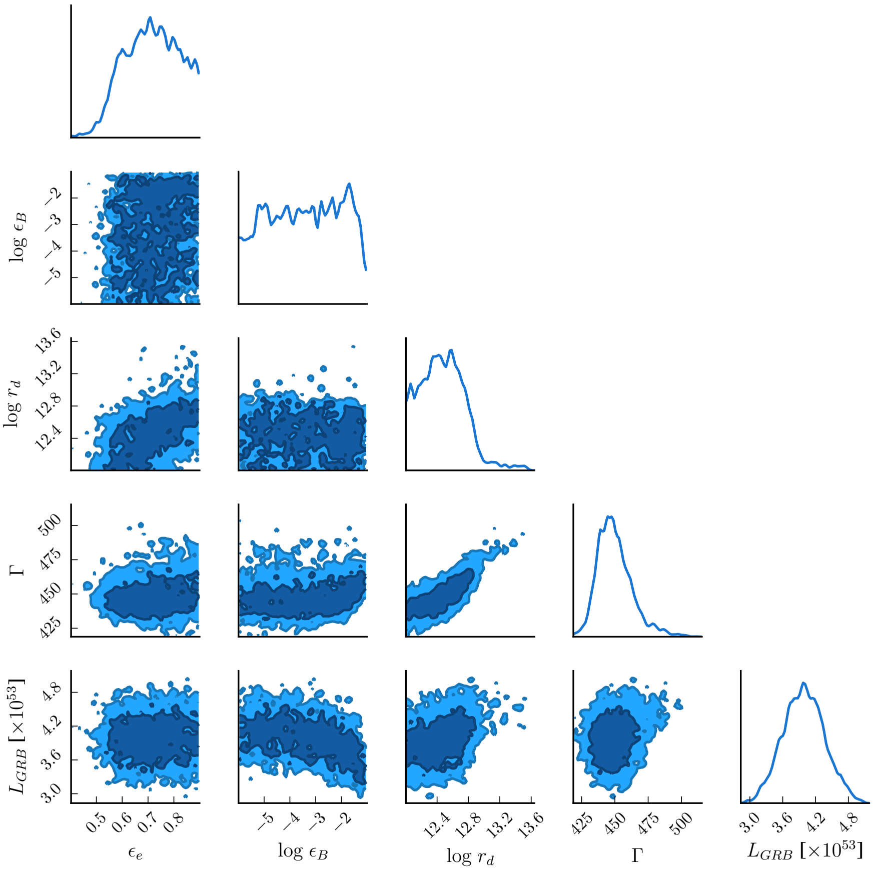

Figure 3.1: An example of a corner plot from one of the spectral fits in Chapter 5. On the top of each column, the marginal distribution of each parameter is visible. Below, the 2-dimensional distributions for the various parameter combinations are displayed, with the two shades of blue denoting the 68% (darker) and 95% (lighter) probability regions.

Regarding what is considered as the final "best" fit parameters, they are chosen as the configuration maximizing the posterior, i.e. the mode of the distribution. Note that in general these values are different from the ones maximizing the individual marginal distributions of Eq. 3.6. Generally speaking, the posterior distribution can be multimodal and as such it is important to monitor plots like Fig. 3.1 to see if the distributions exhibit any peculiar features that could skew the final parameter estimates and cannot always be noticed by simply looking at point estimates (such as mode, mean or median) and their uncertainties.

3.3.1 Model checking

A very common problem in data analysis is "model checking", that is assessing whether the fitted model is able to describe the data accurately or not. In general it is not possible to verify whether the chosen model is the "real" one, but only whether it is a sufficiently good approximation of the physical phenomenon being described. If one is not able to find significant inaccuracies in the model given the constraints applied by the measurements' uncertainties, then it can be deemed to fit the data well. In some instances, the model can directly be tested against a "true" value, which may come from e.g. an independent and much more constraining measurement. This is for example the case for the GBM GRB localizations in Chapter 4, which are compared to the much more precise *Swift* positions. In general however it is not so straightforward to verify whether a given model is able to describe the data accurately or not, especially when many parameters are simultaneously affecting the end result, as for example in the case of the spectra fitted in Chapter 5. In these instances the model can be validated through the use of graphical checks (Wilk and Gnanadesikan, 1968; Gelman, 2003), which allow for a quick and reliable assessment of the fit's performance. In practice, in Chapter 4 this is done through a comparison of the expected and achieved distributions for the parameters describing the localization's performance of GBM, while in Chapter 5 posterior predictive checks (PPCs, see e.g. Gabry et al. (2019)) are instead employed. PPCs are tests which purpose is to assess whether the fitted model can replicate the observed data. Assuming a hypothetical fitted model described by the posterior $P(\vec{\alpha}|D)$, it is possible to draw a parameter vector from this distribution. This vector defines a configuration for the model which can be used to simulate a new dataset D_{rep}. This operation can be repeated many times, sampling each time a new parameter vector from the posterior distribution and generating a new dataset from that model configuration. Mathematically, this can be expressed as

$$P(D_{rep}|D) = \int P(D_{rep}|\vec{\alpha})P(\vec{\alpha}|D)d\vec{\alpha} \tag{3.7}$$

which expresses the likelihood of observing the replicated data given the original measurements. In practice, by replicating many datasets from different parameter configurations one is able to obtain credible regions (i.e. probability intervals) which should capture the vast majority of the real data, if the fitted model is a good description of the physical phenomenon being studied. This can be better visualized with a practical example, as shown in Fig. 3.2, where GBM's observed counts are compared to the credible regions of the counts expected by the fitted model.

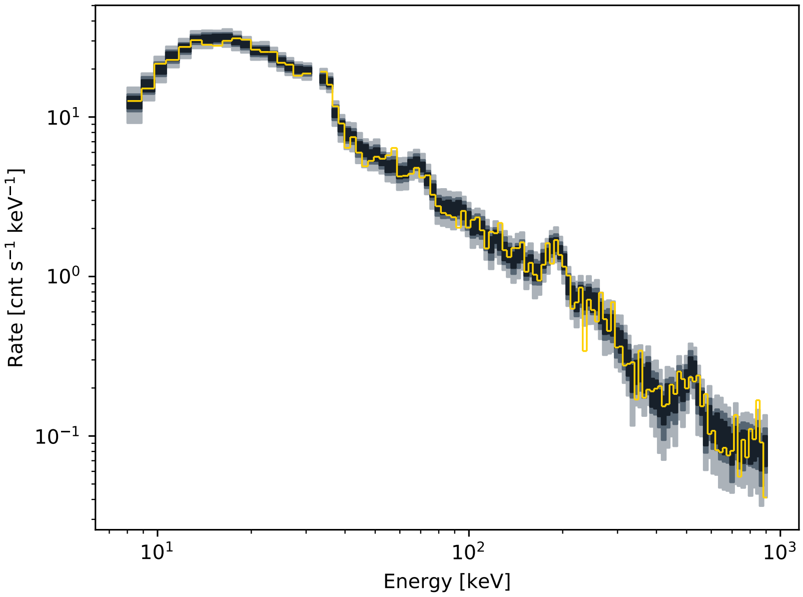

Figure 3.2: An example of PPC plot, used later in Chapter 5 to assess the goodness of the fitted model. The yellow line denotes the observed counts, while the gray regions indicate, from darker to lighter, the 68% and 95% credible regions for each bin.

As one can see, if the model fits the data well, the real counts are almost always falling inside the chosen credible region (usually the 95% one is used, though this is to some extent arbitrary). Nonetheless, this approach allows for a quick and reliable identification of poor fits and is especially useful in case of models depending simultaneously on many parameters, where otherwise some kind of summary statistic would be needed.

Chapter 4

Improved GRBs localizations

4.1 Localizing with GBM

This chapter analyzes the improvements to the Gamma-ray Burst Monitor GRB localizations made possible by the use of a better fitting algorithm. Sec. 4.1 introduces the localization methodology, while Sec. 4.2 and 4.3 quantify the achieved improvement in performance and conduct a search for any possible remaining instrument systematic. Finally, Sec. 4.4 discusses some of the potential applications of the improved locations.
The standard fit methodology employed for GRB localization relies on the Daughter of Location (DoL) algorithm, which uses a χ^2 minimization technique to find the optimal source parameters. This implies that the locations published in the official catalogs are all computed by using DoL, unless any better measurement from another instrument is available (Paciesas et al., 2012; von Kienlin et al., 2014; Narayana Bhat et al., 2016; von Kienlin et al., 2020). In GBM, the observed counts include a background component, which for DoL is simply estimated with a polynomial fit and then subtracted from the total counts. This implies that background uncertainties are not taken into account during the fit. For each direction in the sky, the instrument spatial response is obtained by the interpolation of the original response grid of 272 points (generated through GEANT simulations), allowing the final spatial response matrix, amounting to a total of 41 168 points, to achieve a 1° resolution (Connaughton et al., 2015). Three of these tables are constructed through the use of different spectral templates, based on different (but fixed) spectral parameters' values, as shown in Tab. 4.1. Up to 2019, the template spectra were based on a Band function (Band et al., 1993), but, in response to the issues pointed out in Berlato et al. (2019) and Burgess et al. (2018), they have been recently changed to make use of a cut-off power-law model (Goldstein et al., 2019). This approach is however akin to simply fine-tuning the parameters to achieve a slightly better performance and does not solve the underlying issue of using only three spectral templates. Usually, the soft template is employed for solar flares and Soft Gamma-ray Repeaters, the moderate one for long GRBs and the hard one for short GRBs. Note that the only free parameter for the spectrum is the amplitude, which defines the overall normalization. For each of these templates, a χ^2 minimization is performed to find the most likely source position, i.e. the location most likely to produce the observed counts. The spectrum with lowest χ^2 is chosen as the best one. The 68% error radius is defined as the average distance of the points which lie at $\Delta\chi^2 = 2.3$ (Connaughton et al., 2015). Due to the spatial response grid resolution, a minimum value of 1° is assumed for the statistical uncertainty (Connaughton et al., 2015).

While DoL allows for very fast fitting, this approach is strictly speaking wrong due to its inherent inaccuracy, i.e. the inability of reproducing the real spectrum of the source.

Table 4.1: The previous Band function (left) and current cut-off power-law (right) spectral templates used by DoL (Connaughton et al., 2015; Goldstein et al., 2019).

Template	α	β	E_{peak} (keV)
Soft	-1.9	-3.7	70
Moderate	-1	-2.3	230
Hard	0	-1.5	1000

Template	α	E_{peak} (keV)
Soft	1.95	50
Moderate	-1.15	350
Hard	-0.25	1000

Whenever the real spectrum of the source deviates significantly from the templates, systematics are being introduced in the localization process. A better approach uses the newer and more advanced fitting algorithm, BALROG (BAyesian Location Reconstruction of GRBs), which is able to completely remove this issue thanks to a full fit, which reconstructs simultaneously both source's position and spectrum (Burgess et al., 2018). Compared to DoL, this method is much more computationally expensive, since every different source's parameters combination (both spectral and positional) requires a specific response that the code is generating dynamically while fitting. Such an approach to fitting wouldn't probably have been viable (or at least, not for rapid localizations) at the start of the mission, but with the much improved computational power now at disposal it is possible to run the code in $\sim 10 - 15$ min with parallelization ($\sim$16 CPUs). While BALROG also fits the background with a polynomial, it properly takes into account the uncertainties instead of relying on the incorrect procedure of background subtraction. The result of each BALROG fit is a posterior distribution, describing simultaneously both spectral and positional parameters of the source (Burgess et al., 2018). The "best" configuration of parameters is chosen as the one which maximizes the posterior distribution. The position distribution for a source is then obtained by simply integrating over the spectral parameters, see Fig. 4.1.

In Connaughton et al. (2015), the authors perform a study of the systematics through a comparison between the locations computed by DoL fits and the reference locations obtained by much more precise instruments, e.g. the *Swift* space telescope or the Fermi-LAT, or the ones obtained through triangulation by the Interplanetary Network (IPN). From the analysis performed, it was found that GBM locations are affected by systematics, which are empirically parametrized through the use of a combination of a two component model (or core-plus-tail, see Sec. 4.3 for more details), see Fig. 4.2. By convolving the original statistical error contour with this offset distribution, it is possible to recover the accuracy (i.e. the error contours capture the real location as often as they should) at the expense of the precision (much larger error region).

This approach however does not fix the fundamental issue of the DoL algorithm, which is the use of the spectral templates. Larger uncertainties can only hide the problem at best, but not fix it, since the fitted model requires more adaptability then what allowed by the use of templates. Moreover, the much larger error regions represent a serious drawback when performing searches for possible counterparts. Afterglow searches run into a much higher number of unrelated transients, while any e.g. neutrino search would see the significance of a hypothetical signal being decreased, since it gets "smeared" on a much larger region of the sky. In the following Sec. 4.2, the BALROG code performance is analyzed and compared to DoL's, while also performing a search for potential remaining instrument systematics.

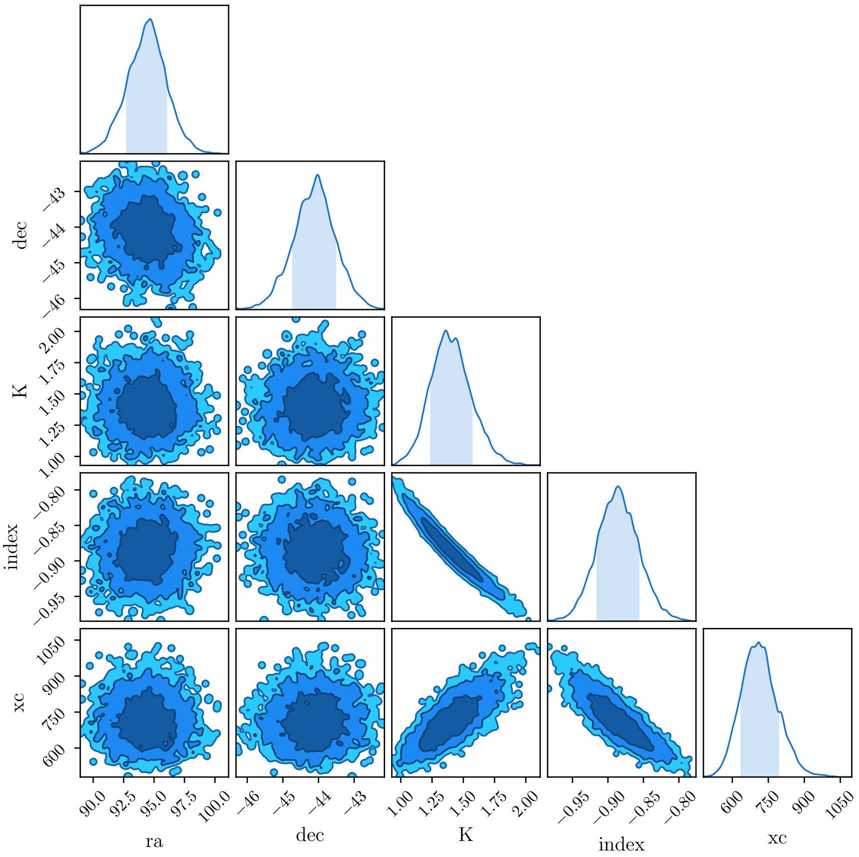

Figure 4.1: A corner-plot of the posterior distribution of the trigdat fit of GRB 090328.401. *ra* and *dec* represent the right ascension and declination of the burst, while K, *index* and *xc* are respectively the amplitude, spectral index and break energy of the fitted cut-off power-law. The distributions for the single parameters are obtained by integrating the full posterior distribution over the other source parameters.

4.2 BALROG localization performance

A study of the BALROG code performance and its comparison to DoL's is here presented. The sample used is the same as in Berlato et al. (2019) (see Appendix A), composed of 105 bright GRBs with known reference location, which is provided by the *Swift* space telescope. Swift localizations are much more constraining than GBMs, with typical uncertainties of the order of a few arcminutes for *Swift*/BAT (Barthelmy et al., 2005) and a few arcseconds for *Swift*/XRT (Burrows et al., 2007). In comparison, typical GBM positions have statistical errors of the order of a few degrees. As such, the uncertainties of the reference locations are neglected in the analysis here performed. Of the 105 GRBs in the sample, 69 are triggers with a DoL location, which can be compared to the BALROG location to assess the comparative performance of the two methods. The remaining 36 bursts do not have a public DoL position, but are nonetheless used to increase the sample size for systematics searches, see Sec. 4.3. The bright bursts selected for the sample satisfy the following cut in fluence S and peak flux F_{peak}:

$$F_{peak} > b - a \cdot S \ , \tag{4.1}$$

where $b = 6\ \mathrm{cm}^{-2}\mathrm{s}^{-1}$ and $a = 0.857 \cdot 10^{5}\ \mathrm{erg}^{-1}\mathrm{s}^{-1}$. This cut, which is to some extent arbitrary, is meant to strike a balance between a large enough sample and events with sufficiently small statistical uncertainties. The small statistical errors are fundamental for

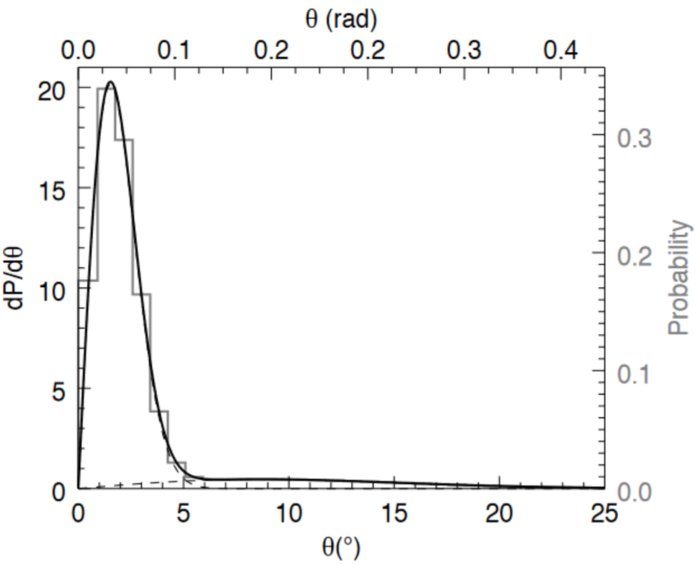

Figure 4.2: A fit of GBM systematics with a two component Fisher-von Mises model for a single spacecraft quadrant. In general, systematics were found to be spacecraft coordinates dependent. Image from Connaughton et al. (2015).

this analysis, as any possible systematic would be very hard, if not impossible, to detect if the statistical error is the dominating contribution.
For the scope of the comparison between the two algorithms, it is of interest to estimate both the precision and accuracy of the computed locations. The former is estimated as the angular separation between *Swift* and GBM positions, while the second uses a quantity here defined, the σ level, which quantifies the ability of the error contours to capture the real location. In practice, this means that, if the positions are perfectly accurate and a large enough sample is available, the e.g. 68% probability contour provided by the posterior should capture the real location 68% of the times, the 95% probability contour would capture the real location 95% of the times and so on. In all generality, for each GRB of the sample both a position distribution from the fit and a *Swift* location are available. This reference position lies on some probability contour C_R of the location distribution, where C_R defines a curve which points have equal probability density. Integrating the region inscribed by C_R yields a probability, given by the following equation

$$p = \int_{C_R} P(\phi, \theta) d\phi d\theta \tag{4.2}$$

where ϕ and θ are the two angular coordinates. This probability value can be converted to the usual σ notation used for gaussian distributed quantities, i.e. 1σ corresponding to 68% probability, 2σ corresponding to 95% probability and so on. To compute the σ level, it is sufficient to invert the following equation:

$$p = \int_0^{\sigma} \frac{2}{\sqrt{2\pi}} e^{-\frac{x^2}{2}} dx \tag{4.3}$$

where a half-gaussian is used due to the fact that angular offsets are positive definite. Following this definition, it is possible to compare both offset and accuracy for BALROG and DoL, as shown in Fig. 4.3. BALROG is able to simultaneously improve both precision and accuracy of the locations provided by GBM. In particular, GRBs with very large offsets (> 10°) are not present with the BALROG code, while with DoL there are two of these cases, with angular separations of ~16° and ~19° (not shown in Fig. 4.3). BALROG is also more accurate, as visible from the more rapidly rising cumulative distribution

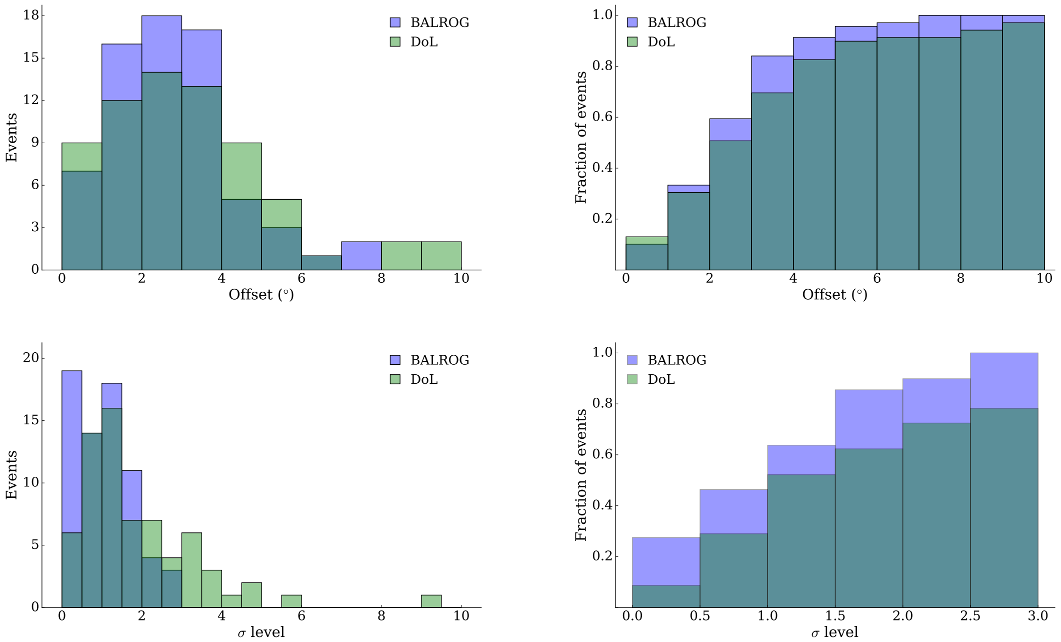

Figure 4.3: Performance comparison between BALROG and DoL. On the top, the offset and its cumulative distribution are shown. On the bottom, the same plots for the σ level are visible.

function (CDF) in Fig. 4.3, due to the fact that it is able to remove all of the outliers, i.e. the bursts where the mismatch between templates and actual spectrum is very large.

Fig. 4.4 shows instead the difference for the offsets and σ levels achieved by DoL and BALROG. One can see that most of the data points favor BALROG (positive values in the plots), due to its ability to remove very inaccurate locations. There are of course instances where DoL is able to achieve slightly better results, but this is only due to statistical scatter: just by chance some measurement happen to be closer to the real value. One can see that, on a sample basis, BALROG always performs in a better or comparable way with respect to DoL.

In Fig. 4.5, the fitted locations are also shown in spacecraft coordinates. The majority of the positions are located in the upper hemisphere due to the fact that most of the lower hemisphere is occulted by the Earth, though not in a constant way due to the spacecraft rocking motion.

4.2.1 BALROG localizations with spectral templates

The DoL fitting method can conceptually be thought as a subset of the BALROG algorithm, where instead of allowing for the simultaneous fitting of position and spectrum, all of the spectral parameters (expect the amplitude) are set to fixed values. It is of interest to see how much of a performance change is present when using the BALROG code with spectral templates. This comparison is performed only for the Band templates, but qualitatively speaking the results will be similar for the more recent cut-off power law templates (see Tab. 4.1) introduced in Goldstein et al. (2019), since roughly speaking they can be thought as a tweaking of the previous templates, but ultimately do not improve in any way the overall flexibility of the method, which still relies on only three distinct spectral shapes. For each GRB, the three Band templates are fitted with the BALROG code and the best one is kept as a final location for the burst. The results of the comparison are shown in Fig. 4.6 and, as easily noticeable, the use of the templates yields a far worse

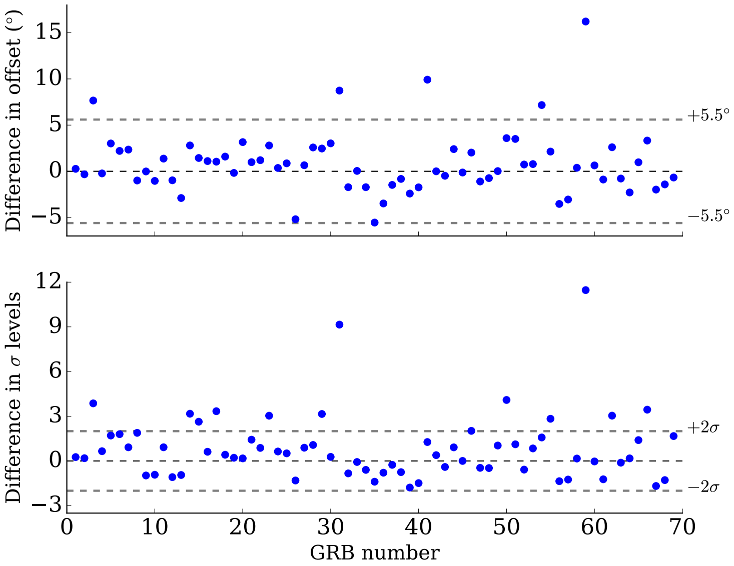

Figure 4.4: Effects of statistical scatter on the localizations. On the top is shown the difference between DoL's and BALROG's offsets, while on the bottom is the same but for the σ level. Positive values imply a worse performance for DoL and negative values a worse performance for BALROG.

localization performance due to the loss of flexibility of the model.

4.3 Search for systematics

Through the use of the BALROG code it is possible to remove the systematics which are intrinsic to the wrong methodology used by DoL, i.e. the use of spectral templates. Nonetheless, this does not guarantee that the instrument is completely free of systematics. This section conducts a further investigation to search and quantify any possible remaining systematic component in GBM. As mentioned in Sec. 4.1, a similar study was performed in Connaughton et al. (2015), where systematics were found and estimated empirically through the use of a core-plus-tail model, that is a combination of two Fisher-von Mises distributions, which are individually described by the following equation (Connaughton et al., 2015)

$$F = \frac{k}{e^k - e^{-k}} e^{k \cos\delta} \tag{4.4}$$

where δ is the offset between fitted and reference location and k is the concentration parameter, which controls how broad or tight the distribution is. This core-plus-tail is then defined as a linear combination of two Fisher-von Mises distributions $F_{tot} = a_1 F_1 + a_2 F_2$, with the two components peaking respectively at 3.7° and 14.3°. The first component contains 90% of the total probability ($a_1 = 0.9$), while the tail contains the remaining 10% ($a_2 = 0.1$). Furthermore, Connaughton et al. (2015) found evidence of this systematic component being dependent on the source position relative to the spacecraft. These results are however heavily affected by the use of a wrong methodology for source reconstruction and are thus not a good benchmark for the presence of "true" systematics, dependent on the instrument response and not on an incorrect algorithm.

To check for the presence of remaining systematics in GBM, it is necessary to assess whether the localizations provided by BALROG are statistically accurate. The σ level should, in absence of systematics, be asymptotically (that is with a large enough sample)

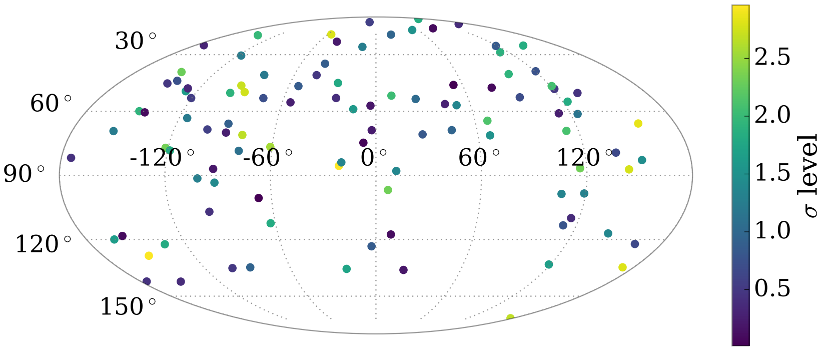

Figure 4.5: The distribution of the reconstructed locations in spacecraft coordinates. The horizontal axis shows the azimuth angle, with the b0 and b1 detectors pointing respectively at 0° and 180°. The vertical axis shows instead the zenith angle, with 0° corresponding to the LAT boresight.

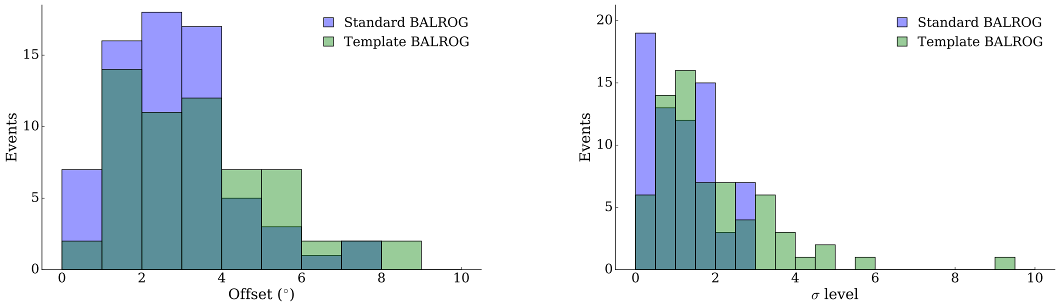

Figure 4.6: Performance comparison between standard and template BALROG. The offset distribution is shown on the left, while on the right is instead the σ level distribution.

distributed as a half standard normal. The comparison between expected and achieved cumulative distributions for the σ level is shown in Fig. 4.7.

As visible, a discrepancy is clearly present within the two. It is however not straightforward to assess whether the difference arises due to the presence of systematics or due to statistical fluctuations. The sample here utilized is still rather small and large statistical fluctuations are to be expected. The possibility of this difference arising purely from statistical fluctuations is discussed more in detail in Sec. 4.3.1.

There are various potential reasons which could cause the observed discrepancy, which are here investigated. One possibility is the emission from the Earth's limb is affecting negatively the localization quality. The Earth is a bright source in the gamma-rays in GBM's energy window, though its effect is already taken into account by the background fit performed by either BALROG or DoL. More likely to cause issues in the locations are possible inaccuracies in the Earth scattering model (see Sec. 2.3). To verify that, one can plot the dependence of the offset angle and σ level on the minimum angle between the detectors' boresight and the Earth's limb, as in Fig. 4.8. If the Earth is affecting negatively the locations, there should be a noticeable pattern, though this does not seem the case.

The procedure is also performed for the Sun angle, and again no particular change in location quality is visible, see Fig. 4.9. Except during solar flares, the gamma-ray emission from the Sun seems negligible.

It is also possible to investigate whether the observed discrepancy arises from specific

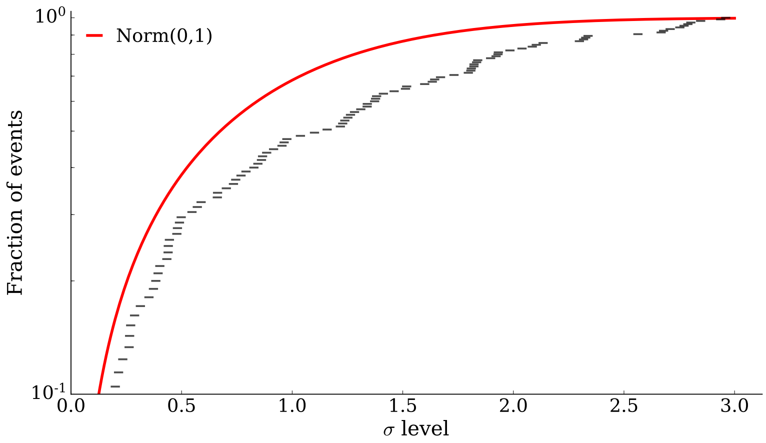

Figure 4.7: The cumulative distribution function (in log scale) of the σ level for the sample locations (in black) and the expected behavior of the distribution (in red) from a half standard normal.

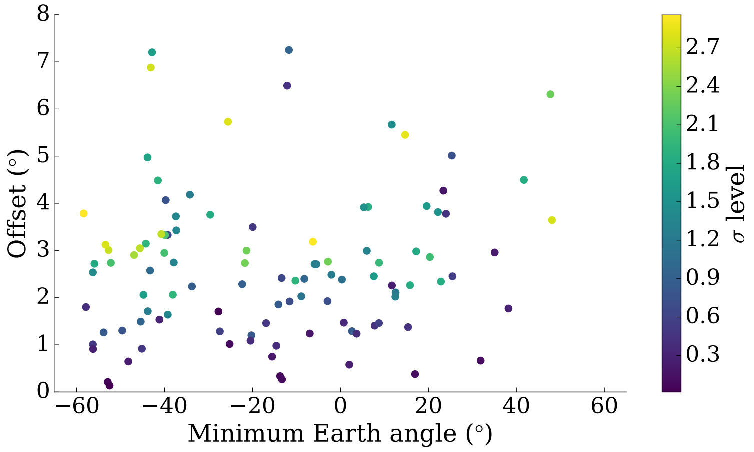

Figure 4.8: Dependence of offset and σ level on angular separation between the Earth's limb and the detector boresight. Negative angles represent detectors pointing inside the Earth's limb.

detector combinations or parts of the spacecraft. A first simple check which can be made is to see if any specific detector pair (i.e. combination of two detectors) is particularly underperforming in terms of offset and σ level, as shown in Fig. 4.10.

Note however that a different performance for the pairs does not necessarily arise from the presence of systematics. Due to the different orientations and mounting points of the detectors, some pairs are less likely to be used together and are worse performing due to the average weaker signal-to-noise ratio. As expected, one can see that for the most part detectors from the same side of the spacecraft are much more likely to be used together in a localization (see Fig. 4.10). From the plots it is also possible to see that the b0 side (detectors from n0 to n5) seems to be slightly underperforming compared to the b1 side (detectors from n6 to nb).

It is then of interest to investigate whether there are significant differences in the localization performance depending on the spacecraft coordinates of the burst. Such an issue could be present due to the asymmetric mass distribution in the satellite bus and correspondingly different spacecraft scattering components. To verify whether that's the case, one can check whether the positions obtained from the fit become systematically less accurate at particular azimuth and zenith angles. In Fig. 4.11, the dependence of the localization performance on the zenith angle is shown. Again, no clear pattern is visible,

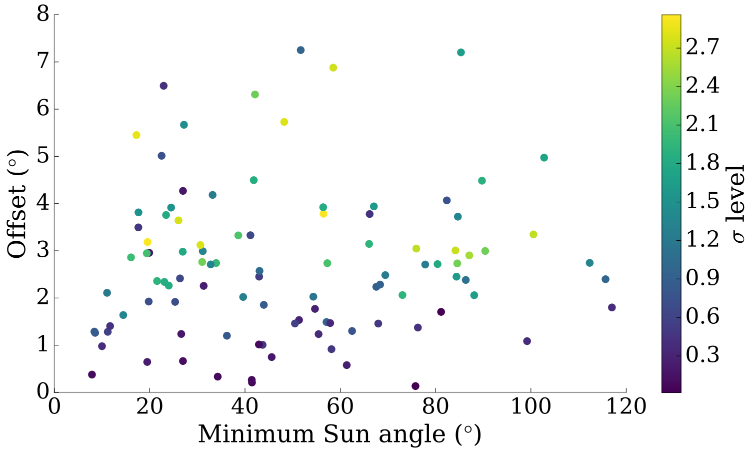

Figure 4.9: Dependence of offset and σ level on angular separation between the Sun and the detector boresight.

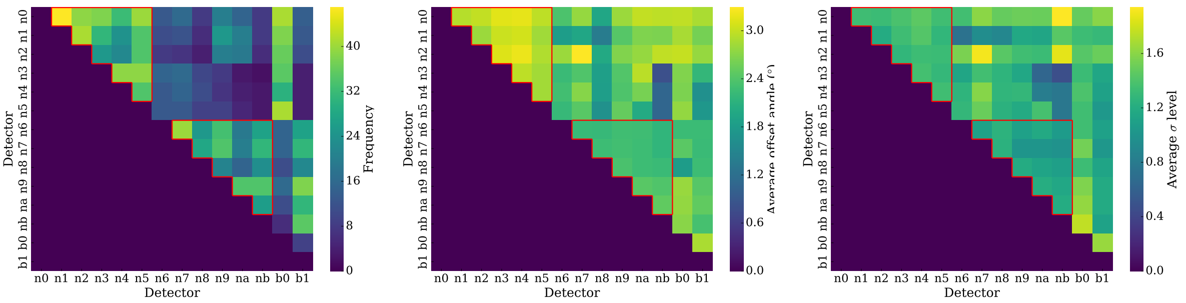

Figure 4.10: Color maps showing the performance of different detector pairs. On the right, the frequency with which each detector combination is used. In the center, the average offset achieved by each detector pair. On the right, the same but for the σ level. Groups of detectors on the same side are marked by a red contour.

though there seem to be slightly more events with larger offsets at larger zenith angles. This is not however evidence for the presence of systematics, but only the effect of the larger statistical fluctuations due to the weaker signal-to-noise ratio for such events, since GBM is optimized to detect events from the top hemisphere of the spacecraft. Furthermore, from Fig.4.11 one can see that such events, even if affected by larger uncertainties, are still accurately localized.

The same performance check can be done for the spacecraft azimuth angle, as shown in Fig. 4.12. Here it is again possible to see some differences between the two sides of the spacecraft, in a similar way as to what already seen in Fig. 4.10. Localizations on the b0 side (at 0°) seem to present larger offsets and also slightly larger σ levels. The same issue is also present close to 90°/270°, where the solar panels are located, possibly hinting to some inaccuracy in the spacecraft mass model.

To further investigate the asymmetry in performance, it is possible to divide the locations in the sample in three different sets:

1. **b0 side**: localizations obtained only by using the detector subset n0, n1, n2, n3, n4, n5 and b0.
2. **b1 side**: localizations obtained only by using the detector subset n6, n7, n8, n9, na, nb and b1.
3. **both sides**: localizations obtained with detectors from both sides of the spacecraft.

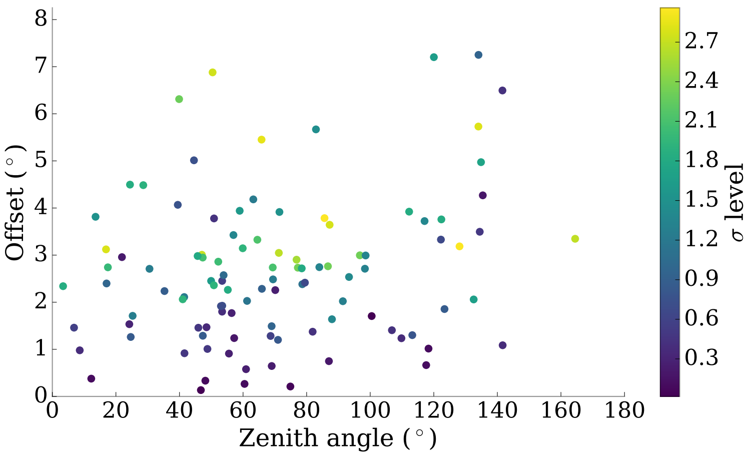

Figure 4.11: Offset and σ level in function of the spacecraft zenith angle. Here 0° corresponds to the LAT pointing direction, while 180° points right below the spacecraft.

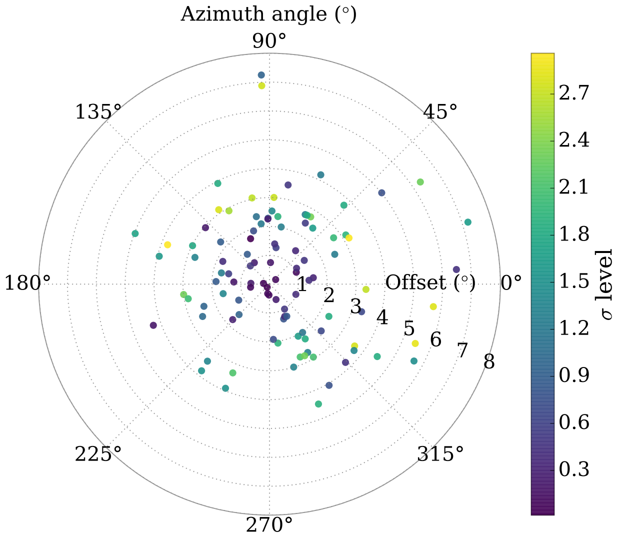

Figure 4.12: Offset and σ level in function of the spacecraft azimuth angle. Detectors b0/b1 are located at 0°/180°, while solar panels are situated 90°/270°.

By applying this classification to the sample, it is possible to check whether there is any difference in localization quality between the different sides of the spacecraft, as shown in Fig. 4.13. One can immediately notice how localizations with detectors from both sides are overall much less accurate compared to the single-side only locations, possibly due to the scattering of photons on the solar panels or other parts of the spacecraft which are unaccounted for in the mass model.

A further comparison between the position obtained by using only detectors on the b0 side and the b1 side produces Fig. 4.14. Here the difference between the two sides becomes clearly noticeable, with the b0 side showing both larger offsets and σ levels.

This is also visible in the CDFs, as shown in Fig. 4.15, although the discrepancy between the two sides is considerably smaller than the one with the localizations obtained by both sides.

Since from each location fit a full posterior distribution is obtained, it is possible to extract even more information from the data. The position distribution, which is obtained by marginalizing the posterior over the spectral parameters, can be used to compute an

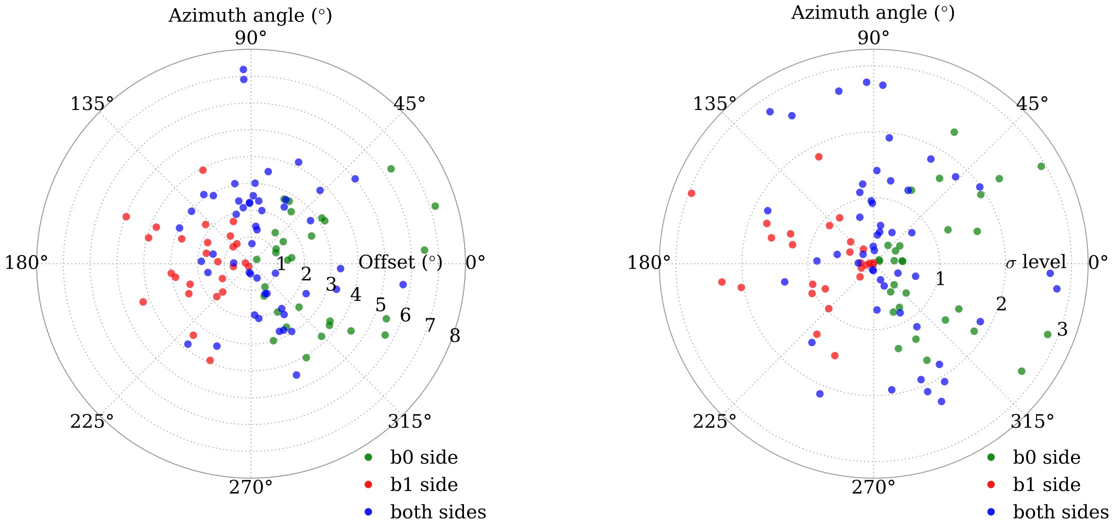

Figure 4.13: Offset angle (left) and σ level (right) in function of the spacecraft azimuth angle. Detectors b0/b1 are located at 0°/180°, while solar panels are situated 90°/270°.

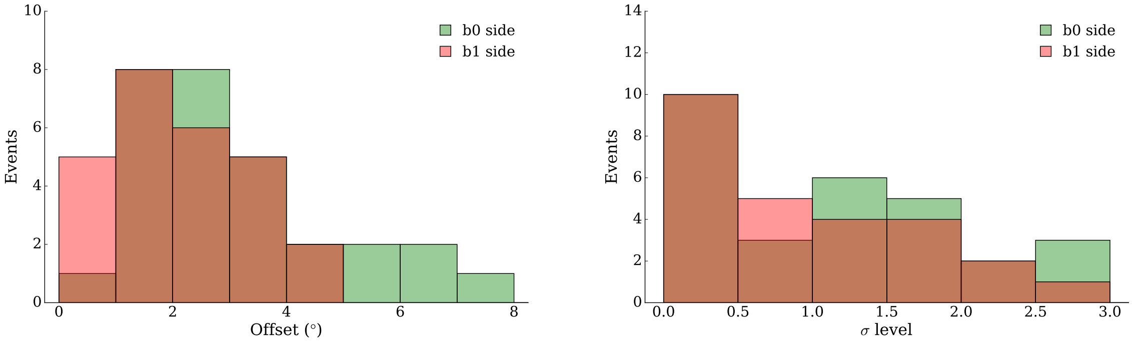

Figure 4.14: Offset (left) and σ level (right) comparison for the b0 and b1 side.

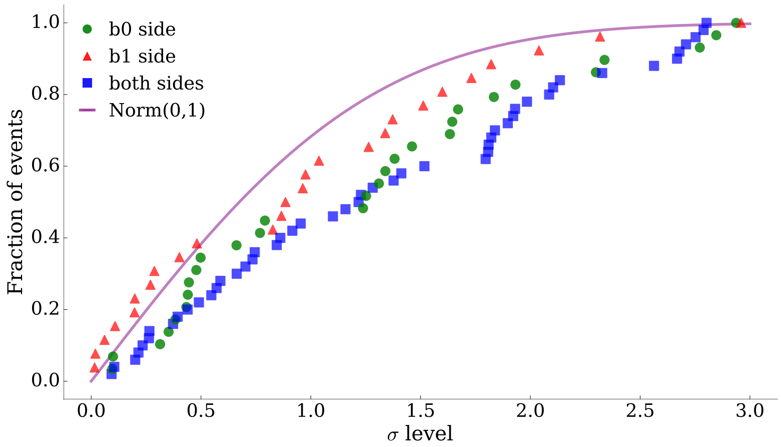

Figure 4.15: Comparison between the cumulative distribution functions for the different sets. The purple line denotes the expected behavior from a standard normal CDF.

offset distribution simply by calculating the offset between each point of the position distribution and the *Swift* reference location. Each of these distributions can be thought as a sample of a larger "global" offset distribution, which describes the overall localization performance for GBM. The achieved distributions are shown in Fig. 4.16. Again, the discrepancy in performance between the two sides is easily noticeable, with the b1 side yielding overall better locations. Note also that, compared to Connaughton et al. (2015), the offset distributions are not found to be compatible with a combination of Fisher-von Mises distributions.

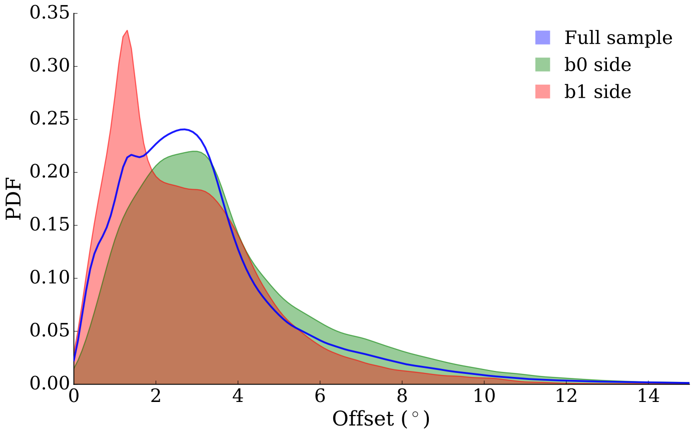

Figure 4.16: Global offset distribution for the full sample (blue) and for the two opposite spacecraft sides (red and green).

4.3.1 Systematics and statistical fluctuations

As last step of this analysis, it is necessary to assess whether the observed discrepancies are compatible with simple statistical noise due to the sample size or are actually a symptom of true systematics. This check can in practice be performed through the use of a simple Monte Carlo by simulating many samples of equal size as the original. By binning the synthetic data in the same way as the real one, one can define probability intervals which encompass the expected range of values for each bin. This process is performed for both the full BALROG sample (all 105 GRBs) and the reduced DoL sample (69 GRBs),

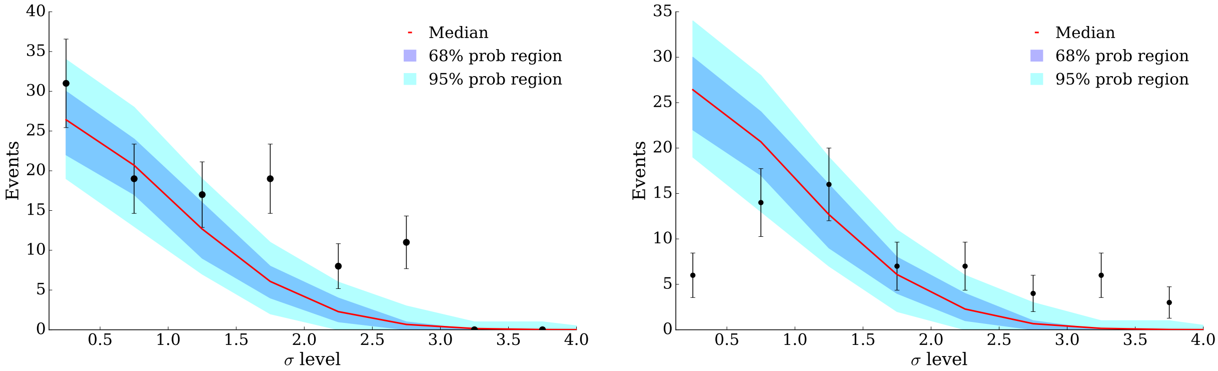

Figure 4.17: Comparison between the percentile regions of the simulated datasets for the data points from BALROG (left, all 105 GRBs) and DoL (right, 69 GRBs) locations.

the results of which are shown in Fig. 4.17. As one can see, both of the datasets display bins which are incompatible with the probability regions defined by the expected (i.e. assuming no systematics) half standard normal distribution. The discrepancy is most significant in the tail (2.5-3 σ) for BALROG, while for the DoL sample it is present both at small and large σ. Even with the proper statistical treatment possible with BALROG, a systematic component still survives. This implies that the instrument response, or at least one of its components, is inaccurate.

Finally, while it is impossible to properly estimate the systematics without identifying their cause, it is at least feasible to provide a rough estimate of their "average" effect on the sample, i.e. to compute some form of constant correction to apply to the sample CDF to bring it closer to expected CDF behavior. Here a quadratic sum is adopted for the sake of simplicity, but it should be noted that this does not constitute a proper estimate of the systematics, which in general act in a different, unknown way on each GRB, but merely a rough estimation of their effect. Thus, by performing this procedure, the "corrected" CDFs of Fig. 4.18 are obtained. As shown, roughly speaking the systematics correspond to an error of $\sigma_{sys} \sim 1-2^{\circ}$, depending also on the subset being considered, with locations from the b0/b1 sides being overall more accurate then the ones from the solar panels' sides.

The remaining systematics are most likely a product of an inaccurate response, though it is hard to pinpoint which components exactly. Based on the fact that the Earth separation angle (see Fig. 4.8) doesn't seem to contribute too much to the inaccuracy of the position, one can infer that the systematics are for the most part coming from either the direct detector response or the spacecraft scattering model. The detectors were however accurately calibrated on ground and, while they are known to have an an azimuthal dependence in their effective area (up to ~10%), this cannot account for the discrepancy observed. The remaining systematics are most likely arising from inaccuracies in the spacecraft mass model. As shown in Fig. 4.13, localization performed by using detectors on both sides seem to be less accurate. This may actually be caused by the presence of the solar panels on the sides or by inaccuracies in other parts of the spacecraft mass model, which is not available to the public, making further investigations of the systematics very hard.

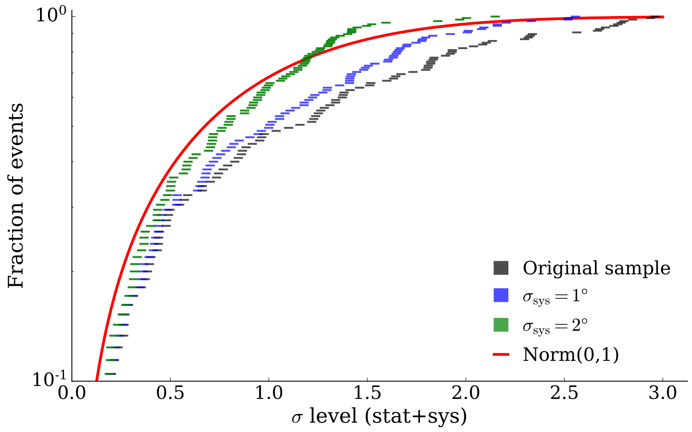

Figure 4.18: BALROG CDF with different systematic errors summed in quadrature to the statistical uncertainty. The y axis is in log scale.

4.3.2 Systematics and size of the error regions

With a rough estimate of the systematics at disposal, it is finally possible to also compare the typical size of the error regions for the locations computed by the two algorithms. While both of the methods ultimately suffer from systematics, BALROG locations are affected to a far lesser extent. According to the analysis done in Connaughton et al. (2015), the core-plus-tail model corresponds to a $2\sigma_{sys} \sim 16°$ systematic error, computed as the 95% containment interval for the offset distribution. This corresponds to an increase in the size of the error region of $\pi(2\sigma_{sys})^2 \sim 800\ \mathrm{deg}^2$. Conversely for BALROG, the systematics increase the size roughly by $\pi(2\sigma_{sys})^2 \sim 50\ \mathrm{deg}^2$. There is thus a significant improvement in terms of the size of the error region over DoL (see for example Fig. 4.19), which allows for faster and more reliable multi-wavelength and multi-messenger searches.

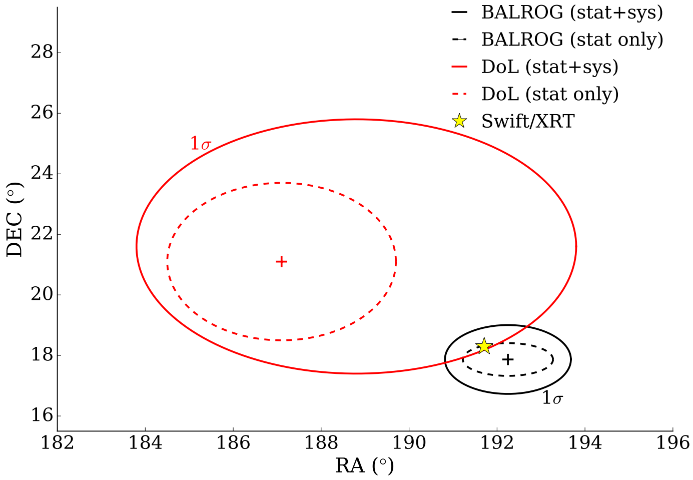

Figure 4.19: Location of GRB 170705.115, an example of the different sizes of the final error contours once systematics are taken into account. BALROG is able to consistently achieve more accurate localizations while still retaining smaller error regions. The systematics component here considered is 1° due to the direction of the burst in spacecraft coordinates. Figure from Berlato et al. (2019).

The only potential drawback of BALROG would be its speed, but with current hardware locations are regularly computed on a timescale of $\sim$ 30 min: 10 min for the data to be available plus another 10 – 20 min for fitting and quality checks. Furthermore, an automated version of the algorithm has been developed at the Max Planck Institute for Extraterrestrial Physics and it allows regular rapid localization of GRBs with minimal human intervention (see https://grb.mpe.mpg.de/). Locations are openly available to the community and, in case of more interesting bursts, are also distributed through the Gamma-ray Coordinates Network (GCN) with email alerts. All of the automated BALROG localizations have been publicly available since January 2019. Since then, 36 GRBs have been detected by both GBM and *Swift*: a limited, but still significant sample which allows to assess the performance of the automated BALROG positions, as shown in Fig. 4.20, which already includes the systematic component in its uncertainties. Similarly to what seen in Fig. 4.18, one can once again see that there seems to be a small remaining systematic component, which most likely arises due to imperfections in the automatic selection algorithm responsible, among other things, for selecting the time intervals to be used for the background fits. Their occasional inaccuracy can cause the discrepancy visible in the CDFs of Fig. 4.20. Note however that such issues are unique to the automated algorithm and are instead not present in the "human" locations previously discussed in this chapter, where all of the selections are done manually.

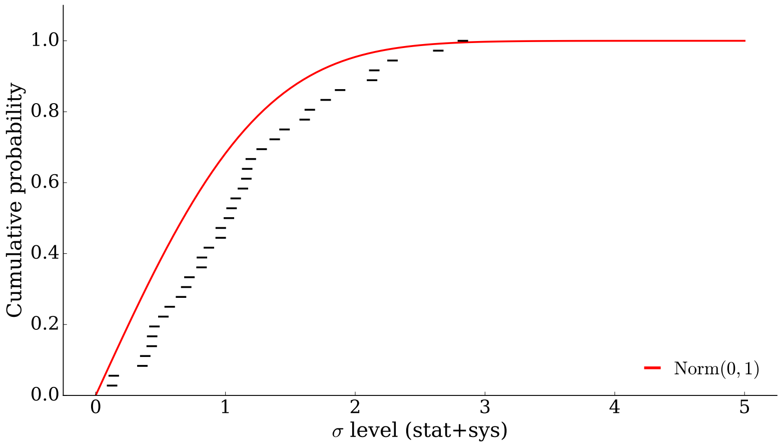

Figure 4.20: The cumulative distribution function of the 36 *Swift* GRBs localized by the automated BALROG algorithm. Systematic uncertainties are already included in the σ level calculation. The red line denotes the expected CDF behavior in absence of systematics.

4.4 Conclusions and further studies

The methodology introduced by the BALROG code is able to significantly improve the localization performance of Fermi-GBM, increasing the accuracy (by removing most of the systematics) and reducing the size of the error regions of the reconstructed positions. These improvements bring a series of benefit to GRB observations, ranging from the increased chances of successful afterglow detections to the more constraining multi-messenger searches. In this regard, neutrino searches are of particular interest in the scope of this thesis. As previously discussed in Sec. 1.5, GRBs represent good candidates to explain part of the observed astrophysical neutrino flux in IceCube. So far, the standard approach for GRB neutrino searches has been to apply simple time window selections (wide enough to include the whole burst plus some extra margin) and then compare the locations of the burst and any potentially remaining neutrino. These searches have been unsuccessful up to now (see e.g. Aartsen et al. (2016); Coppin and van Eijndhoven (2019)), which may simply depend on the use of overly simplistic time cuts together with locations affected by systematics, thing which would greatly decrease the probability of a successful detection. To understand why that is the case, assume that there is a simultaneous detection of neutrinos and gamma-rays from a GRB. Since the standard GBM locations have inflated uncertainties to compensate for DoL's systematics (arising for the vast majority from a wrong fitting methodology), any neutrino signal falling inside the error region would see its significance greatly decreased due to the fact that a larger sky area implies a much greater probability of chance coincidence (i.e. cannot distinguish between background and signal neutrinos). This would imply that, even if there is a simultaneous detection, it would be impossible to correctly identify it. The improved GBM locations provided by the BALROG code can thus increase the chances of a successful detection, if a real signal is present in the data. If not, the improved positions can still be used to better constrain the neutrino flux from GRBs, which is nonetheless helpful for modeling the emission mechanisms.

Further studies performed by von Minckwitz (2020) also analyze the impact of wrongly reconstructed locations on the spectra. This was done by considering a sample of simulated GRBs and randomizing their positions, that is by introducing an offset from the true location. The generated response is thus inaccurate and introduces systematics in the fitting process, which affect the estimated spectral parameters in a complex and a priori unknown way. The problem is of a certain difficulty due to its high dimensionality: the fit results are affected both by source spectrum and position (with respect to the spacecraft frame), but also by which of the detectors are chosen for the fit and their signal-to-noise ratio. In von Minckwitz (2020) it was found that a wrong position can introduce significant systematics in the spectrum (see e.g. Fig. 4.21), particularly for bright GRBs, where the statistical uncertainties are already small. This effect is present for all of the spectral parameters, but it is particularly pronounced for peak energy and fluence of the burst, fact which may have important consequences on studies relying on these parameters, if they are estimated through a GBM position.

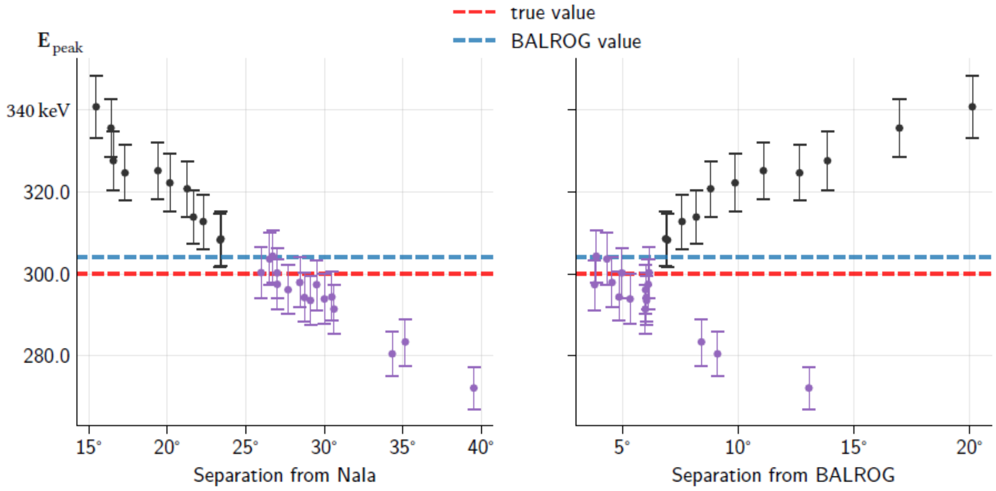

Figure 4.21: The impact of wrongly reconstructed locations on the fitted E_{peak} of a Band function. The plot displays how an increasingly larger offset from the brightest detector (left) and from the BALROG position (right) affect the estimated value of E_{peak} for a bright GRB. The dashed lines denote the fitted E_{peak} value for the true position (in red) and for the BALROG position (in blue). The purple points indicate synthetic locations where the distance from the second brightest detector NaI B is kept fixed, but the separation from the brightest one NaI A is increased. Original figures from von Minckwitz (2020).

Chapter 5

Test of the photospheric emission model

5.1 Introduction

As seen in Chapter 1, the emission mechanisms in GRBs are still poorly understood. While in principle there are physical models which could explain the observations (such as optically thin synchrotron or photospheric emission), in practice so far they have only been tested to a very limited extent and conclusive evidence in favor of one or the other is still lacking. For most of the field's history, spectra have been fitted with simple empirical functions, such as the Band function, the main reason for this being the lack of computational power able to handle complex numerical models. It is however important to understand that tests performed with such methodology cannot substitute a real direct fit of a physical model to the data, as this "empirical" approach has been proven to provide inaccurate results when used for physical inference (Burgess et al., 2020). As seen in Sec. 1.3.3, a clear example of this is the synchrotron's line-of-death, where the low energy index α of Band function fits was found to be consistently violating the limits set by optically thin synchrotron emission (Preece et al., 1998). This result was then used as an argument against a synchrotron dominated emission and often also interpreted as indirect evidence for the presence of a photospheric component (Pe'er and Ryde, 2017). This methodology was however proven to produce unreliable results by Burgess et al. (2020), which found that fitting an optically thin synchrotron model directly to the data yields acceptable fits in at least 95% of the cases. Thus, similarly to what already done for synchrotron, the purpose of this chapter of the thesis is to perform an analogous study with the main competing model, that is emission from a dissipative photosphere.

While definitive evidence for photospheric dominated emission is still lacking, some GRBs have been found to be compatible with the presence of a thermal component, the most notable example being GRB 090902B (Abdo et al., 2009). This burst spectral shape is well fit by a strong thermal component, plus a weaker non-thermal one (Pe'Er et al., 2012), which suggests that photospheric emission may be dominant in at least some GRBs, see Fig. 5.1. Motivated by the presence of such GRBs, this chapter investigates the viability of the photospheric model.
So far, tests of the dissipative photosphere models have been performed only to a very limited extent, see e.g. Ahlgren et al. (2015, 2019a,b), due to the difficulties involved in generating a sufficient number of template spectra. Aiming to fill this gap, the model developed by Pe'er and Waxman (2005) is here tested on a sample of bright GRBs by generating a table model able to cover a large region of the parameter space. The model performance is then compared to the one achieved by Burgess et al. (2020) when testing optically thin synchrotron emission, allowing thus for the first time for a direct compar-

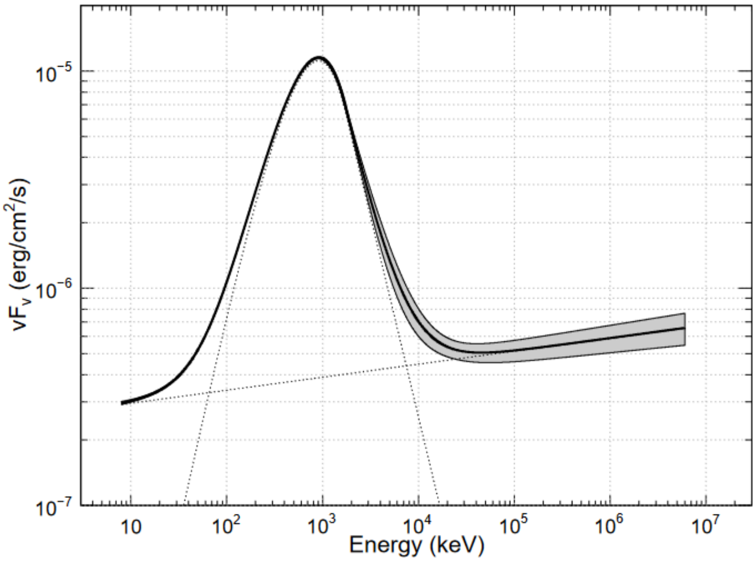

Figure 5.1: Original joint fit of GRB 090902B, performed by using data from both GBM and LAT (Abdo et al., 2009). The spectrum here fitted is composed of a Band function plus a power-law component. In the context of a dissipative photosphere model, these features can be identified as a thermal peak plus synchrotron and inverse Compton components (Pe'Er et al., 2012). Figure from Abdo et al. (2009).

ison of two different physical models on the same GRB sample. For the test to be as fair as possible, the sample here employed adopts the same binning, detector selections, background fits etc. as the analysis performed in Burgess et al. (2020).

The chapter is thus structured as follows. Sec. 5.2 provides a description of the model developed by Pe'er and Waxman (2005). Sec. 5.3 details instead how the table model is generated, the sample is selected and the fits evaluated. Sec.5.4 presents the results of the analysis, while Sec. 5.5 and Sec. 5.6 discuss the physical implications and the possible next steps.

5.2 The model

While there exist various different implementations of emission from a dissipative photosphere, the one here considered was developed by Pe'er and Waxman (2005). It is based on the standard fireball scenario (see Sec. 1.3.2 for a review) in which all of the energy is assumed to be released by a single dissipation episode (e.g. an internal shock). An interesting feature of the model is that it is able to describe not only the case of sub-photospheric dissipation, but also the scenario in which the dissipation takes place in the optically thin region beyond the photosphere, in which case synchrotron and synchrotron self-Compton (SSC) are expected to become more relevant. Which of the two scenarios is taking place fundamentally depends on where the dissipation occurs with respect to the photospheric radius. As shown in Fig. 1.8, the corresponding optical depth affects the spectral shape quite dramatically. Note that large optical depths ($\tau \gtrsim 100$) will result in a pseudo-blackbody spectrum, which is already known not to be compatible with the observations. This occurs due to the fact that any non-thermal component produced by the dissipation episode will end up being thermalized, if occurring deep beneath the photosphere.

From a physics standpoint, the model includes all the relevant electron-photon pro-

cesses, such as synchrotron emission, Compton scattering, synchrotron self-absorption, pair production/annihilation etc. Interactions between nucleons and pion production are instead here not considered. In the model, protons are thus assumed to have negligible interactions with the rest of the plasma, although they still constitute the bulk mass of the outflow. The model described by Pe'er and Waxman (2005) assumes the outflow to be composed by a uniform plasma made of electrons, positrons, photons and protons. The dissipation process is assumed to take place on a time scale equal to the dynamical time $t_d \sim R/c$, with R characteristic length scale of the plasma. The evolution of the various particle species is followed until the end of the dynamical time, after which the photons can escape immediately if $\tau < 1$. In the case $\tau > 1$, the plasma is still optically thick and the photons cannot be released right away, in which case it is here assumed that the fireball expands adiabatically until reaching $\tau = 1$. At this point, the photons are finally released. In practice, this corresponds to applying adiabatic cooling to the photons, which is here modeled as a factor $A = 2\tau^{-\frac{2}{3}}$ (Vurm and Beloborodov, 2016) acting on the photon energies (and thus also modifying their distribution).
The evolution of the different particles species and their interaction with each other are tracked by making use of Fokker-Planck equations (Pe'er and Waxman, 2005). Electrons are assumed to follow a two component distribution: a fraction of them is accelerated (i.e. non-thermal), and thus follows a power-law distribution, while the rest remains thermal. Finally, note that the model does not include any jet geometry (thus effects like geometrical broadening are not considered) or any dynamical prediction, i.e. there's no prediction regarding the spectral evolution.

The spectrum generated by the code depends on the 9 following physical parameters:

1. ϵ_e: the fraction of the dissipated energy carried by the electrons.
2. ϵ_B: the fraction of the dissipated energy carried by the magnetic field.
3. ϵ_d: the fraction of the total energy which is dissipated.
4. ϵ_{pl}: the fraction of the electrons following a power-law distribution. The remaining $1 - \epsilon_{pl}$ is thermally distributed.
5. r_d: the radius at which the dissipation takes place.
6. r_0: the radius at the base of the outflow.
7. Γ: the Lorentz factor of the ejecta.
8. L_{GRB}: the total isotropic luminosity of the fireball emitted by the central engine.
9. p: the index of the power-law distribution of the electrons.

Given the relatively large number of parameters, the computation of a table model can be quite challenging. To keep the number of spectra to a manageable level, 4 of the 9 parameters were fixed. The dissipation efficiency was thus set to $\epsilon_d = 0.05$, which would be a standard value for e.g. an internal shock scenario, where typically $1\% \lesssim \epsilon_d \lesssim 10\%$ (Piran, 2004; Pe'er, 2015). r_0 is fixed to the value of 10^7 cm, representing a "generic" size of the inner engine (Pe'er, 2015). Finally, it is assumed $\epsilon_{pl} = 0.1$ and $p = 2.24$ (canonical relativistic shock prediction (Kirk et al., 2000)).

The other 5 parameters are used to set up a grid of points with the following values:

- $\epsilon_e = [0.3,\ 0.6,\ 0.9]$

Table 5.1: Example of fit results for a simulated spectrum at z=0.1. In the figure, two of the marginal distributions for the fit parameters are shown. As can be seen, the fitted values are consistent with the simulated ones.

Parameter	Simulated	Fitted
ϵ_e	0.8	0.80 ± 0.06
ϵ_B	10^{-2}	$(1.03 \pm 0.03) \cdot 10^{-2}$
r_d (cm)	10^{13}	$(1.1 \pm 0.1) \cdot 10^{13}$
Γ	200	200.3 ± 0.4
L_{GRB} (erg/s)	10^{54}	$(1.01 \pm 0.02) \cdot 10^{54}$

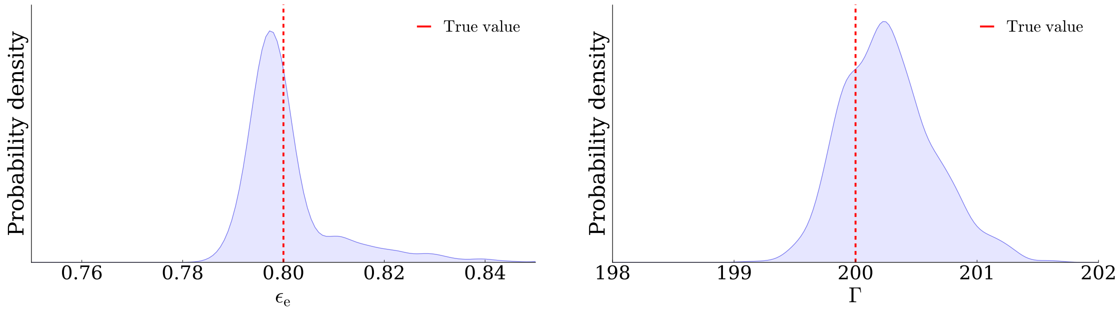

Figure 5.2: Marginal distributions for ϵ_e and Γ for a simulated spectrum. The distributions are found to be able to consistently reproduce the real parameter values.

- $\epsilon_B = [10^{-6},\ 10^{-4},\ 10^{-3},\ 10^{-2},\ 10^{-1}]$
- $r_d = [10^{12}, 10^{13},\ 10^{14},\ 10^{15},\ 10^{16}]$ cm
- $\Gamma = [50,\ 100,\ 150,\ 200,\ 250,\ 300,\ 350,\ 400,\ 500,\ 600,\ 700,\ 800,\ 900,\ 1000]$
- $L_{GRB} = [10^{50}, 10^{51}, 10^{52}, 10^{53},\ 10^{54},\ 10^{55}]$ erg/s

which corresponds to a total of 6300 numerical spectra.
Compared to the previous studies done in Ahlgren et al. (2019a,b), one of the main differences is that this implementation of the photospheric model releases the assumption of a fixed optical depth ($\tau = 35$ in previous works), which allows for more flexibility in the model in adapting to different spectral shape, see 1.8. Additionally, this allows the model to describe the cases for both sub-photospheric and optically thin dissipation scenarios, depending on where the dissipation takes place with respect to the photosphere. A more detailed comparison between the previous studies and the analysis here presented is reserved for Sec. 5.5.

5.3 Sample selection and fitting methodology

Before fitting the real data, the fitting method was tested onto synthetic datasets, so to make sure that the results are consistent. The table model fits are found to reliably reproduce the simulated values, as shown in Tab. 5.1. In the example, the synthetic spectra is set at small redshifts so to provide large count statistics in the detector and thus small parameter uncertainties, which allow to perform a strict test in terms of the accuracy of the fitting method. Note that typical parameters' errors for the real bursts are much larger. Fig. 5.2 also show an example of the marginal distributions for two of the parameters.

As for the chosen sample, it is the same as the one used in Burgess et al. (2020), constituted of 19 GBM time resolved GRBs, corresponding to a total of 162 spectra (see Tab.

5.2). These GRBs present high signal-to-noise ratio, which allows for more constraining parameter estimation. All of the bursts also have a known redshift, which has two important implications:

1. It allows to correct for the cosmological effects and to assess the true burst energetics. This is strictly speaking a requirement when trying to fit directly for the true luminosity of a GRB, as in the study here performed.
2. It implies that a very precise location is available from optical observations. Position uncertainties become thus negligible, with typical values below a few arcseconds. Errors of this order of magnitude have no real effect on the spectral analysis, thus for all practical purposes the estimated position can be treated as the real location of the source.

The choice to employ the same sample stems from the fact that this allows for a direct comparison between the two different physical models. Moreover, the fact that the selected bursts' lightcurves present a single-contiguous pulse, implies that they are compatible with the assumption of a single dissipation episode from Pe'er and Waxman (2005). The sample is mainly constituted by GBM-only data, but three bursts also present LAT Low Energy (LLE) detections, see the events marked by an asterisk in Tab. 5.2.
For the calculations regarding the luminosity distance, standard Λ-CDM cosmology is employed, with a Hubble constant $H_0 = 67.4$ km s^{-1} Mpc^{-1}, matter density parameter $\Omega_m = 0.321$ and a dark energy density parameter $\Omega_\Lambda = 0.679$ (Planck Collaboration et al., 2018). Note however that in practice the fits are not sensitive to minor differences in cosmological models due to the still relatively large uncertainties present in the estimated parameters.

For each GRB of the sample, the detectors with a source separation angle $< 60°$ are selected so to maximize the signal-to-noise ratio. Among those, the brightest NaI detector (i.e. highest significance) is used to generate the binning of the lightcurve through the Bayes blocks algorithm (Scargle et al., 2013). Only time bins with significance $> 5\sigma$ are employed in the fit, where the significance is estimated as a Poisson signal (the source counts) in presence of a gaussian background, as described in Li and Ma (1983); Vianello (2018).

Each of the spectra is fitted independently, as the model provides no dynamical prediction. For each of the fit parameters, uninformative priors are chosen (all units are in cgs):

$$\begin{aligned}
\Pi(\epsilon_e) &= \mathrm{Unif}(0.1, 0.9)\\
\Pi(\epsilon_B) &= \mathrm{LogUnif}(10^{-6}, 10^{-1})\\
\Pi(r_d) &= \mathrm{LogUnif}(10^{12}, 10^{16})\\
\Pi(\Gamma) &= \mathrm{Unif}(50, 1000)\\
\Pi(L_{GRB}) &= \mathrm{LogUnif}(10^{50}, 10^{55})
\end{aligned} \tag{5.1}$$

Aside from these priors, responsible for the physical parameters of the model, another set of priors is used as effective area corrections (Bissaldi et al., 2009) for the detectors, which are factors multiplying the nominal value of the effective area for each of the detectors, meant to represent the calibration uncertainties in the azimuthal dependence of the effective area. The priors for these parameters take the form of a truncated normal distribution centered on the nominal value (i.e. $c_k = 1$) of the effective area:

Table 5.2: The GRB sample used for the fits. Bursts with LLE data are marked with an asterisk.

GRB	T_{90}(s)	Redshift	Total spectra	Accepted fits
GRB 081118	20.7	2.58	4	4
GRB 081221	29.7	2.26	18	10
GRB 081222	18.9	2.77	6	4
GRB 090926B	64.0	1.24	5	5
GRB 091020	24.3	1.71	6	4
GRB 100704A	171.5	3.6	4	1
GRB 100728B	10.2	2.11	3	3
GRB 100816A	2.1	0.8	3	3
GRB 110213A	34.3	1.46	9	7
GRB 120119A	55.3	1.73	15	13
GRB 120326A	11.8	1.80	6	3
GRB 120729A	25.5	0.8	3	3
GRB 120811C	14.3	2.67	3	1
GRB 130518A*	48.6	2.49	25	0
GRB 131011A	77.1	1.87	4	3
GRB 140606B	22.8	0.38	5	0
GRB 140808A	4.5	3.29	4	3
GRB 141028A*	31.5	2.33	12	2
GRB 160509A*	369.7	1.17	27	0
Total			162	68

$$\Pi(c_k) = \text{TruncNormal}(\mu = 1, \sigma = 0.1, a = 0.5, b = 1.5) \tag{5.2}$$

where a and b are the lower and upper bound. The fit itself is performed trough the use of MULTINEST (Feroz et al., 2009), which reconstructs the posterior distribution of model's parameters through a sampling procedure. The "best fit" parameters are chosen as the ones which maximize the posterior, i.e. the ones defining the mode. The goodness of fit is assessed through the criteria introduced in Sec. 3.3.1, that is by making use of posterior predictive checks (PPCs), which test the ability of the fitted model to reproduce the observed data. An example of such plots is given in Fig. 5.3, where two PPC plots are shown: one for a successful and one for an unsuccessful fit.

5.4 Fit results

Each of the accepted spectral fits produces a complete set of parameters for the corresponding time bin of the GRB, as shown in Fig. 5.4. In the plots, two examples are provided: one for a well fitted GRB and another for a poorly fitted one. The shaded area around each spectrum denotes the 68% credible region, which tracks how "uncertain" the model prediction is. Note that the spectra are plotted up to 100 MeV, but GBM can only observe up to $\sim$ 40 MeV. As such, beyond this energy the spectrum is not directly observable (unless LLE data is available), but is instead a prediction of the model. For the complete sets of spectra and lightcurves of the GRB sample, refer to Appendix B, which also provides a Band function equivalent for each of the successful fits.

Note however that there are no dynamical predictions in the model, that is each time bin is fitted independently from one another. In general, the model produces low acceptance rates, with only a few GRBs being overall well fitted, see Tab. 5.2. In total, only $\sim$ 40% (68/162) of the spectra passed the PPCs. Interestingly, a fraction of them ($\sim$ 25% of the accepted spectra) are in the optically thin regime, which loosely corresponds to $\tau \gtrsim 1$, see Fig. 5.5. As visible from the plots, most of the values lie in the

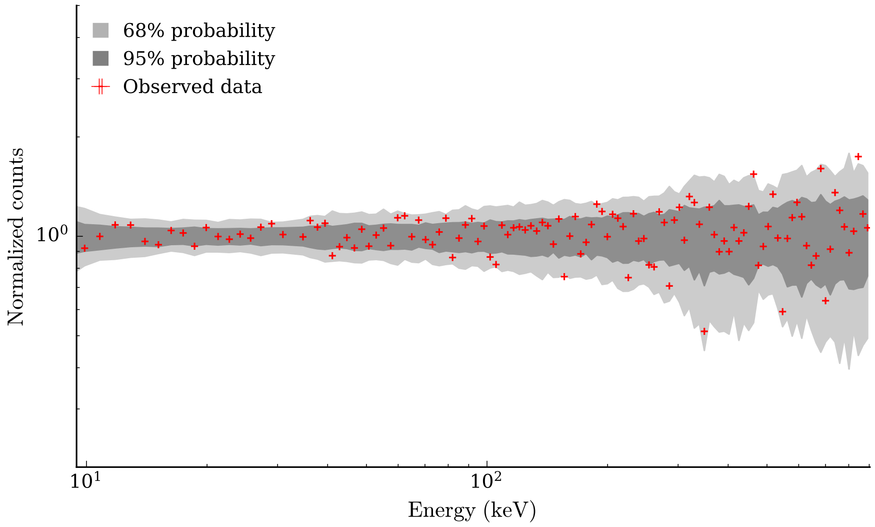

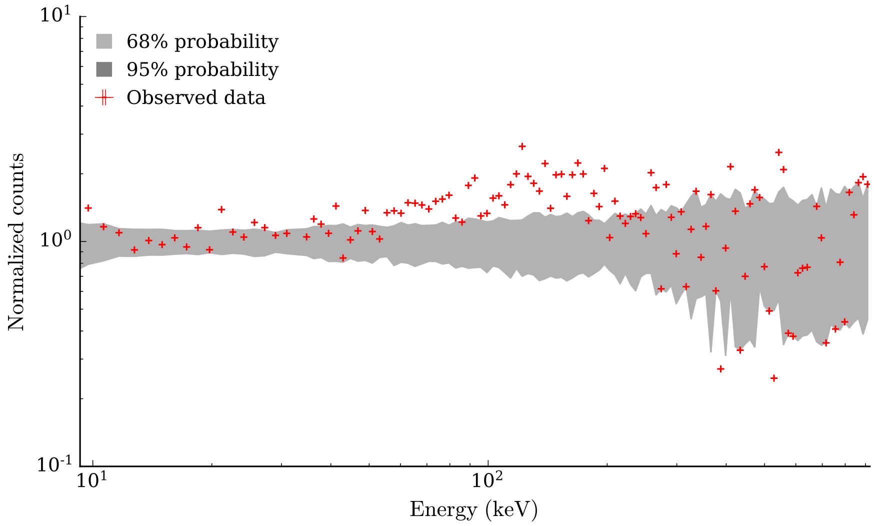

Figure 5.3: PPC plot examples for two different spectra: a successful (top, from bin 3 of GRB 090926B) and unsuccessful fit (bottom, from bin 9 of GRB 081221). Note how, in the second case, the model is unable to consistently capture the real data within its 95% probability region (light gray). Compared to Fig. 3.2, here the counts per bin have been normalized for easier visualization.

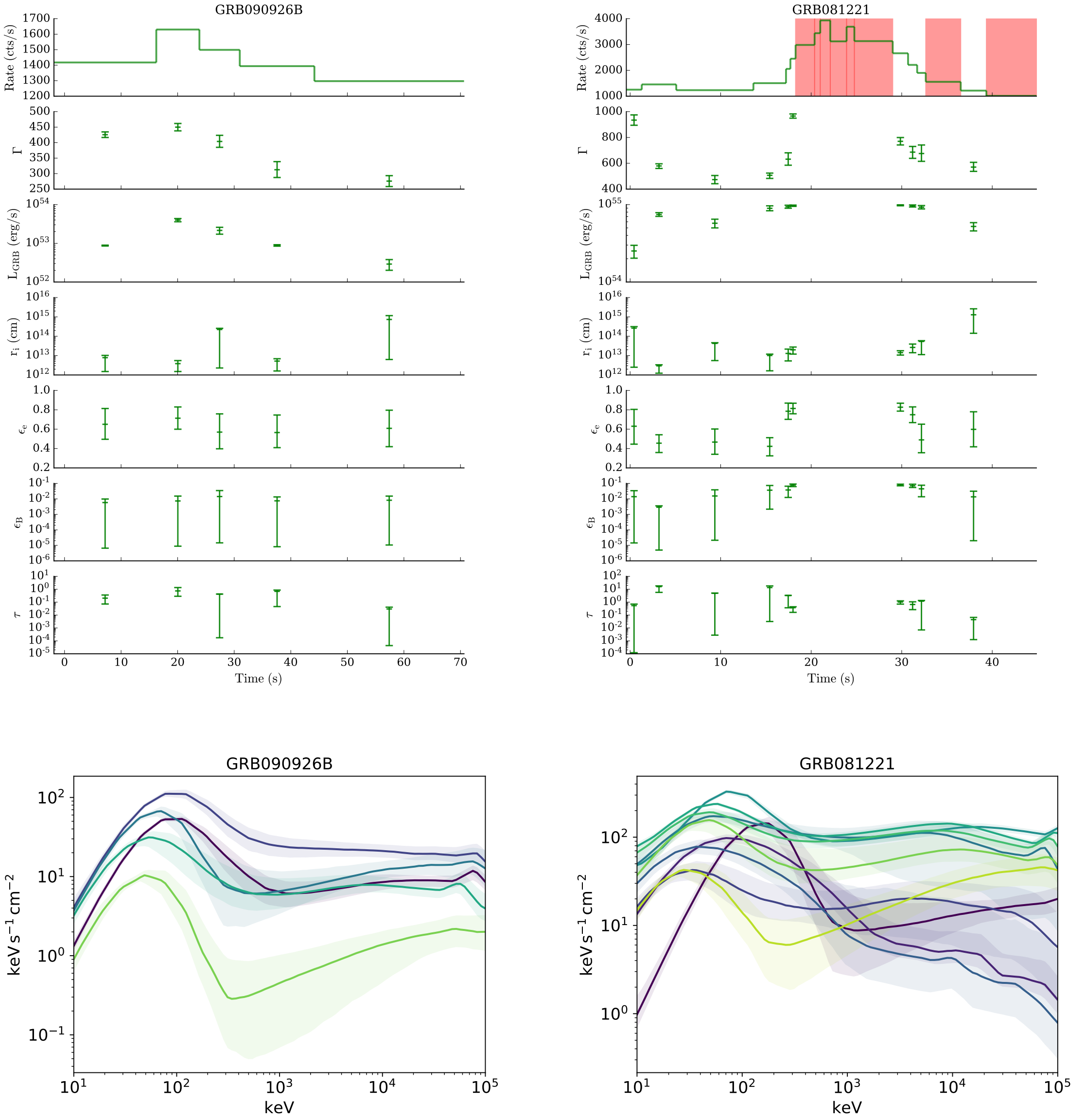

Figure 5.4: Example results of the model fits. On top are two examples of the GRB spectral fits performed with the model: a fully successful one (left) and a mostly unsuccessful one (right). Fits not passing the PPCs are rejected and their time bins are marked in red. On the bottom are instead the corresponding accepted spectra, with colors ranging from dark purple to yellow (corresponding to a viridis color map) denoting earlier to later time bins.

range $1 \lesssim \tau \lesssim 30$, which implies that the dissipation takes place close beneath the photosphere in most cases. Larger optical depths are disfavored, as they produce spectra which get progressively closer to a pure blackbody distribution, which is already known to be unable to describe the strongly non-thermal features of GRBs.

In many of these GRBs, the model seems to struggle particularly during the main phase of the lightcurve (i.e. the central part of the peak, see Appendix B), where the emission is stronger and the significance of the signal in the detectors is higher. This can be taken to imply that the photospheric model is either not managing to produce a sufficiently large flux (i.e. insufficient dissipated luminosity) or that it cannot reproduce the correct spectral shape. This is also shown in Fig. 5.6, which displays how the fit acceptance rate changes with increasing significance: as can be clearly seen, with larger values the model fits

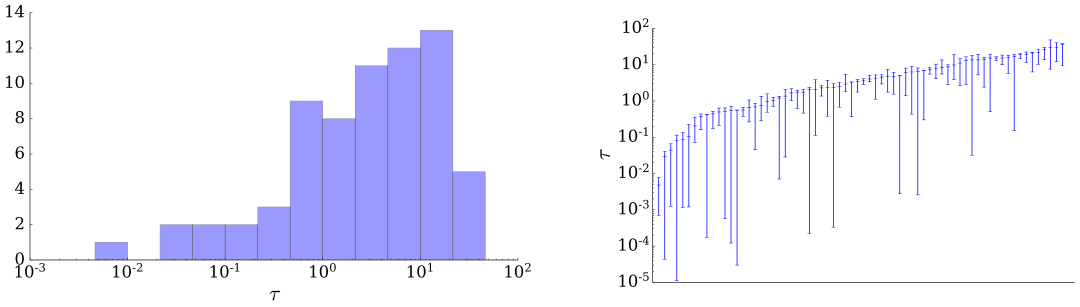

Figure 5.5: On the left, the distribution of the optical depth for the accepted fits. On the right, a barplot of τ, showing the values (with corresponding uncertainties) in ascending order.

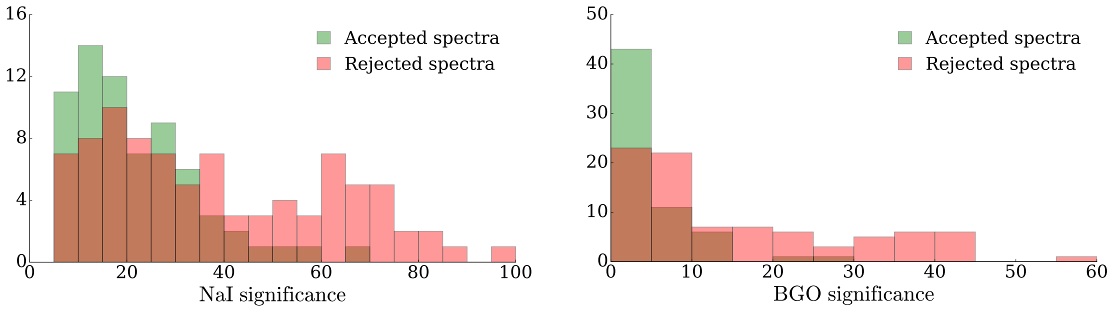

Figure 5.6: Histograms displaying the significance of the brightest NaI (left) and BGO detector (right) for the accepted and rejected fits. Note how the higher the signal-to-noise ratio, the lower the acceptance rate is.

almost always fail. This can be caused by either (or both) of the following:

1. The model is unable to capture the correct spectral shape whenever the detectors can better constrain it due to the higher counts' significance.
2. The model is unable to reach a dissipated luminosity ($\propto \epsilon_d L_{GRB}$) large enough to reproduce the flux (or more accurately the counts) measured by the detectors.

Looking at Fig. 5.7, it is possible to see that the luminosity distribution is pushed to the upper boundary for more than half of the accepted spectra. This suggests that the model, is most likely struggling to produce a large enough flux to match the detector counts, that is there is not enough dissipated energy. Larger values for the dissipation efficiency could in principle ameliorate the luminosity issue, as the dissipated energy scales roughly like $\propto \epsilon_d L_{GRB}$. Much larger efficiencies, while not impossible, are however far less likely. Moreover, even in the best case scenario could only increase the overall dissipated energy by another order of magnitude, as discussed more in detail in Sec. 5.5.

Since the model makes constraining predictions regarding the spectral shape at all energies, even outside the GBM energy window, it is possible to compute the bolometric observed luminosity for the accepted fits and check how it is distributed, as in Fig. 5.8. As visible, L_{obs} increases roughly linearly with the luminosity of the fireball L_{GRB} until reaching the maximum value $L_{obs}^{max} \sim \epsilon_d L_{GRB}^{max} \sim 10^{54}$ erg/s.
It is also of interest to investigate what happens when the luminosity of the fireball L_{GRB} is pushed close to its maximum value, as it may significantly affect the other estimated parameters in a non-trivial way. Fig. 5.9 does so by splitting the sample in two groups, that is spectra with $L_{GRB} > L_{thr}$ and $L_{GRB} < L_{thr}$, where $L_{thr} = 3.16 \cdot 10^{54}$ erg/s is the lower

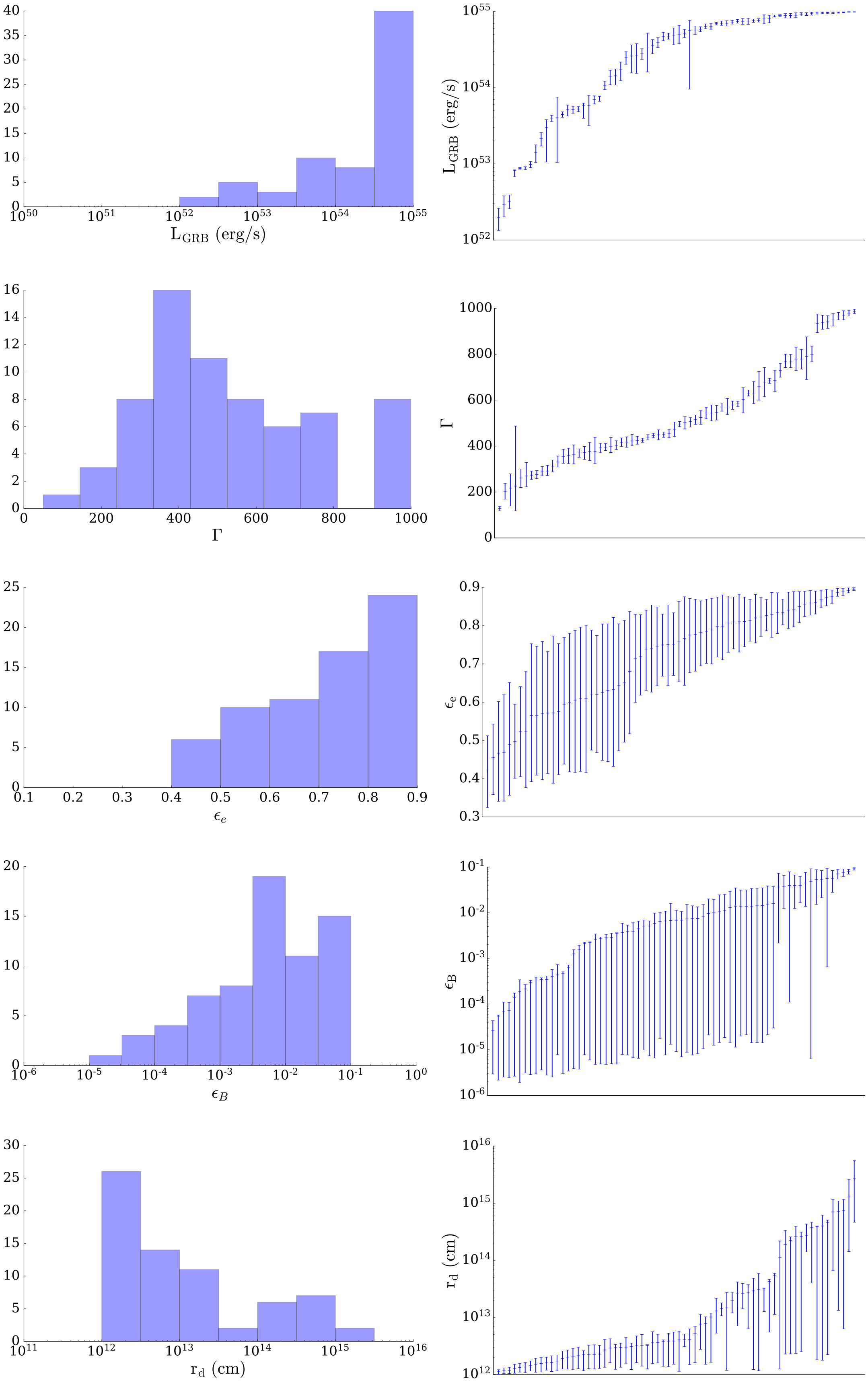

Figure 5.7: Parameter distributions for the successful fits. On the left column are the histograms for the fitted values, while on the right column the corresponding barplots are visible, showing each of the parameters' value (with corresponding uncertainties) in ascending order.

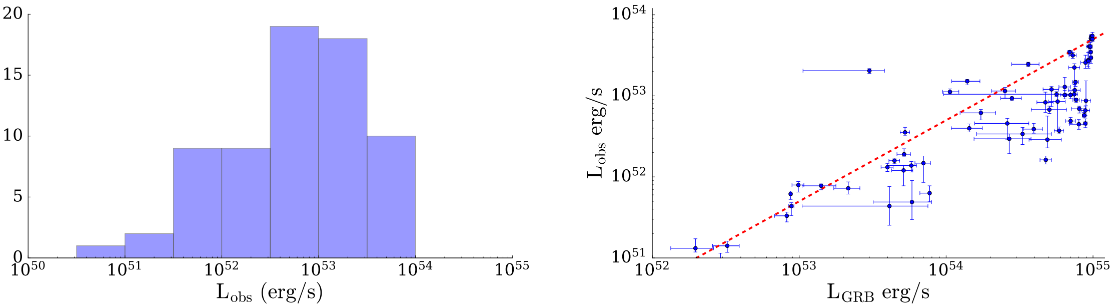

Figure 5.8: On the left, the distribution of the redshift corrected observed bolometric luminosity for the accepted spectra. On the right, the dependence of L_{obs} in relation to the luminosity of the fireball L_{GRB}, scaling roughly linearly (red line), $L_{obs} \sim \epsilon_d L_{GRB}$.

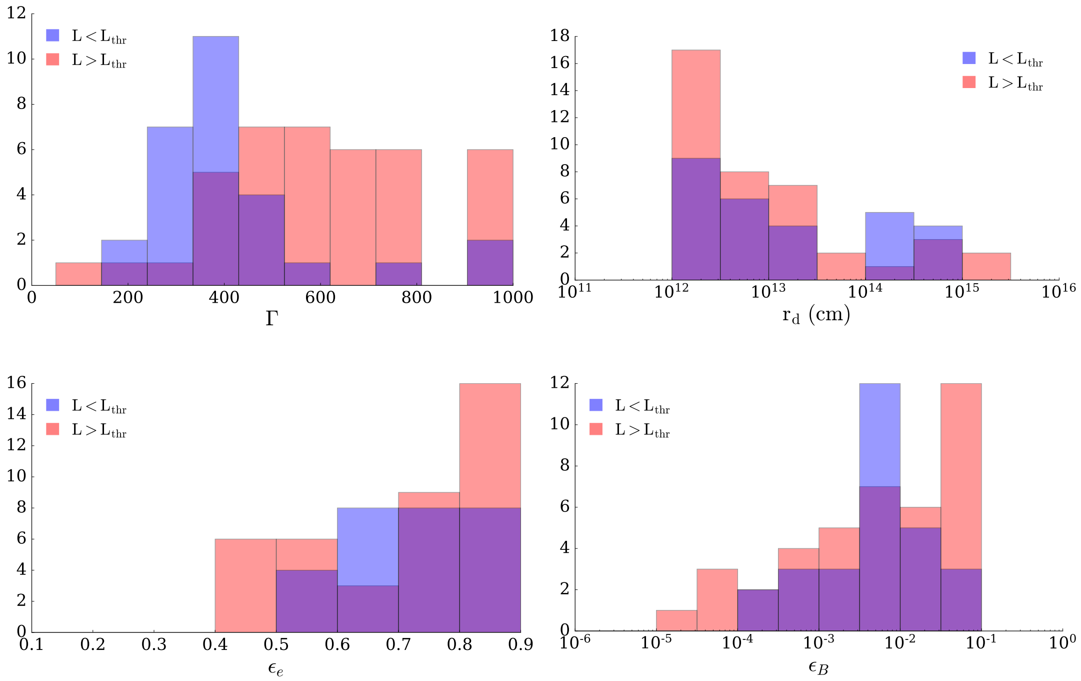

Figure 5.9: The distribution of the fitted parameters depending on the luminosity. The accepted spectra are split in two sub-samples: one having $L_{GRB} > L_{thr} = 3.16 \cdot 10^{54}$ erg/s (last luminosity bin in Fig. 5.7) and the rest with $L_{GRB} < L_{thr}$.

edge of the last bin of the histogram in Fig. 5.7. The most striking change is observed in the Lorentz factor distribution, which loses almost all of the values present in the tail of the distribution $\Gamma \gtrsim 500$ for $L_{GRB} < L_{thr}$. As discussed in the following, this tail is most likely an effect introduced by the insufficient fluxes generated by the model.

The distribution of the Lorentz factors seems on the other hand for the most part well behaved, peaking roughly at $\Gamma \sim 400$, but with a tail extending up to very large values. Note that larger Γ values also indirectly contribute to larger observed fluxes. As seen in Sec. 1.3.4, the luminosity of a pure thermal (i.e. non-dissipative) component scales like $L_{th} \propto \Gamma^{\frac{8}{3}}$. While the model here described is of course a dissipative photosphere, the "strength" of this original component will still end up affecting the overall luminosity of the final spectrum to some extent, at least in the case of sub-photospheric dissipation. This is due to the fact that the original thermal component is still providing photons, which can then undergo different physical processes (e.g. Compton scatter) to generate

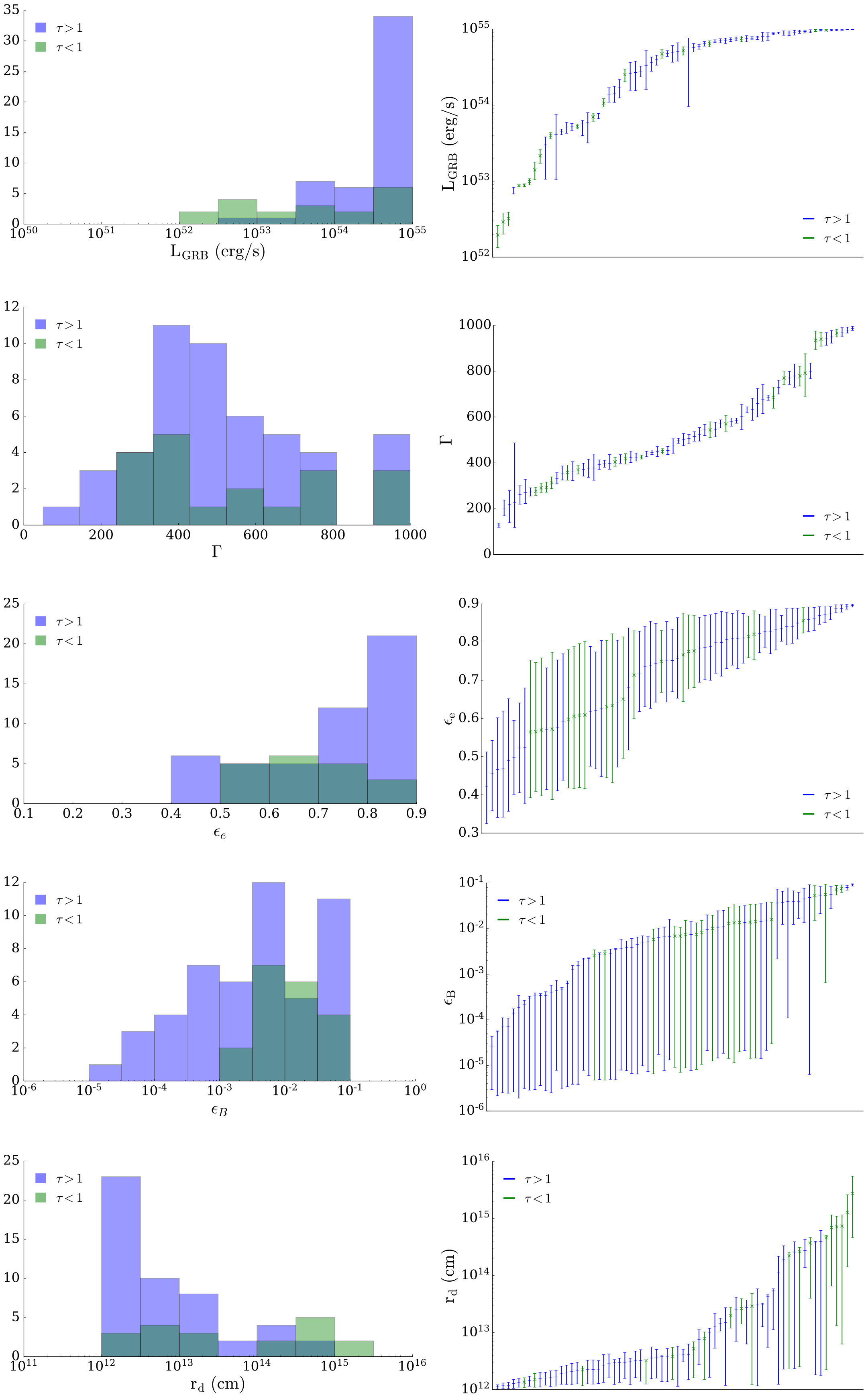

Figure 5.10: Same as Fig. 5.7, but here the parameters are separated in the optically thin $\tau < 1$ (green) and sub-photospheric $\tau > 1$ (blue) dissipation regimes.

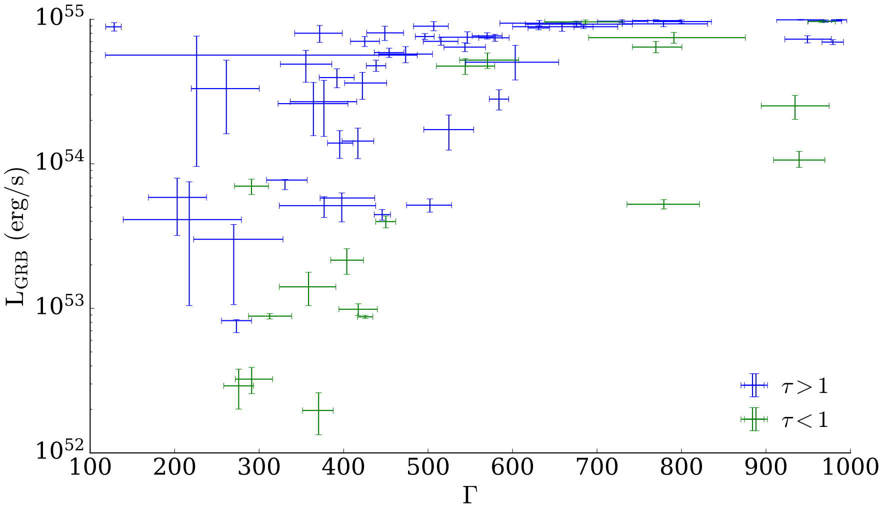

Figure 5.11: $\Gamma - L_{GRB}$ scatterplot. The blue points denote sub-photospheric dissipation ($\tau > 1$), while the green points indicate an optically thin regime ($\tau < 1$).

the final spectrum. This can be further verified in Fig. 5.11, which displays a $\Gamma - L_{GRB}$ scatterplot. In the figure, it is possible to see that an increase in Lorentz factor is (loosely) tied to an increase in luminosity. This trend continues until the maximum L_{GRB} is reached, after which a further increase is not possible anymore and the L_{GRB} values end up being tightly packed close to their boundary. This reasoning regarding the thermal component applies of course only to the cases where the dissipation is sub-photospheric (blue points in Fig. 5.11). As the transition to the optically thin regime takes place, synchrotron and SSC become more and more dominant in the emission.

The distribution for ϵ_e and ϵ_B from Fig. 5.7 are a bit less straightforward to interpret, as it seems that larger values are preferred, but not quite as strongly as in the case of the luminosity. The values of ϵ_B in particular are very poorly constrained below $\lesssim 10^{-2}$, due to the magnetic field being too weak to have an appreciable effect on the fitted spectrum. From a practical purpose, they act essentially as upper limits. The situation changes instead for $\epsilon_B \gtrsim 10^{-2}$, where the magnetic field becomes stronger and starts affecting the spectrum in a more appreciable way. As this corresponds to a stronger synchrotron and SSC component, this effect becomes particularly noticeable in the optically thin regime, as also visible in 5.10, which shows that most of the $\epsilon_B \gtrsim 10^{-2}$ have an optical depth $\tau \lesssim 1$. In general, it seems that the the magnetic field component is not always negligible and should be taken into consideration, differently from what done previously in other studies (Ahlgren et al., 2019a,b).

Finally, the distribution of the dissipation radius r_d exhibits an interesting multimodal behavior, see Fig. 5.7. The histogram displays two distinct peaks, one at $r_d \sim 10^{12}$ cm and a smaller bump at $r_d \sim 10^{14} - 10^{15}$ cm. These two peaks can be identified to roughly correspond to respectively sub-photospheric and optically thin regimes, though this distinction is somewhat fuzzy. This can also be seen in Fig. 5.10, where most (but not all) of the peak with large r_d belongs to the optically thin regime. It is also interesting to note that a few of the spectra in the sub-photospheric regime have large dissipation radii $r_d \gtrsim 10^{14}$ cm, which would imply even larger photospheres, normally thought to be very unlikely due to requiring very large matter densities. These radii are however for the most part very poorly constrained (see Fig. 5.12), as such this may not be a significant issue.

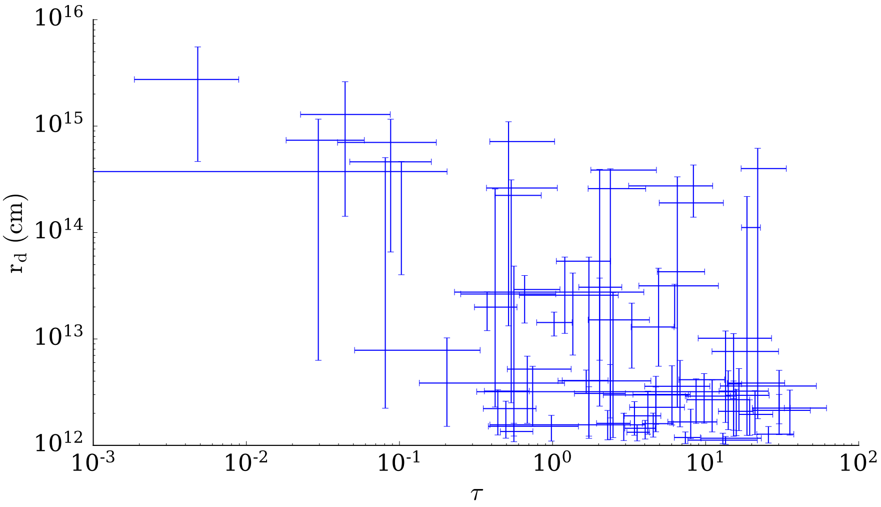

Figure 5.12: $\tau - r_d$ scatterplot.

Additionally, it is also possible to check how the photospheric radius is overall distributed in the sample of the accepted spectra. This is done by summing together the samples of each single spectral fit, so to provide a "global" distribution of the photospheric radius, as shown in Fig. 5.13. The result is a distribution peaking at $r_{ph} \sim 10^{13}$ cm and then decaying sharply for $r_{ph} \gtrsim 10^{14}$ cm. Larger values of r_{ph} are in principle possible, but very unlikely as they require high matter densities at large radii.

5.5 Discussion

Before discussing the results, it is of interest to further analyze the fits in terms of their distribution in the parameter space, as this allows to identify in which emission regimes the reconstructed spectra are. The following analysis adopts the same classification scheme as the one defined in Mészáros and Rees (2000), which laid the framework of the model here tested, developed by Pe'er and Waxman (2005). Adopting thus the same formalism, the dimensionless entropy is defined as $\eta = L_{GRB}/\dot{M}c^2$, with $\dot{M}$ mass ejection rate. This parameter sets the maximum achievable value for the Lorentz factor, assuming that the acceleration of the outflow can be completed, which is always the case as long as the saturation radius r_s is smaller than the photospheric radius r_{ph}. The condition $r_s \leq r_{ph}$ corresponds to $\eta \leq \eta_*$, with η_* typically being a very large Lorentz factor, achievable only if the baryon load of the fireball is very low. For all of the fits here considered, $\eta_* > \Gamma_{max} = 1000$, thus this region of the parameter space is not relevant for the analysis here performed.

The comoving compactness parameter, defined as $\ell = n_\gamma \sigma_T (r/\Gamma)$ (with n_γ comoving photon density), can be used to assess whether pair creation $\gamma\gamma \rightarrow e^+e^-$ is significantly affecting the photon spectrum (Mészáros and Rees, 2000). The presence of pairs is of particular importance, as they contribute to increase the overall Thomson scattering optical depth. For $\ell \gtrsim 1$, comptonization (that is Compton scatter of the photons to higher energies) becomes important, while for $\ell \lesssim 1$ simple synchrotron dominates the emission (note that the radius at which $\ell = 1$ is always beyond the photosphere). Fig. 5.14 shows an example (see Appendix C for the complete list of phase space plots for the successful fits) of how the parameter space can be represented in terms of η and r/r_0, with the result of a single fit being identified by the blue point with $\eta = \Gamma$ and $r/r_0 = r_d/r_0$. Starting from the bottom, it is possible to see the green line defining the saturation radius r_s. All points above this

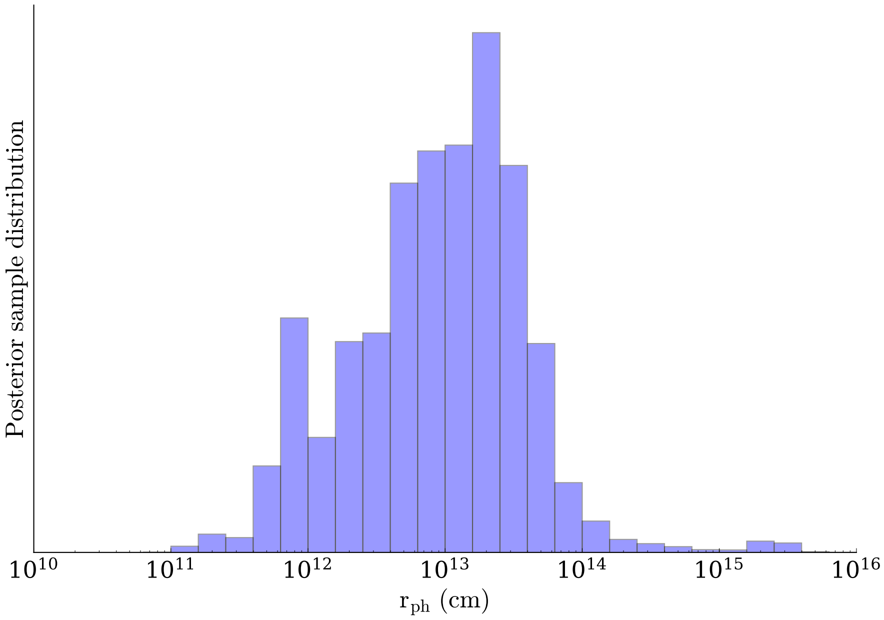

Figure 5.13: Global distribution for the photospheric radius, obtained by summing together the samples of the r_{ph} distributions for each spectral fit.

line correspond to completely accelerated ejecta, reaching the coasting Lorentz factor, while anything below is not (note that this is never the case for any of the results here discussed). The red line identifies instead the photosphere r_{ph}, which decreases as $r_{ph} \propto \eta^{-3}$ until reaching the critical value η_*, where $r_{ph} = r_s$. Past this point, the photosphere occurs in the accelerating region and behaves instead like $r_{ph} \propto \eta^{-\frac{1}{3}}$ (Mészáros and Rees, 2000). This region is never reached by any of the fits, as it requires very large Lorentz factors $\eta \gtrsim 1000$ for luminosities $L_{GRB} \gtrsim 10^{52}$ erg/s. In the figure, the dashed line indicates the minimum dissipation radius allowed by the internal shock scenario, $r_{sh}^{min} = 2r_0\eta^2$. This is computed assuming a minimum variability timescale set by the size of the inner engine, $t_{var} = r_0/c$. Anything below this line is not consistent with simple internal shock and requires some different or additional kind of dissipation mechanism. Note that $r_{sh}^{min} \propto \eta^2$ only up to η_*, as past this value the shells are not being fully accelerated anymore, as the saturation radius occurs beyond the photosphere. Finally, the optically thin region $r > r_{ph}$ (i.e. $\tau < 1$) is divided in two zones depending on the compactness value. The magenta line denotes the radius at which $\ell = 1$, that is past this boundary the comptonization of the photons becomes negligible (and pure synchrotron should dominate the emission), while points falling in the $\ell > 1$ region should still exhibit a synchrotron plus inverse Compton spectrum.

Fig. 5.14 displays the behavior for a single spectrum, however it is more of interest to see how the results of the sample of accepted fits are overall distributed. This check is however not completely trivial to perform, as the different regions shift with different source (i.e. parameter) configurations. In particular, different values of L_{GRB} will move the r_{ph} and $\ell = 1$ lines vertically, while the η_* line moves horizontally. Thus each fit result has its own version of the phase space diagram. Moreover, the boundary lines themselves are actually "fuzzy", as they depend on the estimated fit parameters, which are actually described by distributions and not single values (for the sake of clarity, Fig. 5.14 only plots the line corresponding to the parameter configuration of the mode of the posterior). This implies that it is not trivial to understand were exactly a fit result lies in the parameter

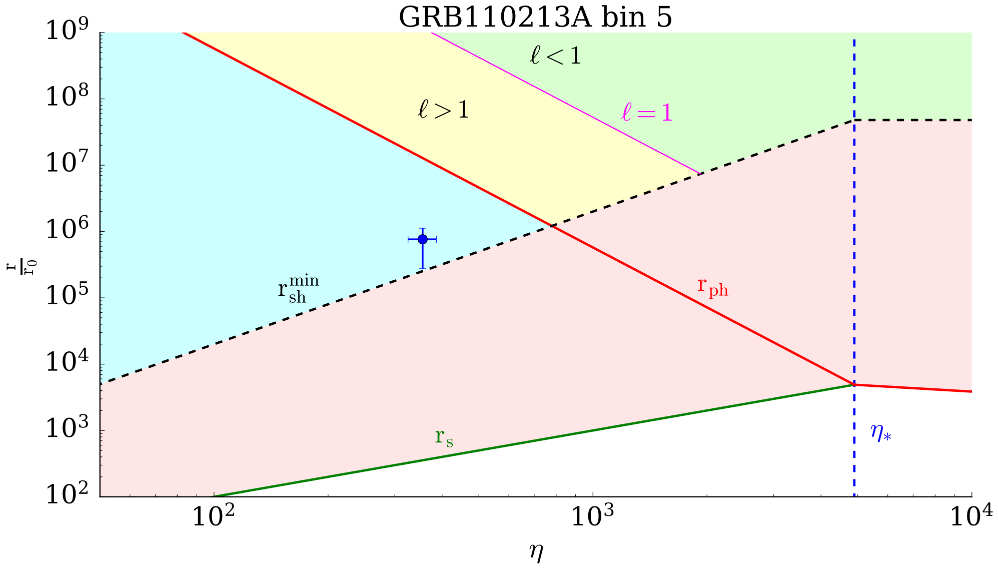

Figure 5.14: Results of a single fit in the $\eta - r/r_0$ phase diagram. The various lines mark the transition points between different regimes and have the following meanings: saturation radius (green), photospheric radius (red), compactness $\ell = 1$ (magenta) and minimum dissipation radius allowed by internal shocks (black dashed line). The shaded regions thus denote the different regimes: dissipation incompatible with internal shocks (red), sub-photospheric dissipation (cyan), optically-thin dissipation with high compactness (yellow) and optically-thin dissipation with low compactness (green). The blue dashed line denotes the value η_* for which $r_s = r_{ph}$, which is also the value of η for which r_{sh}^{min} stops increasing. η_* is too large to be reached by any of the accepted fits. Finally, the white region below r_s corresponds to very small radii (never reached in the fits) for which the ejecta are not completely accelerated.

space, as the distinction between different regions is not sharp. To solve this issue, while also taking fully into account the uncertainties, the following method was thus employed. As each fit produces a posterior distribution through sampling (see Sec. 3.3), each of these sampled points corresponds to a specific source configuration, with its own version of the phase space diagram. In this case it is however unaffected by uncertainties, as a single point is simply a draw from the posterior distribution, a single realization out of the many possible ones. It is possible to see how the results of a fit are distributed by simply checking where each sampling point lies (i.e. in which of the shaded regions of Fig. 5.14), thus obtaining at the end a probability quantifying how likely it is for the source to be in certain region or the other of the parameter space. This process can be repeated for all of the posterior distributions of the accepted fits, allowing to assess how the sample is overall distributed with respect to the different emission regimes. This is shown in Fig. 5.15, which quantifies how likely each region is for the sample of the accepted fits. Most notably, it is possible to see that almost half of the probability lies in the region below the minimum limit set by simple internal shocks. As such, other/additional dissipation mechanisms may be at work, e.g. magnetic reconnection. Moreover, while $\sim 75\%$ of the probability is in the sub-photospheric regime, the remaining fraction lies in the optically thin region. Most of these are in the high compactness $\ell > 1$ region, thus indicating that inverse Compton plays an important part in the generation of the observed spectra even above the photosphere. Finally, the remaining small fraction of the probability lies the synchrotron dominated region $\ell < 1$, meaning that the model still favors simple synchrotron emission in some cases.

This chapter performed a test of the dissipative photosphere model developed by Pe'er and Waxman (2005), analyzing the viability of the emission mechanisms described in Sec. 1.3.4. The fits were performed on a sample of 19 time-resolved GRBs, correspond-

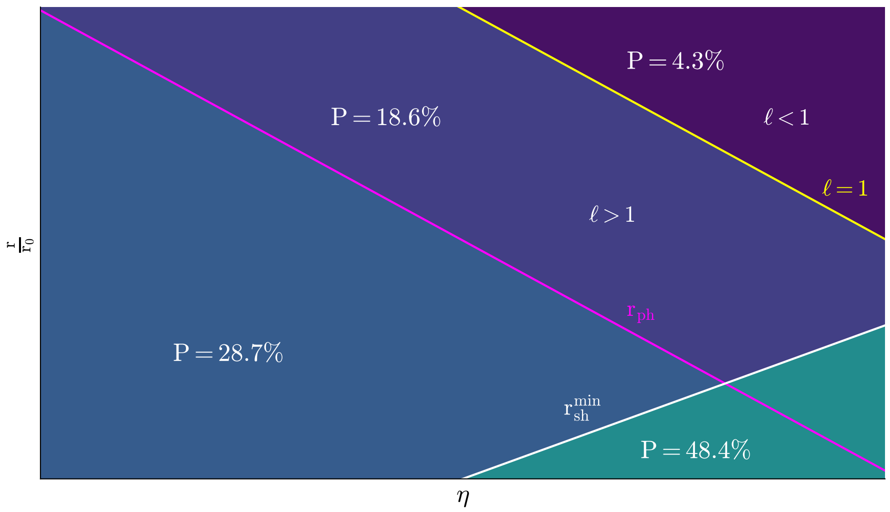

Figure 5.15: Distribution of the fit results in the $\eta - r/r_0$ phase space diagram. The various percentages denote how many of the total sampling points are captured by each of the different regions. The size of the zones is not in scale to the actual parameter space they correspond to.

ing to a total of 162 spectra. It was found that the model is overall unable to describe the observations due to several issues discussed in the following.
First of all, the most problematic aspect of the model is the luminosity. Its distribution for the accepted spectra peaks sharply at the maximum value allowed by the parameter space, that is $L_{GRB} = 10^{55}$ erg/s, which is hard (though strictly speaking not impossible) to justify on a physical basis, as this would imply emitting the equivalent of $\sim 5M_\odot$ in a timescale of one second. Naively, one could think that the luminosity issue can be solved by simply adopting larger dissipation efficiencies, but this approach effectiveness is also affected by severe limitations. The efficiency value here adopted is fixed to $\epsilon_d = 5\%$, which can be considered a typical value for e.g. the internal shock scenario (Piran, 2004; Pe'er, 2015). While larger values are possible, they are unlikely, as they require some degree of fine-tuning of the shell conditions (see Sec. 1.3.5). Much larger efficiencies, possibly up to $\epsilon_d \sim 50\%$ (Giannios and Spruit, 2006), could be reached by assuming that the dissipation occurs through magnetic reconnection. Even in that case however, the dissipated energy can only increase by another order of magnitude, hardly enough to solve the current luminosity issue, with most of the current accepted spectra exceeding $L_{GRB} \gtrsim 10^{54}$ erg/s, values hard to motivate on a physical ground, as a luminosity of $\sim 10^{55}$ erg/s corresponds to emitting $\sim 5M_\odot$ of energy in a timescale of one second. While larger ϵ_d values would be able to recover a fraction of these extreme luminosities, more would fill those bins, as the spectra which were rejected due to the model not generating a sufficient flux would now able to, but only by combining large values of L_{GRB} and ϵ_d, which are hard to justify consistent basis.

As mentioned before, there exist previous studies performed with the same model, see Ahlgren et al. (2015, 2019a,b). A comparison to the results obtained in these previous works is here provided. Since Ahlgren et al. (2015) includes only two GRBs and employs a very small grid, the focus will be on the later studies, namely Ahlgren et al. (2019a,b). Both of these studies test a specific scenario, that is sub-photospheric dissipation through internal shocks at a fixed optical depth of $\tau = 35$. Furthermore, the following parameters are fixed: $\epsilon_e = 0.9$, $\epsilon_B = 10^{-6}$ (i.e. negligible magnetic fields), $r_d = r_{ph}/\tau$ (dissipation at fixed optical depth) and $r_d = r_0\Gamma^2$ (minimum dissipation radius under internal shock assumption). The parameters being fitted are instead Γ, L_{GRB} and ϵ_d. Ahlgren et al. (2019b) employs GBM and LLE data (when available) on a sample of 36 time-resolved GRBs (for a total of 634 spectra), while Ahlgren et al. (2019a) uses GBM and *Swift*/XRT on a sample of 8 GRBs (for a total of 32 spectra). In the following are summarized the main differences between these previous works and the analysis performed here.

In Ahlgren et al. (2019b) the grid used for the fitting is defined by the following parameter values:

- $\Gamma = [100,\ 150,\ 200,\ 250,\ 300,\ 350,\ 400,\ 450,\ 500]$
- $L_{GRB} = [0.1,\ 0.5,\ 1, 5,\ 10,\ 50,\ 100,\ 200,\ 300] \cdot 10^{52}$ erg/s
- $\epsilon_d = [0.01,\ 0.025,\ 0.05,\ 0.075,\ 0.1,\ 0.15,\ 0.2,\ 0.25,\ 0.3,\ 0.35,\ 0.4]$

which corresponds to a total of 891 template spectra. Note that the assumption of $\tau = 35$ is to some extent constraining the spectral shapes the model can take, as spectra generated at this optical depth tend to display a single, well defined peak, mainly generated by the comptonization of the thermal photons. The parameter distributions resulting from the fits are displayed in Fig. 5.16. Of the analyzed 634 spectra, only 171 ($\sim$ 27%) were found to be well described by the model. Similarly to what found in this thesis, the main reason for the low success of the fits is deemed to be the inability to generate sufficiently large fluxes. The luminosity issue is also evident from Fig. 5.16, where, even by allowing efficiencies up to 40%, the luminosity distribution is still peaking at the upper boundary. Interestingly however, the vast majority of the fitted spectra result in a $\epsilon_d \lesssim 10\%$ value, which seems to further reinforce the validity of the assumption of $\epsilon_d = 5\%$ adopted in the analysis done in this thesis. The Lorentz factor distribution is instead different from what achieved here, as it peaks at its lower boundary $\Gamma \sim 100$. This behavior is less clear, but it could be caused by the simultaneous presence of constraint $\tau = 35$ and $r_d = r_0\Gamma^2$. The dissipation radius (though not a free parameter in Ahlgren et al. (2019b)), peaks sharply at $r_d \sim 10^{12}$ cm, similarly to what found in this thesis, though that constitutes the lower boundary of the parameter space in this case.

Ahlgren et al. (2019a) employs instead a larger table model for the fitting, that is:

- $\Gamma = [50,\ 100,\ 150,\ 200,\ 250,\ 300,\ 350,\ 400,\ 450,\ 500,\ 600,\ 700,\ 800,\ 900,\ 1000]$
- $L_{GRB} = [0.1,\ 0.5,\ 1, 5,\ 10,\ 50,\ 100,\ 200,\ 300,\ 1000] \cdot 10^{52}$ erg/s
- $\epsilon_d = [0.01,\ 0.025,\ 0.05,\ 0.075,\ 0.1,\ 0.15,\ 0.2,\ 0.25,\ 0.3,\ 0.35,\ 0.4]$

for a total of 1650 templates. The use of *Swift*/XRT data allows to extend the energy window of the observations down to 0.3 keV, which can help further constrain the spectral shape. The acceptance rate is 50% (16/32 spectra), thus almost double what found in Ahlgren et al. (2019b), most likely due to the lower luminosity of the GRBs, $L_{GRB} \sim 10^{51} - 10^{52}$ erg/s for the accepted spectra. It needs however to be pointed out that 11 of the 16 accepted spectra have very large dissipation efficiency values $\epsilon_d \gtrsim 20\%$, which is hard to justify on a consistent basis in an internal shock scenario, such as the one being considered. The still modest success rate is likely the product of the assumption of a fixed optical depth for the dissipation, as this can limit the ability of the model of describing more complex spectral shapes. This is particularly important, given the extended energy range of the observations provided by the presence of *Swift*/XRT with GBM.

The performance of the model as assessed in this thesis is grossly consistent with what seen in the previous studies (Ahlgren et al., 2019a,b), with low acceptance rates and issues

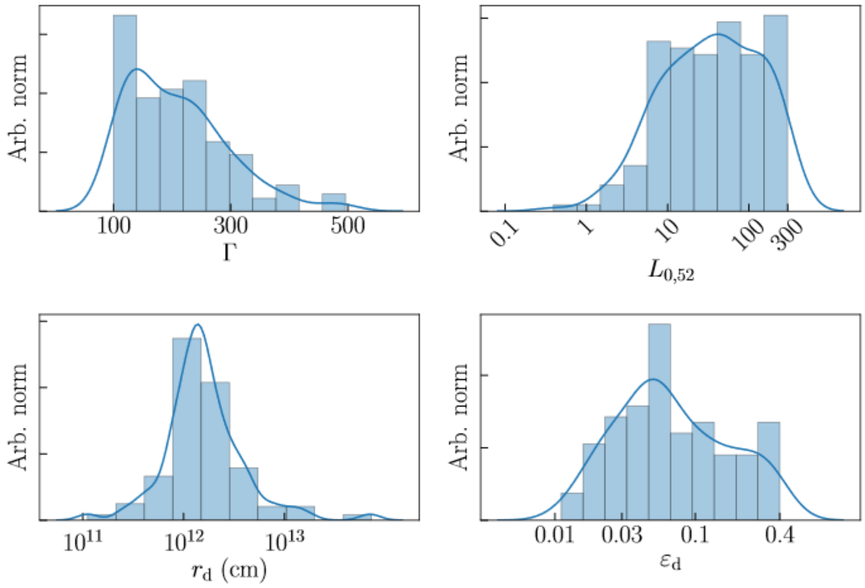

Figure 5.16: Distributions of the fitted parameters from Ahlgren et al. (2019b).

in producing large enough fluxes. In the case of the analysis performed here, the most constraining parameter is the dissipation efficiency. Theoretically, larger values are possible, perhaps up to $\epsilon_d \sim 50\%$ in a magnetic reconnection scenario (Giannios, 2006), though this dissipation mechanism is still subject to many theoretical uncertainties. However, even in the best case scenario of $\epsilon_d \sim 50\%$, it remains very unlikely that the luminosity problem of the model could be solved, as is also demonstrated by the results of Ahlgren et al. (2019b), which, even by allowing much larger efficiencies, still failed to consistently fit the analyzed GRBs spectra.

On the other hand, looking at the results of the synchrotron fits performed by Burgess et al. (2020) on the same sample of GRBs studied here, one finds far different results: it was demonstrated that simple optically thin synchrotron is able to successfully fit 95% (154/162) of the spectra. Furthermore, the results indicate that the emission is incompatible with the presence of a photospheric component, as the Lorentz factor required by it is smaller than the lower limit imposed by the transparency of the outflow to higher energy photons (see Sec. 1.3.1). These synchrotron fits are however not completely exempt from issues, as many of the fitted spectra are found to be in the slow cooling regime in a significant fraction of the cases. This is problematic, as this regime is intrinsically inefficient in radiating photons.

5.6 Conclusions

The study performed in this thesis provides for the first time a direct comparison between a dissipative photosphere model and the synchrotron emission on the same sample of GRBs. For this work, the photospheric model developed by Pe'er and Waxman (2005) was adopted and used to generate a large table model, covering an extensive parameter space. The achieved results show an overall poor performance of the model, with only $\sim 40\%$ of the fits being accepted. This is in all probability caused by the inability of the model to generate sufficiently large fluxes. While this can be partially attributed to the assumption of a low-moderate dissipation efficiency of $\epsilon_d = 5\%$, even much larger values (which could roughly increase the dissipated energy up to another order of magnitude) are unlikely to completely solve the issue. They would also be harder to justify from a physical standpoint, at least with conventional dissipation mechanisms such as internal shocks and magnetic reconnection, which typically have efficiencies of the order of $\epsilon_d \sim 10\%$ (Piran, 2004; Giannios, 2006).

Regardless of the performance of the model, it is still possible to make some interesting physical considerations out of the accepted spectra, where the dissipative photosphere emission is able to describe the data. First of all, it is interesting to note that a fraction of the fits ($\sim 25\%$) still favors the optically thin regime, where synchrotron emission is significant, over pure sub-photospheric dissipation (which was the only case considered by the previous studies performed by (Ahlgren et al., 2019a,b)). This could imply that hybrid models, allowing for both regimes, are a better description of the prompt emission. It is possible, if not likely, that the dissipation is not always occurring in either the optically thin or optically thick region, but that this varies from case to case. As shown by Fig. 5.15, this corresponds to different emission regimes, where different components become more or less important depending on the parameter space region the GRB lies in. Moreover, as seen in Sec. 5.5, it was also found that the accepted spectra are not entirely consistent with simple dissipation from internal shocks and may require different or more complex mechanisms, at least in a fraction of the cases.

This once again shows the potential of direct fits of physical models, which allow to perform proper physical inference on the data. Future studies may proceed down this path by testing different implementations of the dissipative photosphere (or optically thin synchrotron) models, which may allow to further constrain the underlying physics of the prompt emission.

Conclusions and outlook

The work performed in this thesis demonstrates that it is possible to better constrain gamma-ray bursts by approaching the problem in two different, yet connected, ways.
First, the GBM localization study here presented shows that, while achieving constraining GRB positions with GBM remains often challenging, large improvements can be achieved by means of a better source reconstruction method. The traditional localization method for GBM, i.e. the DoL algorithm, fits for the position by assuming that the spectrum follows either one of three spectral templates, which correspond to different responses for the detector. This implies that whenever real spectrum and template do not match, systematics are being introduced into the estimated position. To compensate for this inherent inaccuracy of the method, the DoL positions adopt much larger error regions through the addition of a systematic error component (Connaughton et al., 2015). As demonstrated in this thesis, by making use of the BALROG algorithm (Burgess et al., 2018), which allows for a simultaneous fit of both position and spectrum, these systematics arising from a wrong methodology can be removed. The improved locations so obtained are both more accurate (i.e. correct error regions) and more precise (i.e. smaller uncertainties).
Other follow-up studies performed by von Minckwitz (2020) also show that wrong positions do affect the results of spectral fits due to the wrong response being employed. These findings have important implications, as any study reliant on the standard GBM positions could be indirectly affected by systematics. As such, these issues should also be further investigated in the future. Finally, a natural next step to the work performed here is to use the BALROG locations for new multi-messenger searches (e.g. neutrinos), given that the improved accuracy of the positions will be able to provide more reliable results.

The following test of the photospheric emission model approaches instead the “GRB problem” from a different angle and tries to better model the spectrum of these sources. The physics underlying the prompt emission in GRBs is still uncertain, with two main competing models being present at the moment: emission from a dissipative photosphere and optically thin synchrotron. Due to the numerical complexity of these models, they have seldom been tested directly onto the data (Ahlgren et al., 2015, 2019a,b; Burgess et al., 2020) and most of the physical inference so far has been performed through the use of simple empirical functions (e.g. Band function).
This thesis instead tests directly the dissipative photosphere model developed by Pe’er and Waxman (2005) by generating a table model covering a large parameter space. The results of the fits show that the model is unable to consistently describe the data, achieving an acceptance rate of $\sim 40\%$, as in many instances it cannot generate a large enough flux to match the measured detector counts. Larger dissipation efficiencies may be able to ameliorate the issue, potentially increasing the dissipated energy by up to an order of magnitude, but this is unlikely to completely solve the problem.
The model however still constitutes a useful tool to probe the underlying physics of GRB prompt emission. From the accepted spectra, it was found that in a significant fraction

of cases ($\sim 25\%$) the dissipation occurs in the optically thin region, where synchrotron is expected to be an important part of the spectrum, suggesting thus that the emission does not occur exclusively in only one of the two regimes. It was also found that the fitted spectra are not entirely consistent with simple internal shocks. This likely implies that different or additional dissipation mechanisms are at work, which future studies may be able to further investigate.

Both of the analyses performed in this thesis laid the groundwork for future more advanced studies. The improved GBM locations can be used for better follow-up observations and more constraining multi-messenger searches, with the locations being openly available to the scientific community at https://grb.mpe.mpg.de. This is of particular importance, as the main limiting factor of the current observations is not their overall number, but their "completeness", i.e. only a relatively small fraction of the total sample have observations ranging from the prompt emission until the later stages of the afterglow. This severely limits what can be inferred from the available detections. Conversely, when many multi-wavelength (and possibly multi-messenger) observations are present for the same event, much more information can be obtained and thus used for physical inference, as demonstrated by events such as GRB 170817A (Abbott et al., 2016; Goldstein et al., 2017). As such, having a constraining and accurate gamma-ray position available is of utmost importance for follow-up observations and multi-messenger searches.

On the other hand, the fits of the photospheric model here performed test the emission mechanisms of GRB prompt emission. Identifying the correct physical processes would allow for a better understanding of the source, which could help in constraining the predicted neutrino fluxes. While the photospheric model here analyzed is unable to fully describe the observations, it was shown that from the sample of accepted spectra it is possible to perform physical inference regarding the emission regimes and the dissipation mechanisms at work in GRBs. Future studies may be able to test different and possibly more sophisticated implementations of the emission from a dissipative photosphere or optically thin synchrotron, further refining the analysis done here. New measurements could also be able to shed more light on the matter. Polarimetry in particular is an especially good candidate to discriminate between different emission models: for example, a single measurement of the polarization fraction $\Pi \gtrsim 50\%$ would strongly favor synchrotron over photospheric emission (Gill et al., 2020). With the upcoming polarimeter POLAR 2, such measurements may be soon be possible and thus provide the observations needed to achieve a better understanding of the emission mechanisms in GRBs.

Appendix A: location tables

Table 5.3: List with the analyzed GRBs. In the model column, the abbreviations have the following meanings: cpl = cut-off power-law, band = Band function and pl = power-law. Asterisks in front of the trigger numbers denote short GRBs.

	Swift		BALROG				DoL				Data	
Trigger	RA (°)	DEC (°)	RA (°)	DEC (°)	Offset (°)	Model	RA (°)	DEC (°)	Err. (°)	Offset (°)	Fluence ($\mathrm{erg} \cdot \mathrm{cm}^{-2}$)	Peak flux ($\mathrm{ph} \cdot \mathrm{cm}^{-2} \cdot \mathrm{s}^{-1}$)
080714745	188.1	-60.2	184.6 ± 5.0	−57.4 ± 2.1	3.3	cpl	183.5	-57.5	3.9	3.6	$6.3 \cdot 10^{-6}$	6.9
080723557	176.8	-60.2	178.6 ± 0.6	−61.2 ± 0.6	1.3	cpl	175.1	-60.7	1.0	1.0	$7.2 \cdot 10^{-5}$	$3.0 \cdot 10^{1}$
080725435	121.7	-14.0	120.7 ± 1.7	−12.8 ± 2.3	1.5	cpl	123.1	-23.1	2.2	9.2	$8.0 \cdot 10^{-6}$	3.4
080727964	32.6	64.1	41.6 ± 6.9	63.3 ± 2.9	4.1	cpl	40.0	62.2	2.7	3.8	$1.3 \cdot 10^{-5}$	3.5
080804972	328.7	-53.2	325.9 ± 3.7	−52.7 ± 1.3	1.8	cpl	320.8	-52.7	2.4	4.8	$9.1 \cdot 10^{-6}$	3.8
080916009	119.8	-56.6	121.3 ± 1.1	−57.2 ± 0.7	1.0	band	124.4	-54.7	1.4	3.2	$6.0 \cdot 10^{-5}$	$1.4 \cdot 10^{1}$
081102739	331.2	53.0	327.2 ± 5.0	50.2 ± 3.3	3.8	pl	321.3	51.9	4.5	6.1	$3.8 \cdot 10^{-6}$	2.7
081121858	89.3	-60.6	95.6 ± 7.7	−64.6 ± 1.7	5.0	cpl	97.2	-59.9	1.1	4.0	$1.5 \cdot 10^{-5}$	7.7
081126899	323.5	48.7	327.5 ± 1.2	48.2 ± 2.3	2.7	cpl	326.9	50.3	2.7	2.7	$1.1 \cdot 10^{-5}$	6.5
081221681	15.8	-24.5	13.4 ± 0.4	−22.9 ± 0.5	2.7	cpl	14.1	-25.2	1.2	1.7	$3.0 \cdot 10^{-5}$	$2.5 \cdot 10^{1}$
081222204	22.7	-34.1	20.5 ± 1.1	−32.5 ± 0.7	2.5	cpl	18.6	-32.4	1.5	3.8	$1.2 \cdot 10^{-5}$	$1.3 \cdot 10^{1}$
090102122	128.2	33.1	124.5 ± 1.0	31.0 ± 0.6	3.8	cpl	128.5	30.3	1.5	2.8	$2.8 \cdot 10^{-5}$	$1.1 \cdot 10^{1}$
090129880	269.1	-32.8	266.4 ± 6.6	−36.7 ± 1.9	4.5	cpl	270.6	-33.8	1.8	1.6	$5.6 \cdot 10^{-6}$	6.6
090323002	190.7	17.1	191.2 ± 2.1	16.0 ± 1.9	1.2	cpl	190.1	21.1	1.2	4.0	$1.1 \cdot 10^{-4}$	$1.3 \cdot 10^{1}$
090328401	90.9	-42.0	94.4 ± 1.6	−44.1 ± 0.6	3.3	band	95.9	-45.1	1.0	4.8	$4.2 \cdot 10^{-5}$	$1.7 \cdot 10^{1}$
090424592	189.5	16.8	190.3 ± 0.2	17.7 ± 0.3	1.2	cpl	191.5	18.1	1.6	2.3	$4.6 \cdot 10^{-5}$	$1.1 \cdot 10^{2}$
090510016*	333.6	-26.6	334.5 ± 1.7	−30.3 ± 1.6	3.8	cpl	335.0	-31.3	1.0	4.9	$3.4 \cdot 10^{-6}$	9.1
090531775*	252.1	-36.0	249.8 ± 6.1	−33.7 ± 3.4	3.0	cpl	252.9	-31.5	7.2	4.5	$3.2 \cdot 10^{-7}$	3.4
090618353	294.0	78.4	285.3 ± 2.9	79.7 ± 0.3	2.1	cpl	288.4	80.0	1.0	1.9	$2.7 \cdot 10^{-4}$	$6.9 \cdot 10^{1}$
090813174	225.1	88.6	280.9 ± 28.9	87.3 ± 1.3	2.2	cpl	40.2	86.0	5.1	5.4	$3.3 \cdot 10^{-6}$	$1.4 \cdot 10^{1}$
090902462	264.9	27.3	262.5 ± 0.5	26.3 ± 0.3	2.4	cpl	261.4	26.1	1.0	3.3	$2.2 \cdot 10^{-4}$	$7.7 \cdot 10^{1}$
090904058	264.2	-25.2	260.4 ± 1.5	−23.4 ± 2.5	3.9	cpl	265.9	-30.1	1.9	5.1	$2.2 \cdot 10^{-5}$	6.8
090926181	353.4	-66.3	354.0 ± 0.5	−66.1 ± 0.1	0.3	cpl	350.1	-63.5	1.0	3.1	$1.5 \cdot 10^{-4}$	$8.1 \cdot 10^{1}$
091003191	251.5	36.6	251.2 ± 0.3	36.3 ± 0.2	0.4	cpl	251.2	37.3	1.0	0.7	$2.3 \cdot 10^{-5}$	$2.9 \cdot 10^{1}$
091020900	175.7	51.0	175.1 ± 3.3	50.1 ± 2.0	1.0	cpl	174.4	52.7	3.1	1.9	$8.3 \cdot 10^{-6}$	6.8
091112737	257.7	-36.7	254.0 ± 2.7	−41.6 ± 3.1	5.7	cpl	258.3	-36.7	3.2	0.5	$9.9 \cdot 10^{-6}$	4.2
091127976	36.6	-19.1	38.1 ± 0.5	−18.1 ± 0.5	1.7	cpl	38.1	-21.0	1.1	2.4	$2.1 \cdot 10^{-5}$	$6.8 \cdot 10^{1}$
091208410	29.4	16.9	28.5 ± 0.9	16.6 ± 1.1	0.9	pl	30.1	13.5	2.6	3.5	$6.2 \cdot 10^{-6}$	$2.1 \cdot 10^{1}$
091221870	55.8	23.2	57.4 ± 2.4	22.1 ± 1.4	1.8	cpl	54.5	27.3	1.2	4.3	$8.9 \cdot 10^{-6}$	4.3
100401297	290.8	-8.3	295.4 ± 4.1	−10.4 ± 3.9	5.0	pl	290.0	-16.3	7.9	8.0	$1.9 \cdot 10^{-6}$	4.1
100414097	192.1	8.7	191.8 ± 0.6	8.1 ± 0.6	0.6	band	185.7	15.7	1.0	9.4	$8.8 \cdot 10^{-5}$	$2.2 \cdot 10^{1}$
100427356	89.2	-3.5	86.0 ± 1.2	−0.3 ± 1.8	4.5	cpl	91.0	-1.4	2.6	2.8	$2.3 \cdot 10^{-6}$	3.8
100522157	7.0	9.5	8.0 ± 1.2	10.4 ± 1.0	1.4	cpl	8.0	10.5	3.9	1.4	$3.9 \cdot 10^{-6}$	$1.1 \cdot 10^{1}$
100615083	177.2	-19.5	173.1 ± 2.6	−20.1 ± 2.4	3.9	pl	175.6	-21.1	2.4	2.2	$8.7 \cdot 10^{-6}$	8.3
100619015	84.6	-27.1	86.1 ± 2.4	−20.0 ± 3.0	7.2	pl	84.0	-25.5	6.6	1.7	$1.1 \cdot 10^{-5}$	7.4
100704149	133.6	-24.2	133.5 ± 1.3	−20.0 ± 2.3	4.2	cpl	133.2	-23.6	1.6	0.7	$8.4 \cdot 10^{-6}$	7.2
100728095	88.8	-15.3	91.8 ± 1.0	−14.2 ± 0.9	3.1	cpl	88.3	-13.7	1.0	1.7	$1.3 \cdot 10^{-4}$	$1.1 \cdot 10^{1}$
100728439	44.1	0.3	41.0 ± 2.4	1.9 ± 1.6	3.4	pl	41.5	0.2	4.2	2.6	$3.3 \cdot 10^{-6}$	6.2
100906576	28.7	55.6	24.9 ± 1.1	53.6 ± 0.6	3.0	cpl	28.0	55.2	1.1	0.6	$2.3 \cdot 10^{-5}$	$1.4 \cdot 10^{1}$
101024486	66.5	-77.3	89.4 ± 49.8	−74.0 ± 5.9	6.5	pl	147.1	-77.2	9.6	16.4	$3.3 \cdot 10^{-6}$	8.3
101201418	1.9	-16.1	3.2 ± 0.8	−14.1 ± 1.2	2.4	band	3.9	-14.7	1.6	2.4	$2.4 \cdot 10^{-5}$	6.9
110102788	245.9	7.6	245.3 ± 0.9	5.6 ± 0.8	2.1	cpl	246.2	6.0	2.0	1.6	$3.7 \cdot 10^{-5}$	$1.4 \cdot 10^{1}$
110213220	43.0	49.3	39.6 ± 1.7	47.9 ± 1.2	2.7	pl	49.0	52.8	2.3	5.1	$9.4 \cdot 10^{-6}$	$1.8 \cdot 10^{1}$
110318552	338.3	-15.3	337.9 ± 0.9	−17.8 ± 1.1	2.5	cpl	335.9	-14.9	1.9	2.4	$8.2 \cdot 10^{-6}$	$1.1 \cdot 10^{1}$

Trigger	*Swift*		BALROG				DoL				Data	
	RA (°)	DEC (°)	RA (°)	DEC (°)	Offset (°)	Model	RA (°)	DEC (°)	Err. (°)	Offset (°)	Fluence ($\mathrm{erg} \cdot \mathrm{cm}^{-2}$)	Peak flux ($\mathrm{ph} \cdot \mathrm{cm}^{-2} \cdot \mathrm{s}^{-1}$)
110402009	197.4	61.4	196.7 ± 9.1	57.9 ± 3.6	3.5	cpl	187.7	58.7	2.2	5.5	$1.1 \cdot 10^{-5}$	7.8
110610640	308.2	74.8	300.9 ± 5.8	73.7 ± 1.2	2.3	pl	306.5	75.9	2.6	1.2	$8.0 \cdot 10^{-6}$	5.8
110625881	286.8	6.8	287.7 ± 0.2	8.2 ± 0.2	1.6	cpl	287.7	6.7	1.0	0.9	$6.5 \cdot 10^{-5}$	$7.7 \cdot 10^{1}$
110709642	238.9	40.9	238.5 ± 1.3	39.0 ± 1.5	1.9	cpl	241.2	41.8	1.1	1.9	$3.7 \cdot 10^{-5}$	$1.1 \cdot 10^{1}$
110731465	280.5	-28.5	281.8 ± 0.3	−26.5 ± 0.7	2.3	cpl	283.1	-34.0	1.0	5.9	$2.3 \cdot 10^{-5}$	$2.1 \cdot 10^{1}$
111228657	150.1	18.3	148.8 ± 0.4	19.1 ± 1.2	1.5	pl	146.6	14.6	2.4	5.0	$1.8 \cdot 10^{-5}$	$2.1 \cdot 10^{1}$
120102095	276.2	24.7	275.6 ± 1.3	21.1 ± 0.7	3.6	cpl	277.1	20.4	2.0	4.4	$1.3 \cdot 10^{-5}$	$1.9 \cdot 10^{1}$
120119170	120.0	-9.1	120.1 ± 0.5	−8.9 ± 0.6	0.2	cpl	119.0	-9.0	1.1	1.0	$3.9 \cdot 10^{-5}$	$1.7 \cdot 10^{1}$
120326056	273.9	69.3	276.5 ± 3.7	70.5 ± 1.7	1.5	pl	262.2	62.1	4.2	8.6	$3.3 \cdot 10^{-6}$	7.7
120624933	170.9	8.9	171.1 ± 1.1	10.2 ± 0.9	1.3	cpl	171.8	5.6	1.0	3.4	$1.9 \cdot 10^{-4}$	$1.8 \cdot 10^{1}$
120703726	339.4	-29.7	335.1 ± 1.9	−31.0 ± 1.3	3.9	cpl	339.8	-29.5	1.7	0.4	$8.3 \cdot 10^{-6}$	$1.7 \cdot 10^{1}$
120913997	213.6	-14.5	217.0 ± 2.1	−18.9 ± 1.2	5.5	pl	214.8	-16.6	1.5	2.4	$2.0 \cdot 10^{-5}$	5.3
121031949	170.8	-3.5	170.1 ± 2.2	−5.8 ± 2.8	2.4	pl	173.1	-1.9	3.4	2.8	$1.5 \cdot 10^{-5}$	7.4
121128212	300.6	54.3	300.2 ± 1.9	57.3 ± 1.3	3.0	cpl	278.8	41.6	1.5	19.2	$9.3 \cdot 10^{-6}$	$1.8 \cdot 10^{1}$
130216790	58.9	2.0	61.3 ± 1.0	1.2 ± 1.0	2.5	pl	61.7	3.5	2.3	3.2	$4.9 \cdot 10^{-6}$	$1.5 \cdot 10^{1}$
130216927	67.9	14.7	70.8 ± 0.6	16.0 ± 1.0	3.0	pl	69.4	16.3	1.5	2.2	$5.9 \cdot 10^{-6}$	9.2
130305486	116.8	52.0	115.5 ± 0.6	51.6 ± 0.6	0.9	cpl	119.7	49.0	1.0	3.5	$4.6 \cdot 10^{-5}$	$2.7 \cdot 10^{1}$
130306991	279.5	-11.8	276.1 ± 0.6	−11.6 ± 0.4	3.3	cpl	276.9	-11.5	1.0	2.6	$1.2 \cdot 10^{-4}$	$2.9 \cdot 10^{1}$
130420313	196.1	59.4	185.0 ± 11.4	55.3 ± 4.7	7.3	cpl	205.7	58.8	4.4	5.0	$1.2 \cdot 10^{-5}$	5.4
130427324	173.1	27.7	174.2 ± 0.0	26.9 ± 0.1	1.3	cpl	172.5	25.5	1.0	2.3	$2.5 \cdot 10^{-3}$	$1.1 \cdot 10^{3}$
130502327	66.8	71.1	66.9 ± 1.9	71.0 ± 0.6	0.1	cpl	77.0	70.3	1.0	3.5	$1.0 \cdot 10^{-4}$	$4.6 \cdot 10^{1}$
130504978	91.6	3.8	94.6 ± 0.4	4.2 ± 0.3	3.0	cpl	90.7	4.3	1.0	1.0	$1.3 \cdot 10^{-4}$	$4.3 \cdot 10^{1}$
130518580	355.7	47.5	352.8 ± 0.4	46.9 ± 0.3	2.1	cpl	356.3	47.0	1.0	0.6	$9.5 \cdot 10^{-5}$	$4.5 \cdot 10^{1}$
130609902	53.8	-40.2	50.1 ± 1.8	−37.9 ± 1.3	3.7	cpl	51.9	-42.9	1.0	3.1	$5.4 \cdot 10^{-5}$	$1.4 \cdot 10^{1}$
130727698	330.8	-65.5	329.6 ± 4.4	−61.3 ± 4.2	4.3	cpl	-	-	-	-	$8.2 \cdot 10^{-6}$	$1.1 \cdot 10^{1}$
130925173	41.2	-26.1	43.6 ± 1.9	−25.1 ± 0.7	2.4	cpl	-	-	-	-	$8.5 \cdot 10^{-5}$	$1.1 \cdot 10^{1}$
131229277	85.2	-4.4	86.5 ± 1.1	−6.8 ± 1.4	2.7	cpl	-	-	-	-	$2.6 \cdot 10^{-5}$	$2.4 \cdot 10^{1}$
140108721	325.1	58.7	326.1 ± 2.4	59.3 ± 1.2	0.7	cpl	-	-	-	-	$2.0 \cdot 10^{-5}$	$1.0 \cdot 10^{1}$
140206304	145.3	66.8	147.9 ± 1.7	68.3 ± 1.1	1.9	cpl	-	-	-	-	$1.6 \cdot 10^{-5}$	$1.7 \cdot 10^{1}$
140209313*	81.3	32.5	81.8 ± 0.8	29.6 ± 0.5	2.9	cpl	-	-	-	-	$9.0 \cdot 10^{-6}$	$5.8 \cdot 10^{1}$
140213807	105.2	-73.1	102.7 ± 16.6	−71.9 ± 1.0	1.5	cpl	-	-	-	-	$2.1 \cdot 10^{-5}$	$3.7 \cdot 10^{1}$
140323433	357.0	-79.9	356.0 ± 5.2	−77.2 ± 1.3	2.7	cpl	-	-	-	-	$3.2 \cdot 10^{-5}$	9.7
140506880	276.8	-55.6	275.6 ± 5.8	−56.4 ± 3.0	1.1	cpl	-	-	-	-	$6.6 \cdot 10^{-6}$	$1.6 \cdot 10^{1}$
140512814	289.4	-15.1	294.1 ± 2.3	−19.5 ± 1.8	6.3	cpl	-	-	-	-	$2.9 \cdot 10^{-5}$	$1.1 \cdot 10^{1}$
140716436	108.1	-60.1	102.2 ± 2.7	−65.2 ± 2.2	5.7	cpl	-	-	-	-	$1.2 \cdot 10^{-5}$	$1.1 \cdot 10^{1}$
141004973	76.7	12.8	78.0 ± 2.7	11.7 ± 2.9	1.7	cpl	-	-	-	-	$1.2 \cdot 10^{-6}$	9.8
141220252	195.1	32.1	198.5 ± 1.0	32.1 ± 1.4	2.9	pl	-	-	-	-	$5.3 \cdot 10^{-6}$	$1.2 \cdot 10^{1}$
150201574	11.8	-37.6	11.3 ± 0.5	−38.0 ± 0.2	0.6	cpl	-	-	-	-	$6.3 \cdot 10^{-5}$	$8.9 \cdot 10^{1}$
150309958	277.0	86.4	276.3 ± 15.6	86.7 ± 0.9	0.3	cpl	-	-	-	-	$4.0 \cdot 10^{-5}$	$1.5 \cdot 10^{1}$
150323395	260.5	38.3	263.3 ± 3.6	38.0 ± 3.8	2.3	cpl	-	-	-	-	$1.9 \cdot 10^{-5}$	8.9
150403913	311.5	-62.7	310.1 ± 0.7	−60.5 ± 0.5	2.3	cpl	-	-	-	-	$5.5 \cdot 10^{-5}$	$3.3 \cdot 10^{1}$
150430015	326.5	-27.9	325.2 ± 1.1	−27.4 ± 1.8	1.2	cpl	-	-	-	-	$1.6 \cdot 10^{-5}$	9.9
150817087	249.6	-12.1	251.0 ± 1.4	−11.7 ± 1.4	1.4	cpl	-	-	-	-	$1.2 \cdot 10^{-5}$	$1.6 \cdot 10^{1}$
151027166	272.5	61.4	271.5 ± 2.8	62.2 ± 0.6	1.0	cpl	-	-	-	-	$1.4 \cdot 10^{-5}$	$1.1 \cdot 10^{1}$
151229285	329.4	-20.7	327.9 ± 2.9	−22.8 ± 2.3	2.5	pl	-	-	-	-	$1.1 \cdot 10^{-6}$	$1.1 \cdot 10^{1}$
160325291	15.7	-72.7	13.5 ± 3.4	−74.0 ± 1.0	1.5	cpl	-	-	-	-	$1.9 \cdot 10^{-5}$	8.5
160905471	162.2	-50.8	159.8 ± 0.5	−53.6 ± 0.3	3.1	cpl	-	-	-	-	$7.3 \cdot 10^{-5}$	$1.6 \cdot 10^{1}$
161004964	112.2	-39.9	110.1 ± 0.5	−37.7 ± 0.7	2.7	band	-	-	-	-	$1.7 \cdot 10^{-5}$	$1.6 \cdot 10^{1}$
161117066	322.1	-29.6	323.8 ± 0.8	−28.3 ± 0.7	2.0	cpl	-	-	-	-	$3.1 \cdot 10^{-5}$	$1.0 \cdot 10^{1}$
170126480	263.6	-64.8	264.3 ± 2.5	−67.7 ± 1.1	3.0	cpl	-	-	-	-	$8.5 \cdot 10^{-6}$	$1.2 \cdot 10^{1}$
170208940	127.1	-9.0	128.5 ± 1.1	−6.8 ± 1.4	2.6	cpl	-	-	-	-	$1.0 \cdot 10^{-5}$	$1.2 \cdot 10^{1}$
170405777	219.8	-25.2	217.5 ± 0.8	−27.2 ± 1.0	2.9	cpl	-	-	-	-	$7.4 \cdot 10^{-5}$	$1.6 \cdot 10^{1}$
170607971	7.4	9.2	5.5 ± 1.2	12.5 ± 1.2	3.8	pl	-	-	-	-	$9.4 \cdot 10^{-6}$	$1.5 \cdot 10^{1}$
170626401	165.4	56.5	160.6 ± 1.6	56.1 ± 0.7	2.7	cpl	-	-	-	-	$1.5 \cdot 10^{-5}$	$3.7 \cdot 10^{1}$
170705115	191.7	18.3	192.3 ± 1.0	17.9 ± 0.5	0.7	cpl	-	-	-	-	$1.3 \cdot 10^{-5}$	$2.2 \cdot 10^{1}$
170906030	203.9	-47.1	201.4 ± 0.6	−45.0 ± 0.6	2.8	cpl	-	-	-	-	$9.5 \cdot 10^{-5}$	$2.2 \cdot 10^{1}$
170906039	232.2	-28.3	233.4 ± 1.8	−29.9 ± 1.7	1.9	cpl	-	-	-	-	$3.0 \cdot 10^{-6}$	$1.0 \cdot 10^{1}$
171120556	163.8	22.5	164.6 ± 0.3	23.5 ± 0.4	1.3	cpl	-	-	-	-	$1.6 \cdot 10^{-5}$	$3.6 \cdot 10^{1}$
180113116	19.2	68.7	17.4 ± 2.9	61.8 ± 1.9	6.9	cpl	-	-	-	-	$1.4 \cdot 10^{-5}$	9.3
180404091	53.4	-50.2	55.0 ± 1.7	−52.0 ± 0.8	2.0	cpl	-	-	-	-	$2.8 \cdot 10^{-5}$	8.0

Appendix B: spectral fit results

The following plots display the results of the fits from Chapter 5. On the top left are the light curves with the parameters estimated for each (successful) time bin. The top right shows instead the lightcurves for the signal-to-noise ratio (computed as described in Vianello (2018)). The first one is for the brightest NaI detector, while the second is for the BGO detector. Time bins with unsuccessful fit are marked in red.
On the bottom are instead the spectra for each of the accepted bins: on the left for the photospheric model and on the right the for Band function equivalent. The shaded are surrounding each spectra denotes the 68% credible region. GRBs with no successful fits are not displayed.

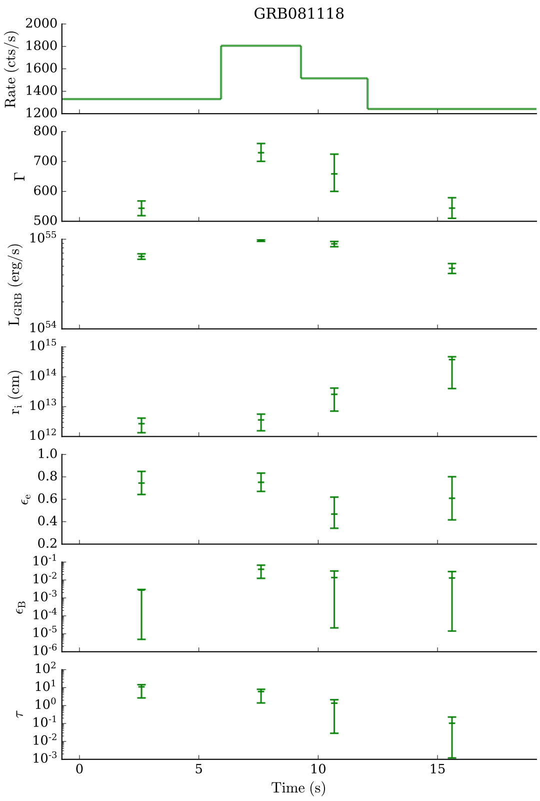
GRB081118
Rate (cts/s)
2000
1800
1600
1400
1200
Γ
800
700
600
500
L_{GRB} (erg/s)
10^{55}
10^{54}
r_i (cm)
10^{15}
10^{14}
10^{13}
10^{12}
ϵ_e
1.0
0.8
0.6
0.4
0.2
ϵ_B
10^{-1}
10^{-2}
10^{-3}
10^{-4}
10^{-5}
10^{-6}
τ
10^{2}
10^{1}
10^{0}
10^{-1}
10^{-2}
10^{-3}
0
5
10
15
Time (s)

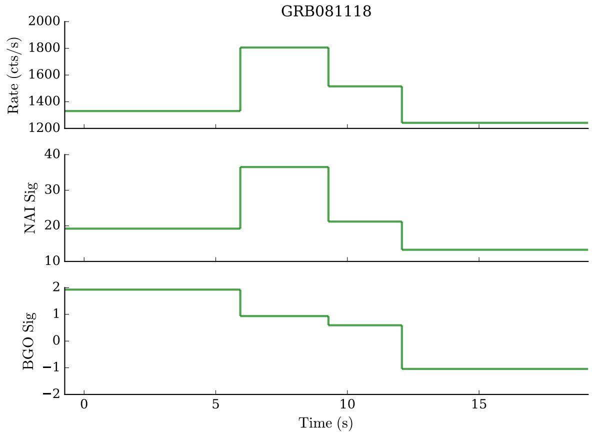
GRB081118
Rate (cts/s)
2000
1800
1600
1400
1200
NAI Sig
40
30
20
10
BGO Sig
2
1
0
−1
−2
0
5
10
15
Time (s)

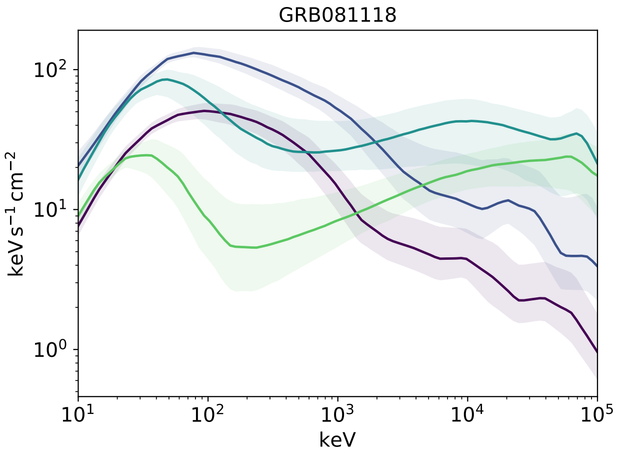
GRB081118
$\mathrm{keV\,s^{-1}\,cm^{-2}}$
10^{2}
10^{1}
10^{0}
10^{1}
10^{2}
10^{3}
10^{4}
10^{5}
keV

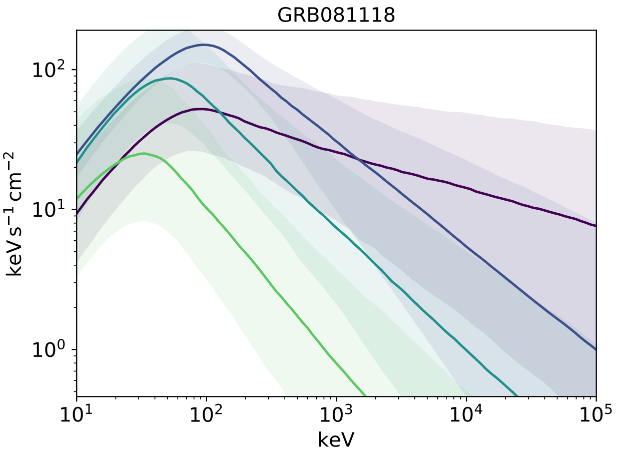
GRB081118
$\mathrm{keV\,s^{-1}\,cm^{-2}}$
10^{2}
10^{1}
10^{0}
10^{1}
10^{2}
10^{3}
10^{4}
10^{5}
keV

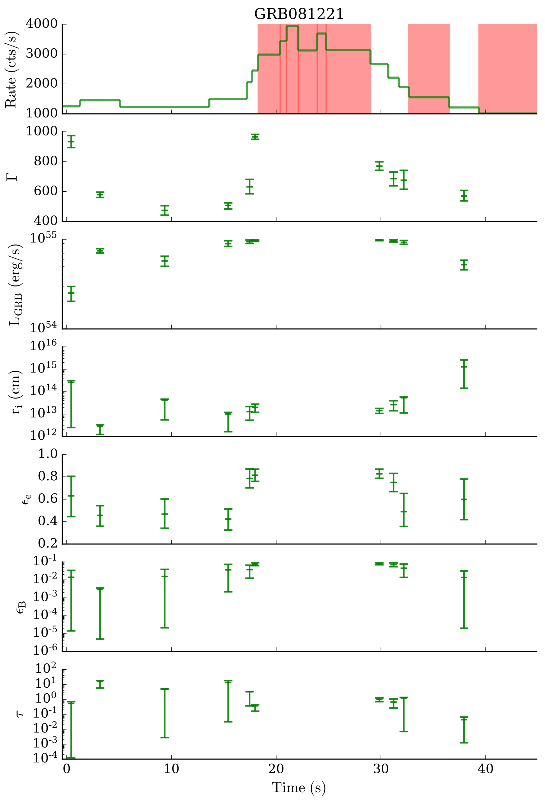
GRB081221
Rate (cts/s)
4000
3000
2000
1000
Γ
1000
800
600
400
L_{GRB} (erg/s)
10^{55}
10^{54}
r_i (cm)
10^{16}
10^{15}
10^{14}
10^{13}
10^{12}
ϵ_e
1.0
0.8
0.6
0.4
0.2
ϵ_B
10^{-1}
10^{-2}
10^{-3}
10^{-4}
10^{-5}
10^{-6}
τ
10^{2}
10^{1}
10^{0}
10^{-1}
10^{-2}
10^{-3}
10^{-4}
0
10
20
30
40
Time (s)

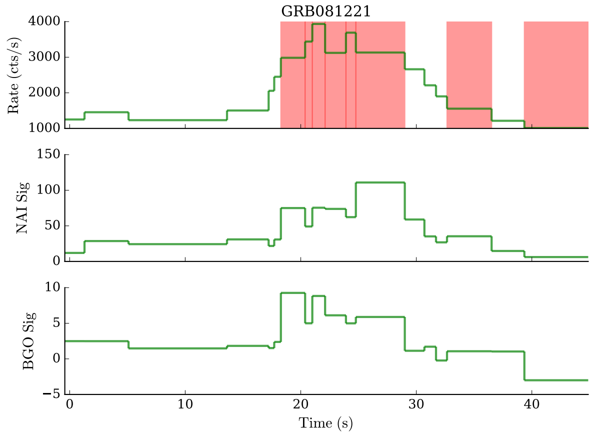
GRB081221
Rate (cts/s)
4000
3000
2000
1000
NAI Sig
150
100
50
0
BGO Sig
10
5
0
−5
0
10
20
30
40
Time (s)

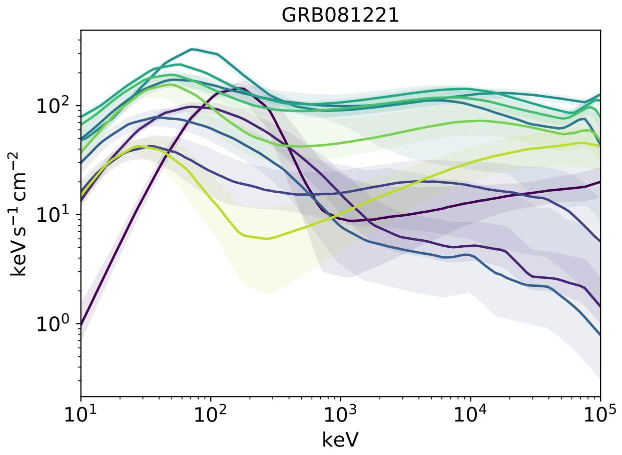
GRB081221
keV s^{-1} cm^{-2}
10^{2}
10^{1}
10^{0}
10^{1}
10^{2}
10^{3}
10^{4}
10^{5}
keV

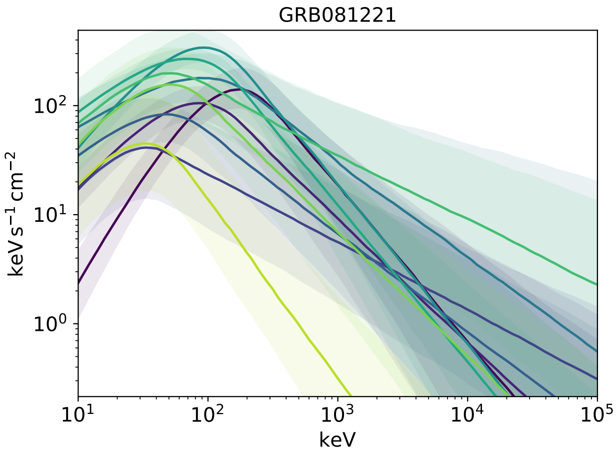
GRB081221
keV s^{-1} cm^{-2}
10^{2}
10^{1}
10^{0}
10^{1}
10^{2}
10^{3}
10^{4}
10^{5}
keV

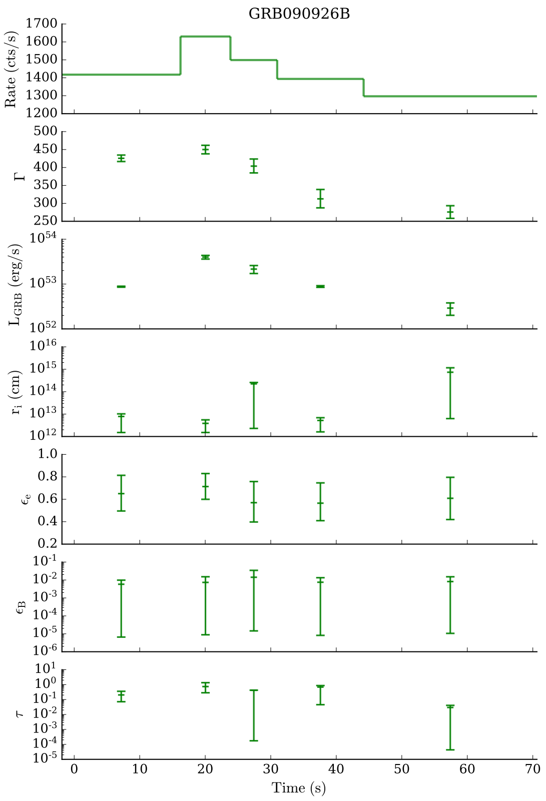
GRB090926B
Rate (cts/s)
1200
1300
1400
1500
1600
1700
Γ
250
300
350
400
450
500
L_{GRB} (erg/s)
10^{52}
10^{53}
10^{54}
r_i (cm)
10^{12}
10^{13}
10^{14}
10^{15}
10^{16}
ϵ_e
0.2
0.4
0.6
0.8
1.0
ϵ_B
10^{-6}
10^{-5}
10^{-4}
10^{-3}
10^{-2}
10^{-1}
τ
10^{-5}
10^{-4}
10^{-3}
10^{-2}
10^{-1}
10^{0}
10^{1}
0
10
20
30
40
50
60
70
Time (s)

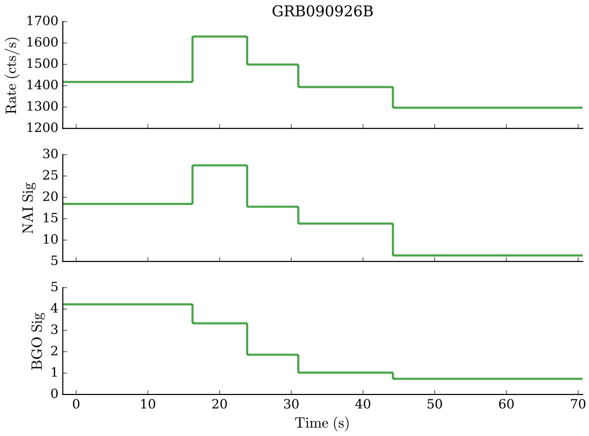
GRB090926B
Rate (cts/s)
1200
1300
1400
1500
1600
1700
NAI Sig
5
10
15
20
25
30
BGO Sig
0
1
2
3
4
5
0
10
20
30
40
50
60
70
Time (s)

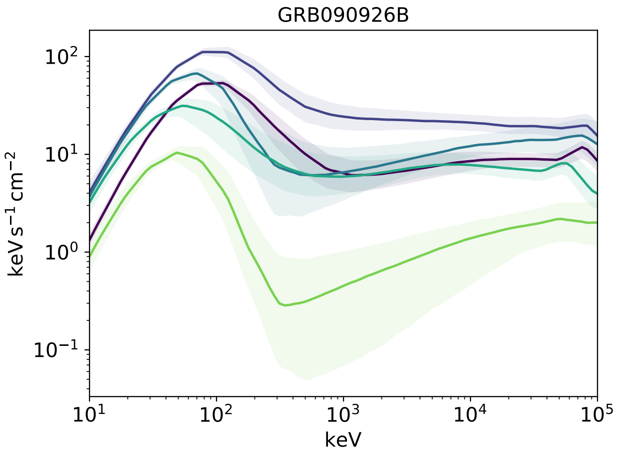
GRB090926B
keV s^{-1} cm^{-2}
10^{-1}
10^{0}
10^{1}
10^{2}
10^{1}
10^{2}
10^{3}
10^{4}
10^{5}
keV

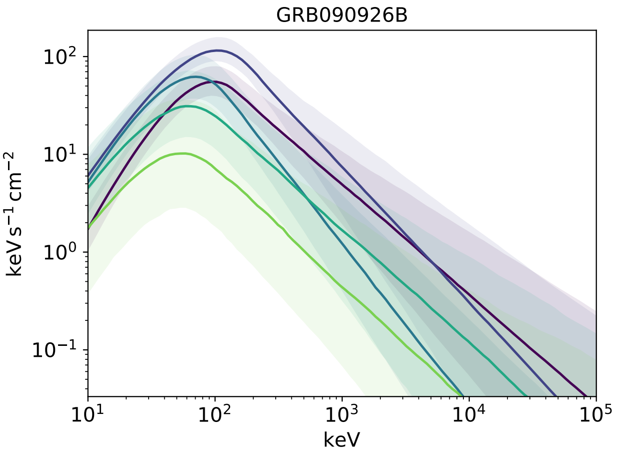
GRB090926B
keV s^{-1} cm^{-2}
10^{-1}
10^{0}
10^{1}
10^{2}
10^{1}
10^{2}
10^{3}
10^{4}
10^{5}
keV

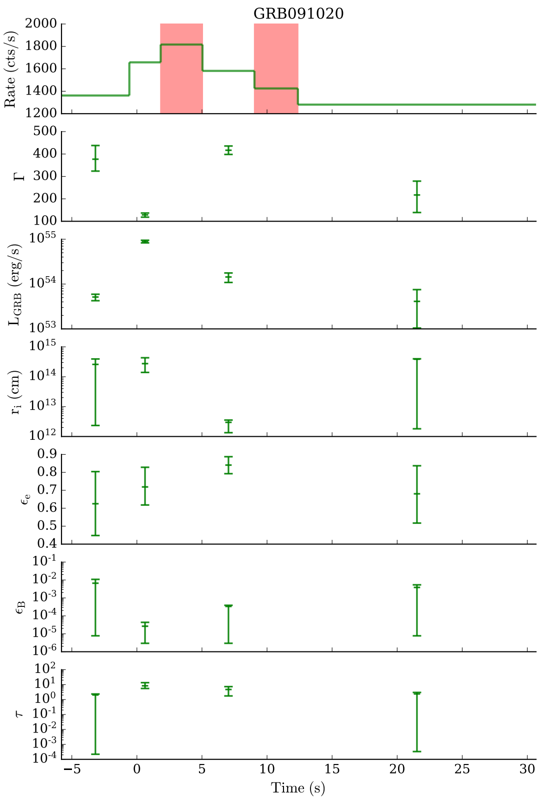
GRB091020
Rate (cts/s)
2000
1800
1600
1400
1200
Γ
500
400
300
200
100
L_{GRB} (erg/s)
10^{55}
10^{54}
10^{53}
r_i (cm)
10^{15}
10^{14}
10^{13}
10^{12}
ϵ_e
0.9
0.8
0.7
0.6
0.5
0.4
ϵ_B
10^{-1}
10^{-2}
10^{-3}
10^{-4}
10^{-5}
10^{-6}
τ
10^{2}
10^{1}
10^{0}
10^{-1}
10^{-2}
10^{-3}
10^{-4}
−5
0
5
10
15
20
25
30
Time (s)

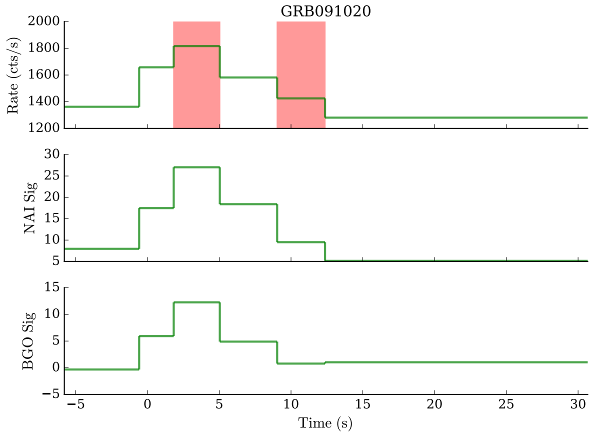
GRB091020
Rate (cts/s)
2000
1800
1600
1400
1200
NAI Sig
30
25
20
15
10
5
BGO Sig
15
10
5
0
−5
−5
0
5
10
15
20
25
30
Time (s)

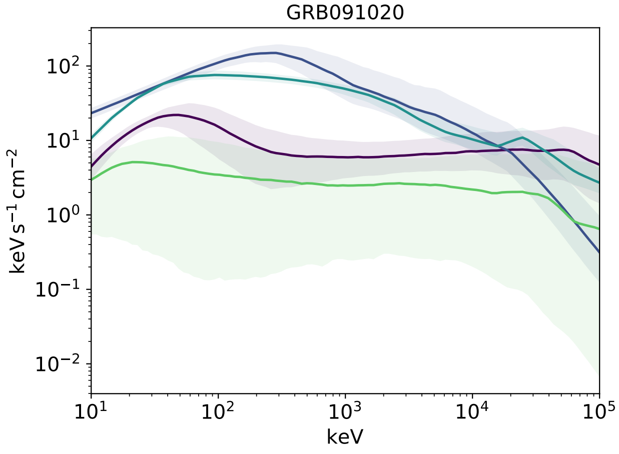
GRB091020
$\mathrm{keV\,s^{-1}\,cm^{-2}}$
10^{2}
10^{1}
10^{0}
10^{-1}
10^{-2}
10^{1}
10^{2}
10^{3}
10^{4}
10^{5}
keV

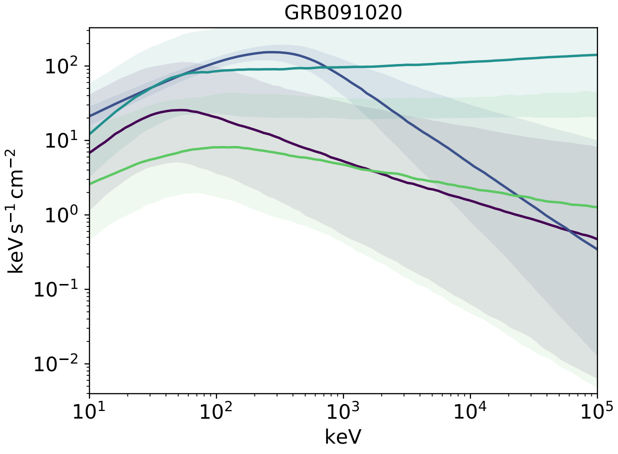
GRB091020
$\mathrm{keV\,s^{-1}\,cm^{-2}}$
10^{2}
10^{1}
10^{0}
10^{-1}
10^{-2}
10^{1}
10^{2}
10^{3}
10^{4}
10^{5}
keV

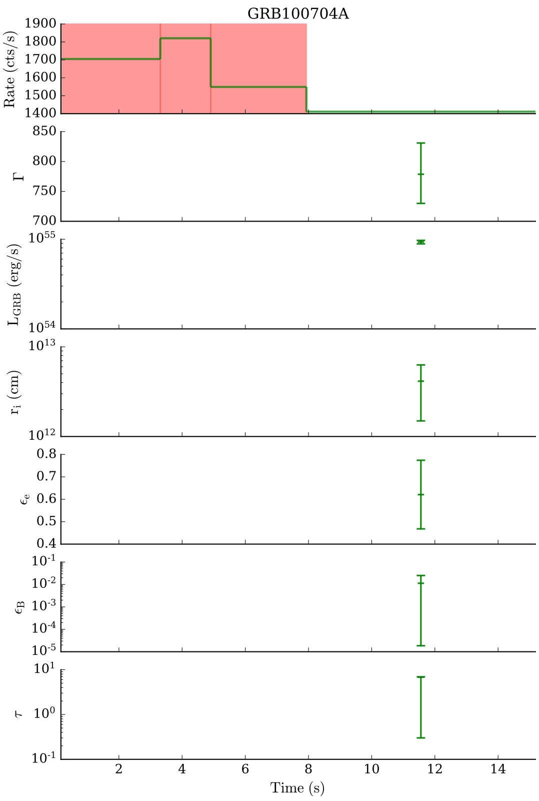
GRB100704A
Rate (cts/s)
1900
1800
1700
1600
1500
1400
Γ
850
800
750
700
L_{GRB} (erg/s)
10^{55}
10^{54}
r_i (cm)
10^{13}
10^{12}
ϵ_e
0.8
0.7
0.6
0.5
0.4
ϵ_B
10^{-1}
10^{-2}
10^{-3}
10^{-4}
10^{-5}
τ
10^{1}
10^{0}
10^{-1}
2
4
6
8
10
12
14
Time (s)

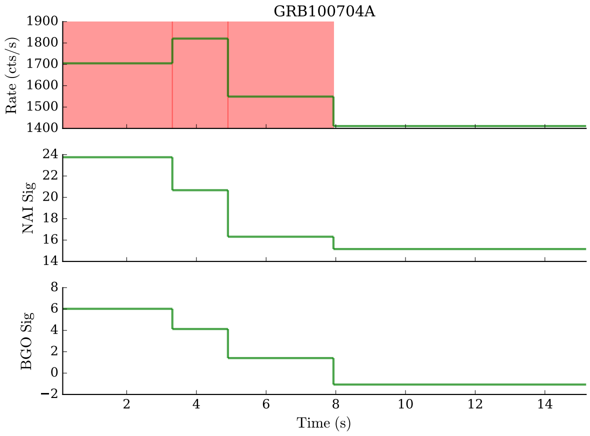
GRB100704A
Rate (cts/s)
1900
1800
1700
1600
1500
1400
NAI Sig
24
22
20
18
16
14
BGO Sig
8
6
4
2
0
−2
2
4
6
8
10
12
14
Time (s)

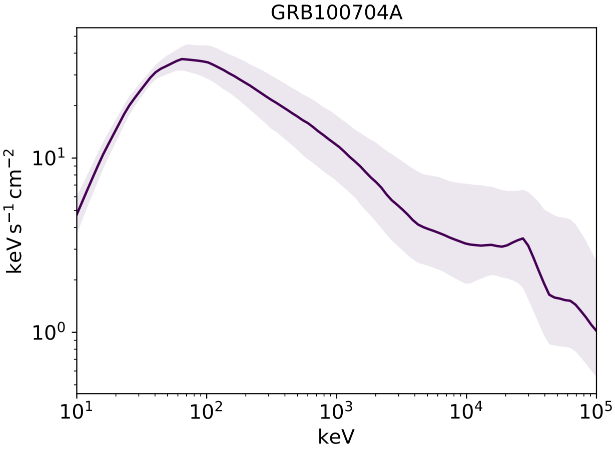
GRB100704A
$\mathrm{keV\,s^{-1}\,cm^{-2}}$
10^{1}
10^{0}
10^{1}
10^{2}
10^{3}
10^{4}
10^{5}
keV

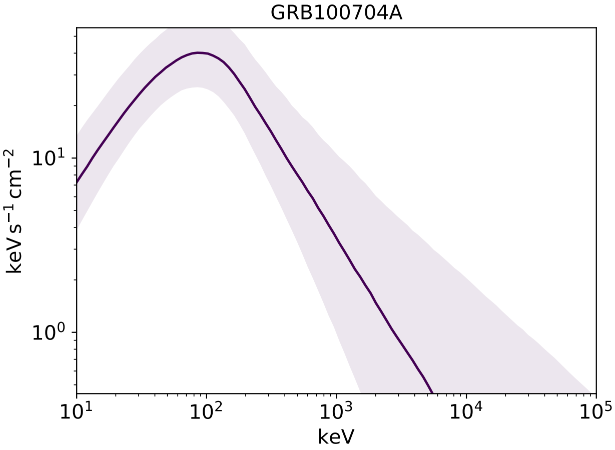
GRB100704A
$\mathrm{keV\,s^{-1}\,cm^{-2}}$
10^{1}
10^{0}
10^{1}
10^{2}
10^{3}
10^{4}
10^{5}
keV

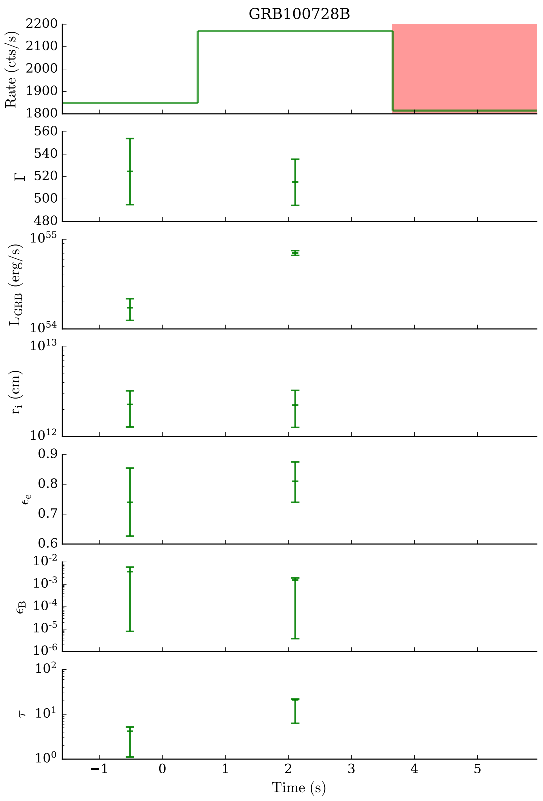
GRB100728B
Rate (cts/s)
1800
1900
2000
2100
2200
Γ
480
500
520
540
560
L_{GRB} (erg/s)
10^{54}
10^{55}
r_i (cm)
10^{12}
10^{13}
ϵ_e
0.6
0.7
0.8
0.9
ϵ_B
10^{-6}
10^{-5}
10^{-4}
10^{-3}
10^{-2}
τ
10^0
10^1
10^2
−1
0
1
2
3
4
5
Time (s)

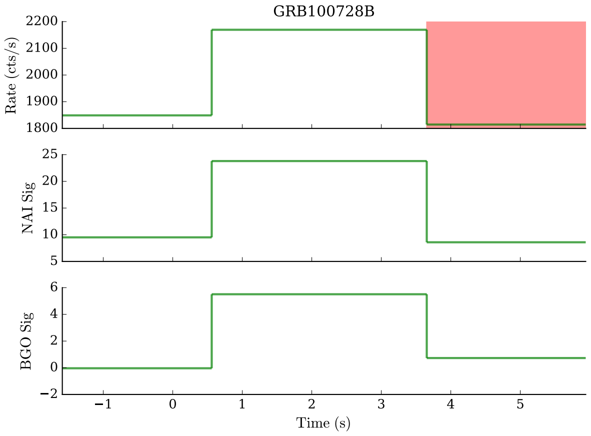
GRB100728B
Rate (cts/s)
1800
1900
2000
2100
2200
NAI Sig
5
10
15
20
25
BGO Sig
−2
0
2
4
6
−1
0
1
2
3
4
5
Time (s)

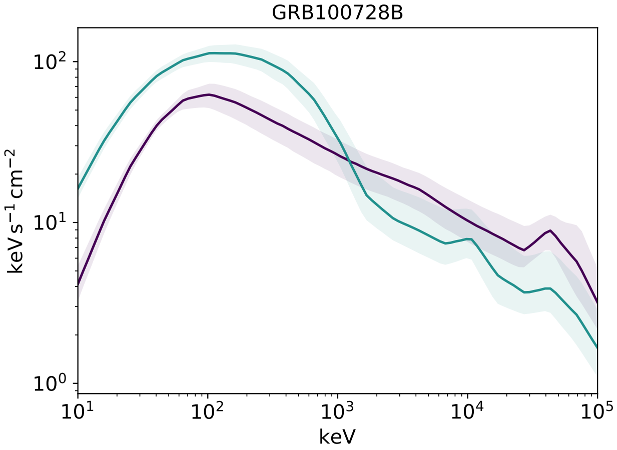
GRB100728B
$\mathrm{keV\,s^{-1}\,cm^{-2}}$
10^0
10^1
10^2
10^1
10^2
10^3
10^4
10^5
keV

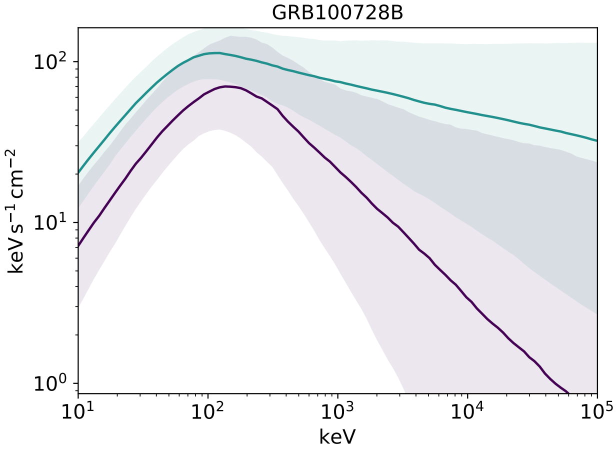
GRB100728B
$\mathrm{keV\,s^{-1}\,cm^{-2}}$
10^0
10^1
10^2
10^1
10^2
10^3
10^4
10^5
keV

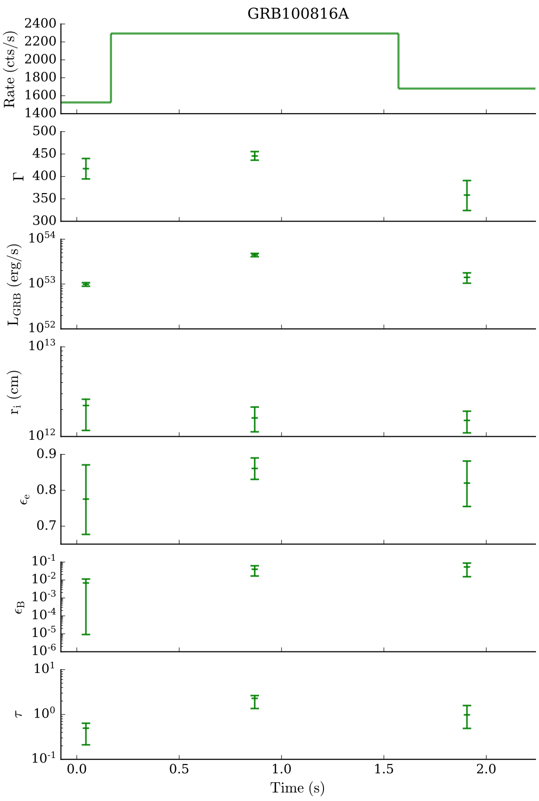
GRB100816A
Rate (cts/s)
2400
2200
2000
1800
1600
1400
Γ
500
450
400
350
300
L_{GRB} (erg/s)
10^{54}
10^{53}
10^{52}
r_i (cm)
10^{13}
10^{12}
ϵ_e
0.9
0.8
0.7
ϵ_B
10^{-1}
10^{-2}
10^{-3}
10^{-4}
10^{-5}
10^{-6}
τ
10^{1}
10^{0}
10^{-1}
0.0
0.5
1.0
1.5
2.0
Time (s)

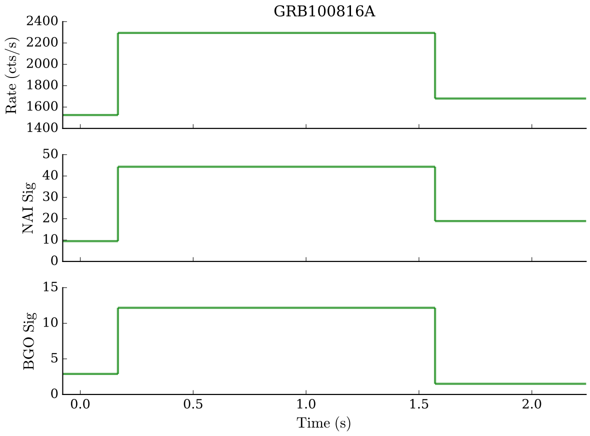
GRB100816A
Rate (cts/s)
2400
2200
2000
1800
1600
1400
NAI Sig
50
40
30
20
10
0
BGO Sig
15
10
5
0
0.0
0.5
1.0
1.5
2.0
Time (s)

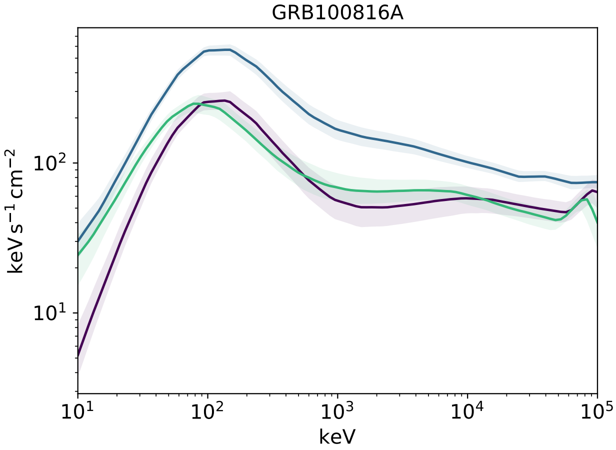
GRB100816A
$\mathrm{keV\,s^{-1}\,cm^{-2}}$
10^{2}
10^{1}
10^{1}
10^{2}
10^{3}
10^{4}
10^{5}
keV

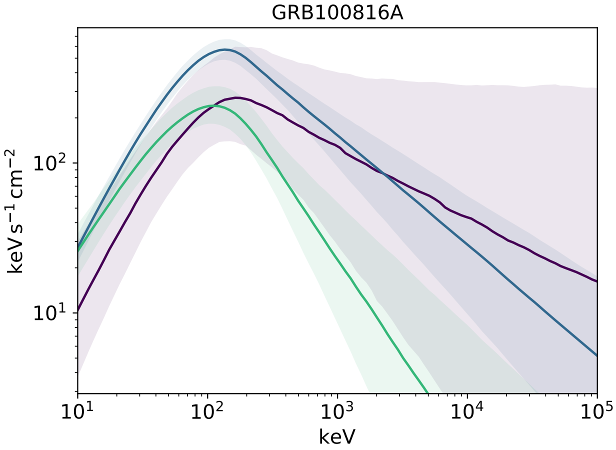
GRB100816A
$\mathrm{keV\,s^{-1}\,cm^{-2}}$
10^{2}
10^{1}
10^{1}
10^{2}
10^{3}
10^{4}
10^{5}
keV

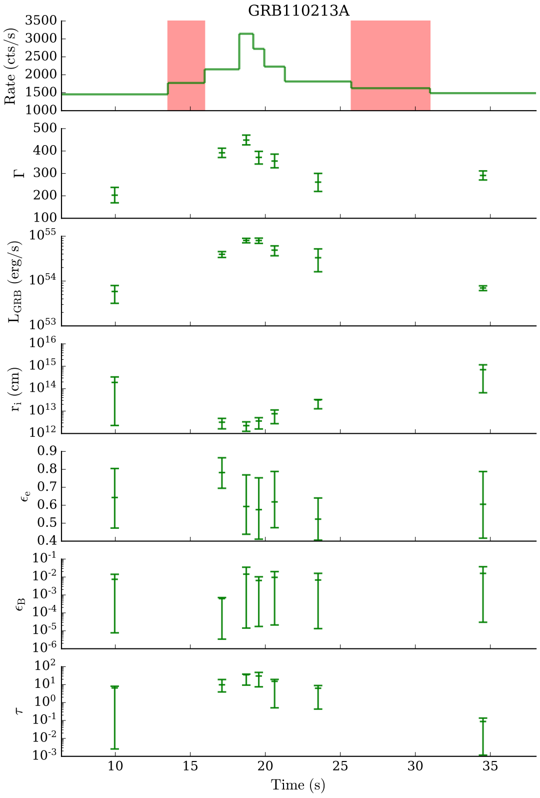
GRB110213A
Rate (cts/s)
3500
3000
2500
2000
1500
1000
Γ
500
400
300
200
100
L_{GRB} (erg/s)
10^{55}
10^{54}
10^{53}
r_i (cm)
10^{16}
10^{15}
10^{14}
10^{13}
10^{12}
ϵ_e
0.9
0.8
0.7
0.6
0.5
0.4
ϵ_B
10^{-1}
10^{-2}
10^{-3}
10^{-4}
10^{-5}
10^{-6}
τ
10^{2}
10^{1}
10^{0}
10^{-1}
10^{-2}
10^{-3}
10
15
20
25
30
35
Time (s)

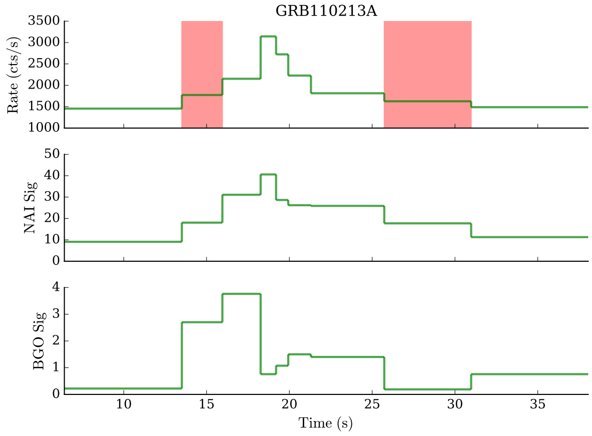
GRB110213A
Rate (cts/s)
3500
3000
2500
2000
1500
1000
NAI Sig
50
40
30
20
10
0
BGO Sig
4
3
2
1
0
10
15
20
25
30
35
Time (s)

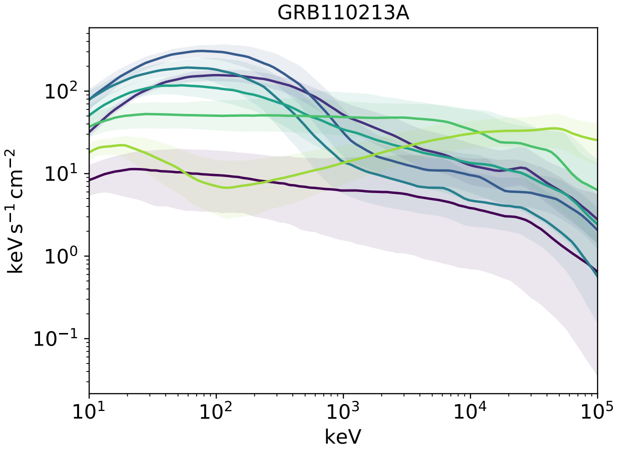
GRB110213A
$\mathrm{keV\,s^{-1}\,cm^{-2}}$
10^{2}
10^{1}
10^{0}
10^{-1}
10^{1}
10^{2}
10^{3}
10^{4}
10^{5}
keV

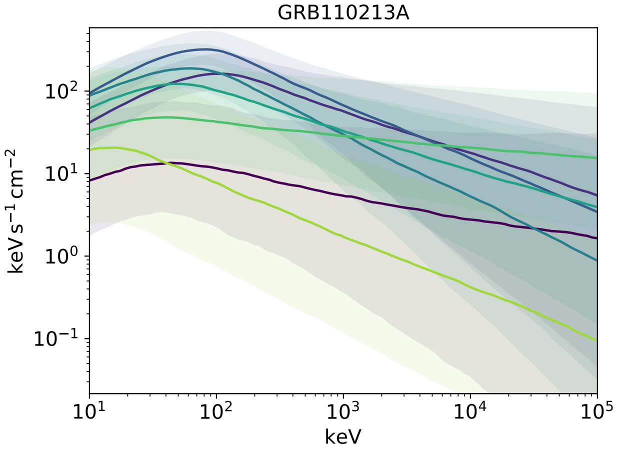
GRB110213A
$\mathrm{keV\,s^{-1}\,cm^{-2}}$
10^{2}
10^{1}
10^{0}
10^{-1}
10^{1}
10^{2}
10^{3}
10^{4}
10^{5}
keV

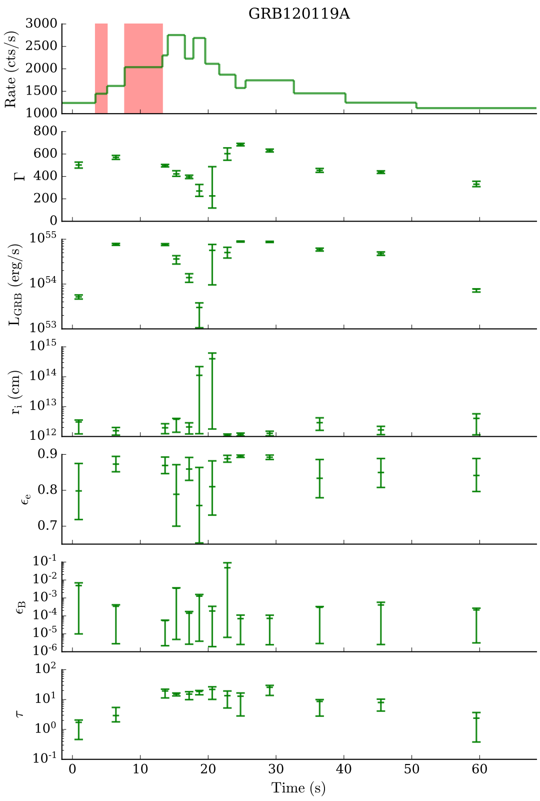
GRB120119A
Rate (cts/s)
3000
2500
2000
1500
1000
Γ
800
600
400
200
0
L_{GRB} (erg/s)
10^{55}
10^{54}
10^{53}
r_i (cm)
10^{15}
10^{14}
10^{13}
10^{12}
ϵ_e
0.9
0.8
0.7
ϵ_B
10^{-1}
10^{-2}
10^{-3}
10^{-4}
10^{-5}
10^{-6}
τ
10^{2}
10^{1}
10^{0}
10^{-1}
0
10
20
30
40
50
60
Time (s)

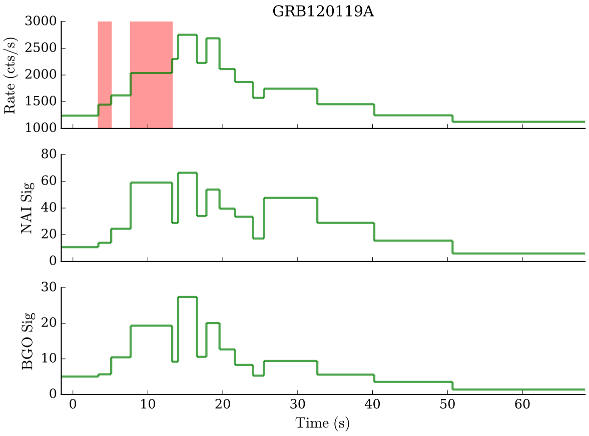
GRB120119A
Rate (cts/s)
3000
2500
2000
1500
1000
NAI Sig
80
60
40
20
0
BGO Sig
30
20
10
0
0
10
20
30
40
50
60
Time (s)

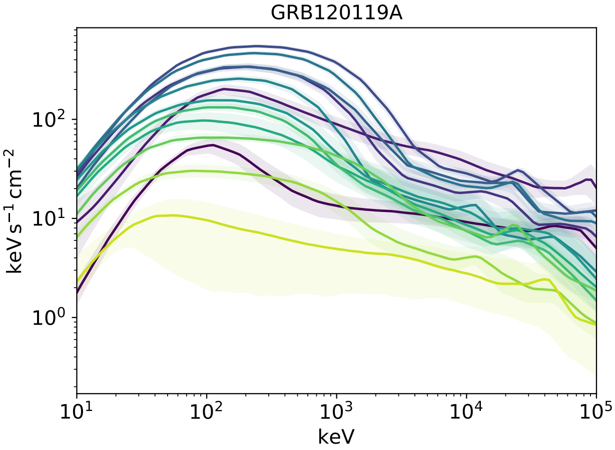
GRB120119A
$\mathrm{keV\,s^{-1}\,cm^{-2}}$
10^{2}
10^{1}
10^{0}
10^{1}
10^{2}
10^{3}
10^{4}
10^{5}
keV

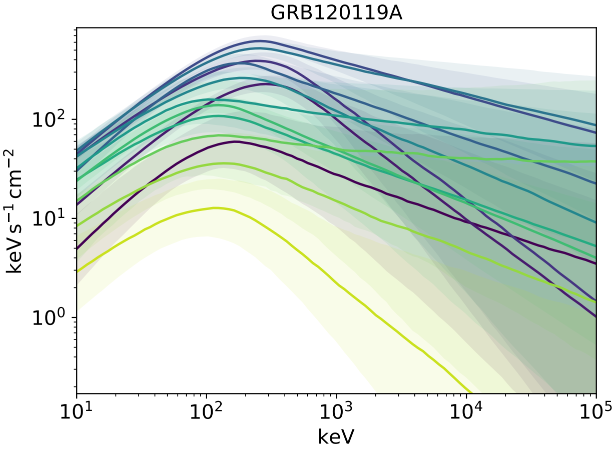
GRB120119A
$\mathrm{keV\,s^{-1}\,cm^{-2}}$
10^{2}
10^{1}
10^{0}
10^{1}
10^{2}
10^{3}
10^{4}
10^{5}
keV

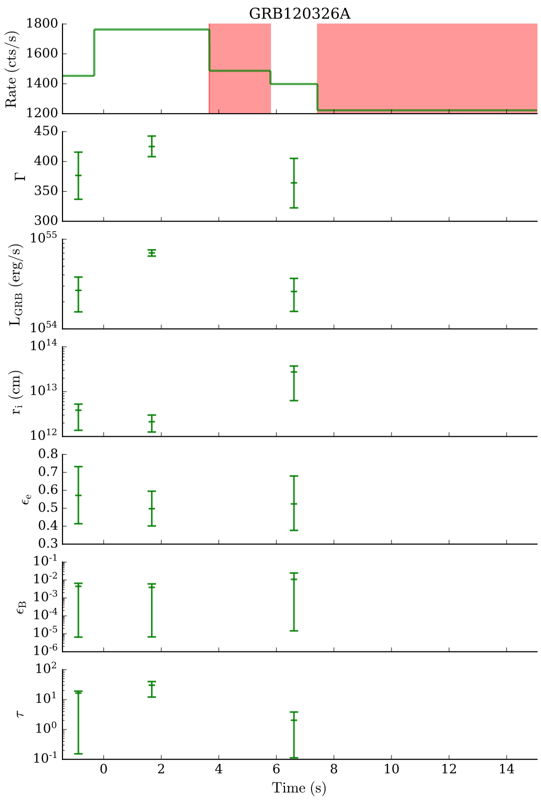
GRB120326A
Rate (cts/s)
1800
1600
1400
1200
Γ
450
400
350
300
L$_{GRB}$ (erg/s)
10^{55}
10^{54}
r$_i$ (cm)
10^{14}
10^{13}
10^{12}
ϵ_e
0.8
0.7
0.6
0.5
0.4
0.3
ϵ_B
10^{-1}
10^{-2}
10^{-3}
10^{-4}
10^{-5}
10^{-6}
τ
10^{2}
10^{1}
10^{0}
10^{-1}
0
2
4
6
8
10
12
14
Time (s)

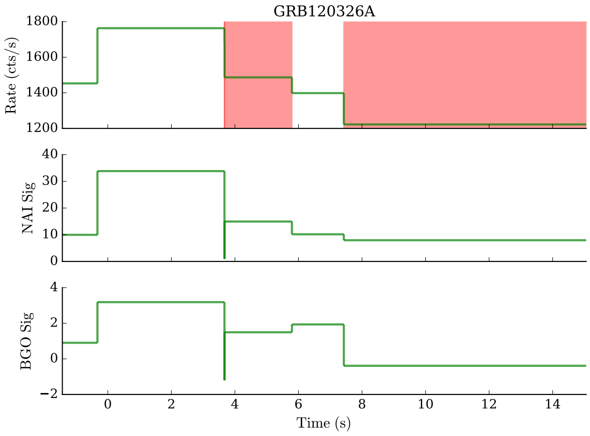
GRB120326A
Rate (cts/s)
1800
1600
1400
1200
NAI Sig
40
30
20
10
0
BGO Sig
4
2
0
−2
0
2
4
6
8
10
12
14
Time (s)

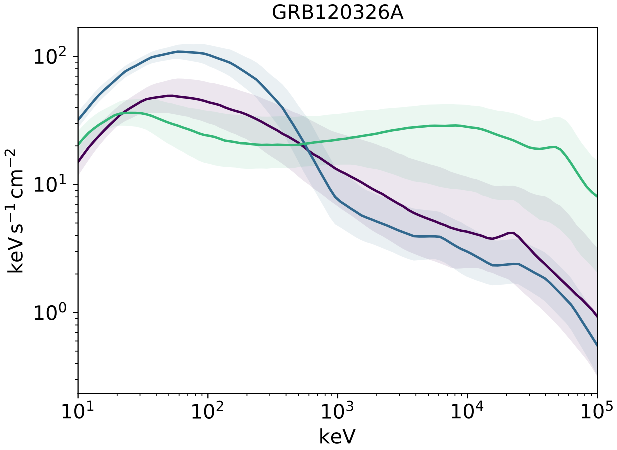
GRB120326A
keV s^{-1} cm^{-2}
10^{2}
10^{1}
10^{0}
10^{1}
10^{2}
10^{3}
10^{4}
10^{5}
keV

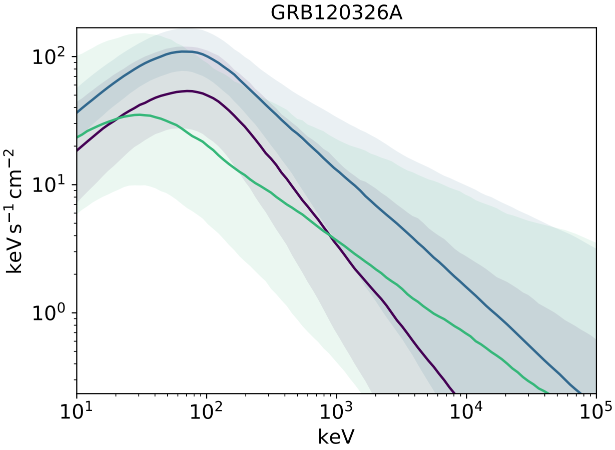
GRB120326A
keV s^{-1} cm^{-2}
10^{2}
10^{1}
10^{0}
10^{1}
10^{2}
10^{3}
10^{4}
10^{5}
keV

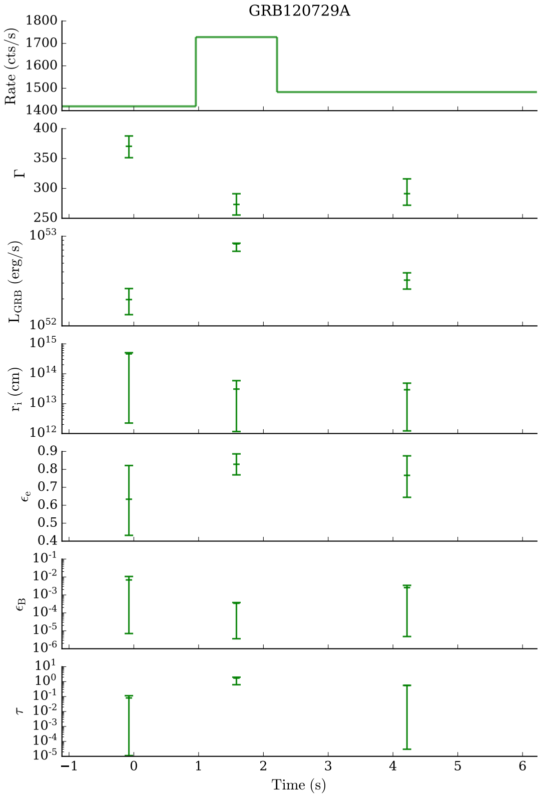
GRB120729A
Rate (cts/s)
1800
1700
1600
1500
1400
Γ
400
350
300
250
L$_{GRB}$ (erg/s)
10^{53}
10^{52}
r$_i$ (cm)
10^{15}
10^{14}
10^{13}
10^{12}
ϵ_e
0.9
0.8
0.7
0.6
0.5
0.4
ϵ_B
10^{-1}
10^{-2}
10^{-3}
10^{-4}
10^{-5}
10^{-6}
τ
10^{1}
10^{0}
10^{-1}
10^{-2}
10^{-3}
10^{-4}
10^{-5}
−1
0
1
2
3
4
5
6
Time (s)

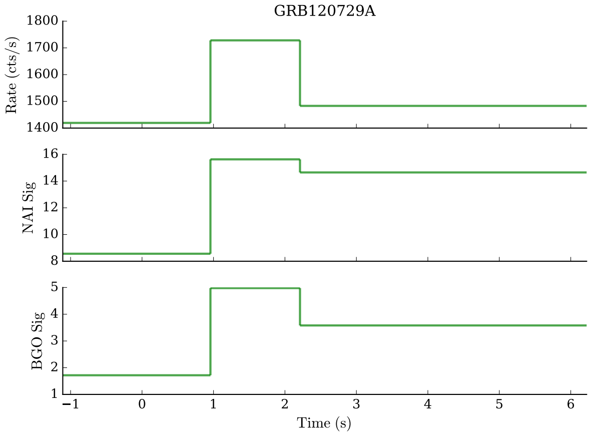
GRB120729A
Rate (cts/s)
1800
1700
1600
1500
1400
NAI Sig
16
14
12
10
8
BGO Sig
5
4
3
2
1
−1
0
1
2
3
4
5
6
Time (s)

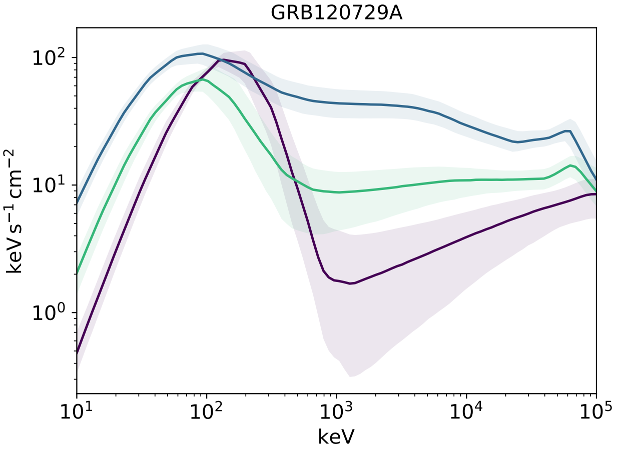
GRB120729A
keV s^{-1} cm^{-2}
10^{2}
10^{1}
10^{0}
10^{1}
10^{2}
10^{3}
10^{4}
10^{5}
keV

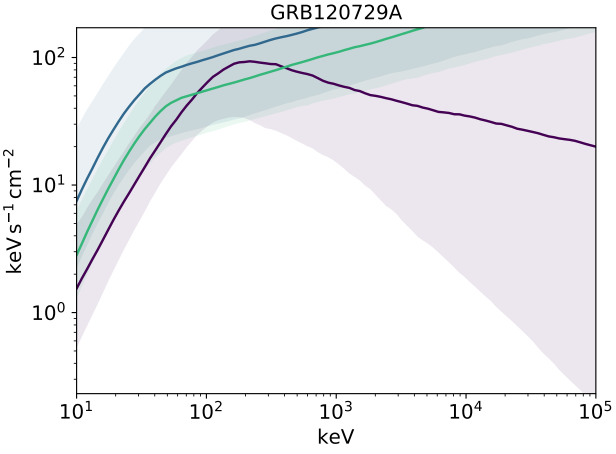
GRB120729A
keV s^{-1} cm^{-2}
10^{2}
10^{1}
10^{0}
10^{1}
10^{2}
10^{3}
10^{4}
10^{5}
keV

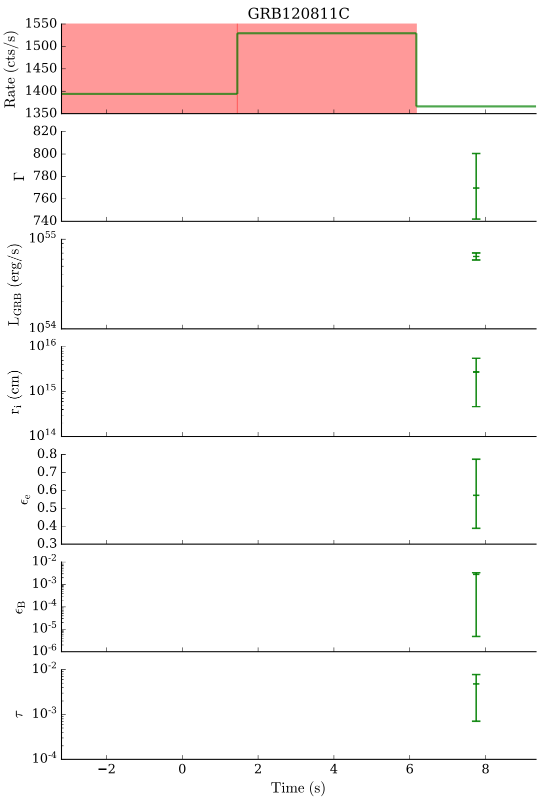
GRB120811C
Rate (cts/s)
1550
1500
1450
1400
1350
Γ
820
800
780
760
740
L_{GRB} (erg/s)
10^{55}
10^{54}
r_i (cm)
10^{16}
10^{15}
10^{14}
ϵ_e
0.8
0.7
0.6
0.5
0.4
0.3
ϵ_B
10^{-2}
10^{-3}
10^{-4}
10^{-5}
10^{-6}
τ
10^{-2}
10^{-3}
10^{-4}
−2
0
2
4
6
8
Time (s)

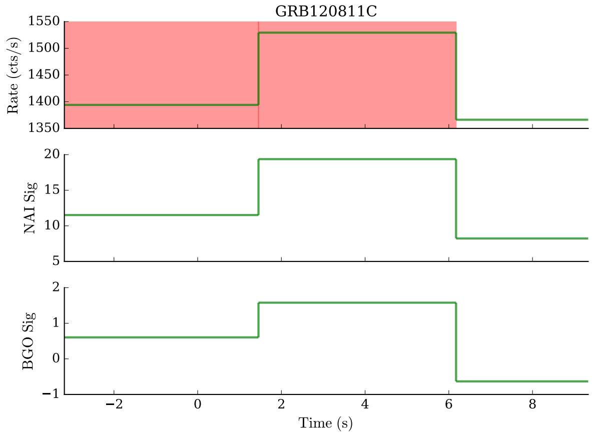
GRB120811C
Rate (cts/s)
1550
1500
1450
1400
1350
NAI Sig
20
15
10
5
BGO Sig
2
1
0
−1
−2
0
2
4
6
8
Time (s)

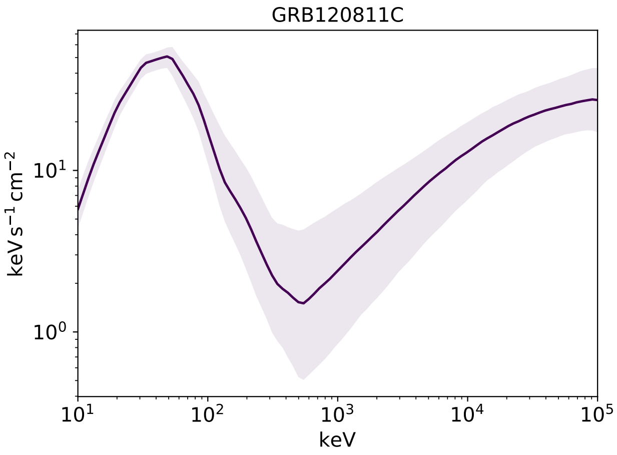
GRB120811C
$\mathrm{keV\,s^{-1}\,cm^{-2}}$
10^1
10^0
10^1
10^2
10^3
10^4
10^5
keV

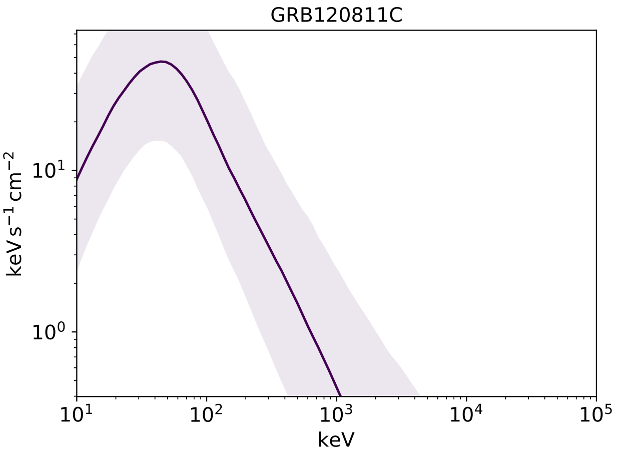
GRB120811C
$\mathrm{keV\,s^{-1}\,cm^{-2}}$
10^1
10^0
10^1
10^2
10^3
10^4
10^5
keV

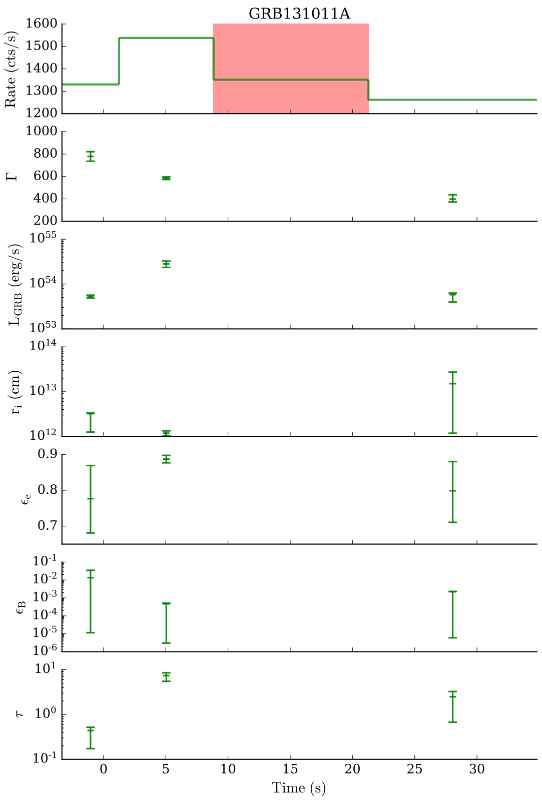
GRB131011A
Rate (cts/s)
1200
1300
1400
1500
1600
Γ
200
400
600
800
1000
L_GRB (erg/s)
10^53
10^54
10^55
r_i (cm)
10^12
10^13
10^14
ε_e
0.7
0.8
0.9
ε_B
10^-6
10^-5
10^-4
10^-3
10^-2
10^-1
τ
10^-1
10^0
10^1
0
5
10
15
20
25
30
Time (s)

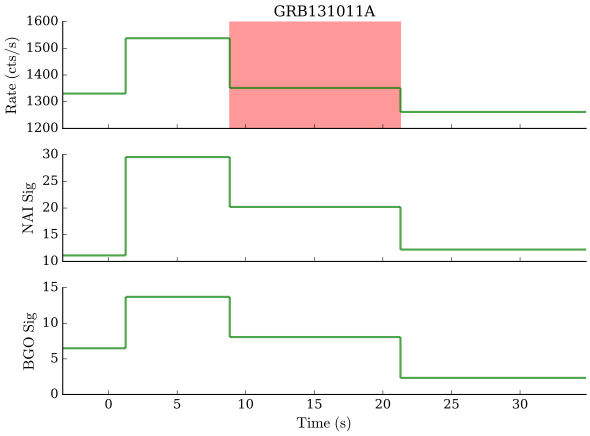
GRB131011A
Rate (cts/s)
1200
1300
1400
1500
1600
NAI Sig
10
15
20
25
30
BGO Sig
0
5
10
15
0
5
10
15
20
25
30
Time (s)

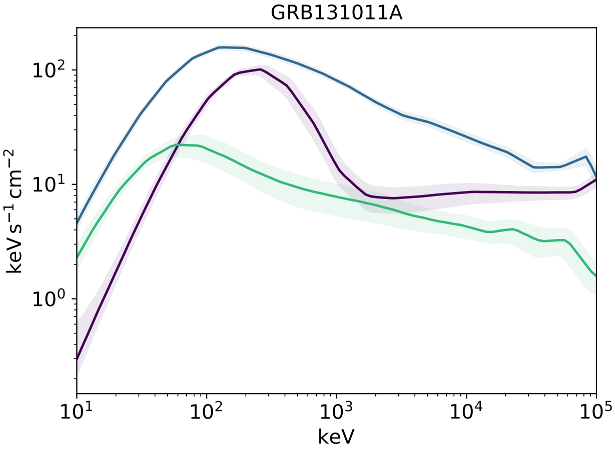
GRB131011A
keV s^-1 cm^-2
10^0
10^1
10^2
10^1
10^2
10^3
10^4
10^5
keV

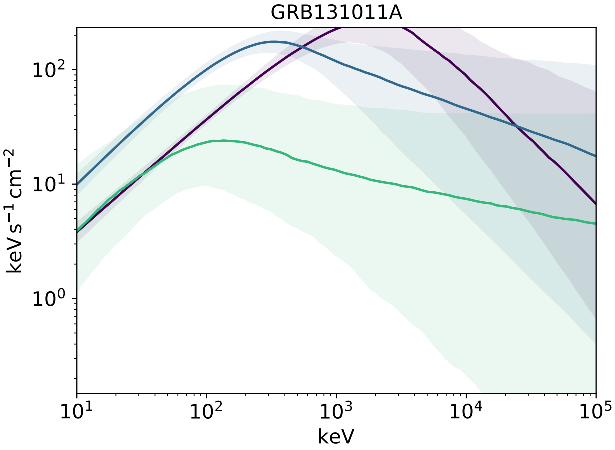
GRB131011A
keV s^-1 cm^-2
10^0
10^1
10^2
10^1
10^2
10^3
10^4
10^5
keV

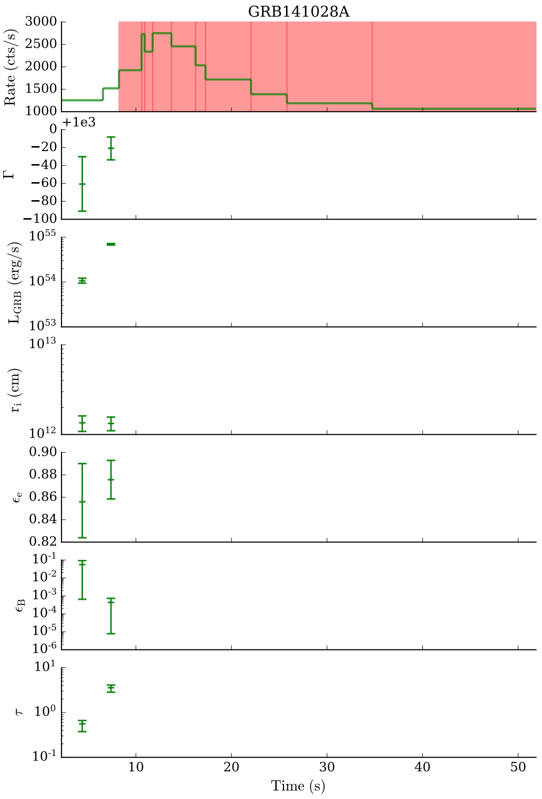
GRB141028A
Rate (cts/s)
3000
2500
2000
1500
1000
+1e3
Γ
0
−20
−40
−60
−80
−100
L_GRB (erg/s)
10^55
10^54
10^53
r_i (cm)
10^13
10^12
ε_e
0.90
0.88
0.86
0.84
0.82
ε_B
10^-1
10^-2
10^-3
10^-4
10^-5
10^-6
τ
10^1
10^0
10^-1
10
20
30
40
50
Time (s)

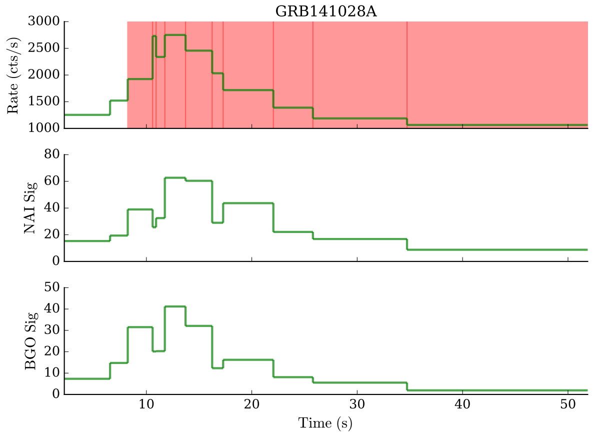
GRB141028A
Rate (cts/s)
3000
2500
2000
1500
1000
NAI Sig
80
60
40
20
0
BGO Sig
50
40
30
20
10
0
10
20
30
40
50
Time (s)

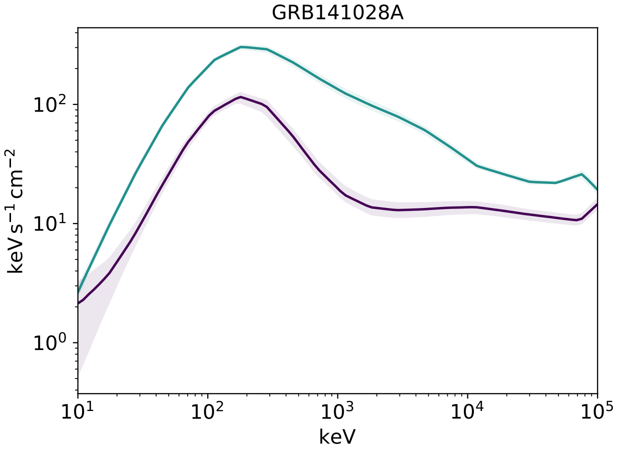
GRB141028A
keV s^-1 cm^-2
10^2
10^1
10^0
10^1
10^2
10^3
10^4
10^5
keV

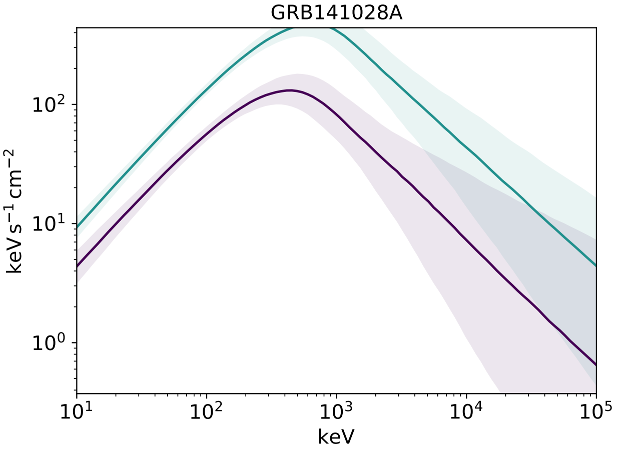
GRB141028A
keV s^-1 cm^-2
10^2
10^1
10^0
10^1
10^2
10^3
10^4
10^5
keV

Appendix C: phase space plots

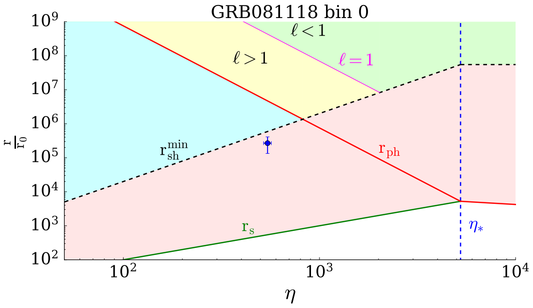
GRB081118 bin 0

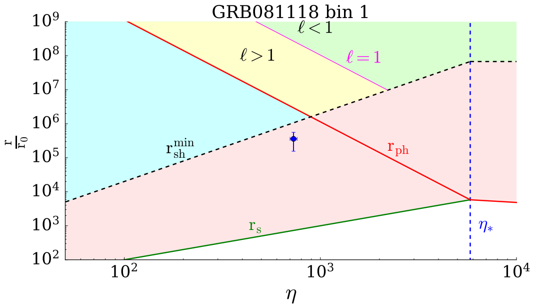
GRB081118 bin 1

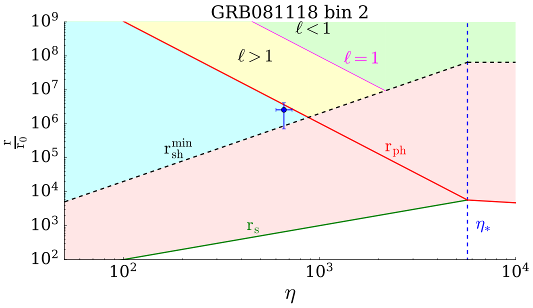
GRB081118 bin 2

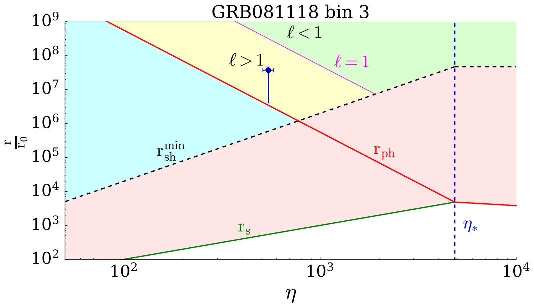
GRB081118 bin 3

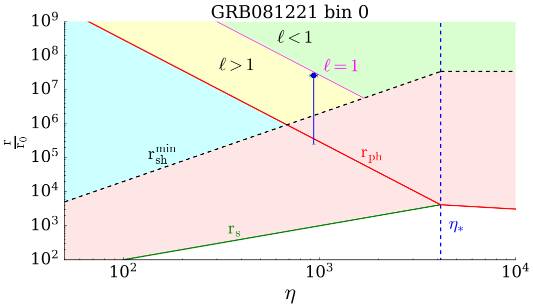
GRB081221 bin 0

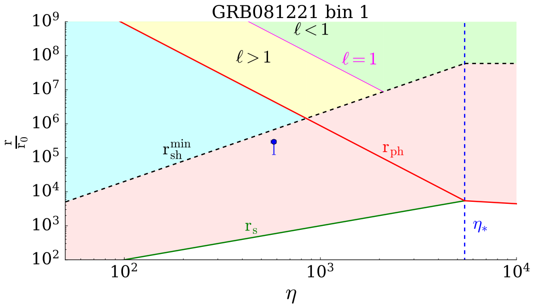
GRB081221 bin 1

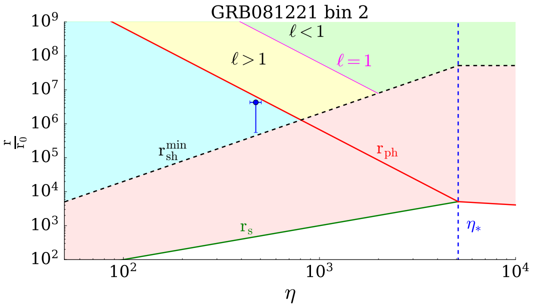
GRB081221 bin 2

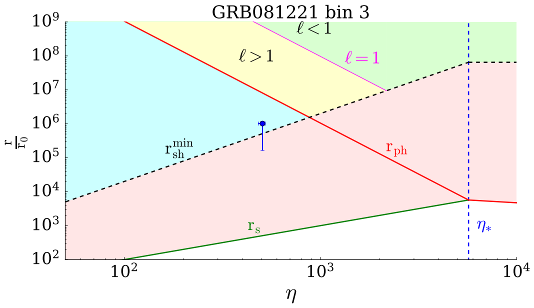
GRB081221 bin 3

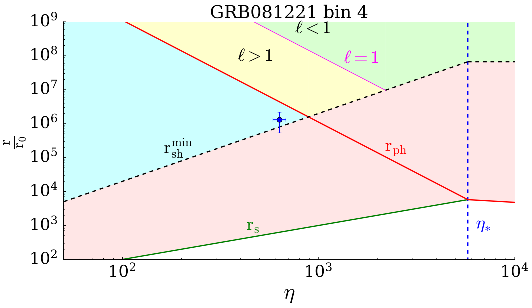
GRB081221 bin 4
$\ell<1$
$\ell>1$
$\ell=1$
r_{sh}^{min}
r_{ph}
r_s
η_*
$\frac{r}{r_0}$
η
10^2 10^3 10^4 10^5 10^6 10^7 10^8 10^9
10^2 10^3 10^4

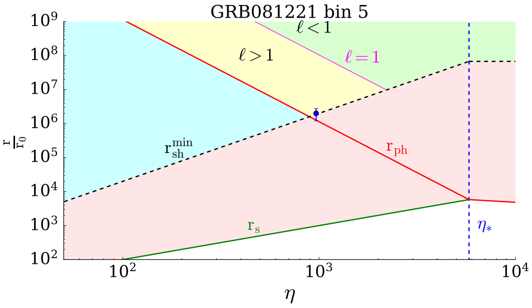
GRB081221 bin 5
$\ell<1$
$\ell>1$
$\ell=1$
r_{sh}^{min}
r_{ph}
r_s
η_*
$\frac{r}{r_0}$
η
10^2 10^3 10^4 10^5 10^6 10^7 10^8 10^9
10^2 10^3 10^4

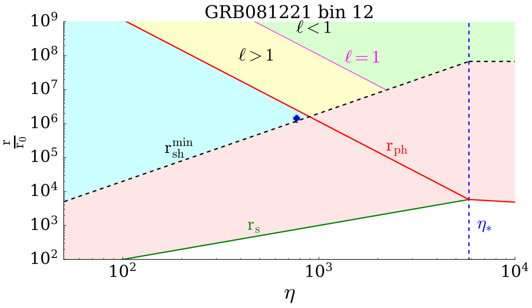
GRB081221 bin 12
$\ell<1$
$\ell>1$
$\ell=1$
r_{sh}^{min}
r_{ph}
r_s
η_*
$\frac{r}{r_0}$
η
10^2 10^3 10^4 10^5 10^6 10^7 10^8 10^9
10^2 10^3 10^4

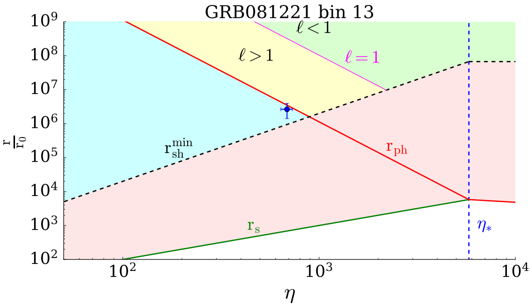
GRB081221 bin 13
$\ell<1$
$\ell>1$
$\ell=1$
r_{sh}^{min}
r_{ph}
r_s
η_*
$\frac{r}{r_0}$
η
10^2 10^3 10^4 10^5 10^6 10^7 10^8 10^9
10^2 10^3 10^4

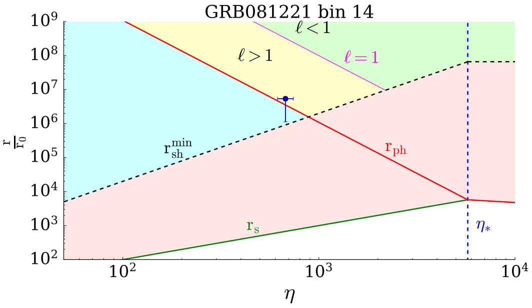
GRB081221 bin 14
$\ell<1$
$\ell>1$
$\ell=1$
r_{sh}^{min}
r_{ph}
r_s
η_*
$\frac{r}{r_0}$
η
10^2 10^3 10^4 10^5 10^6 10^7 10^8 10^9
10^2 10^3 10^4

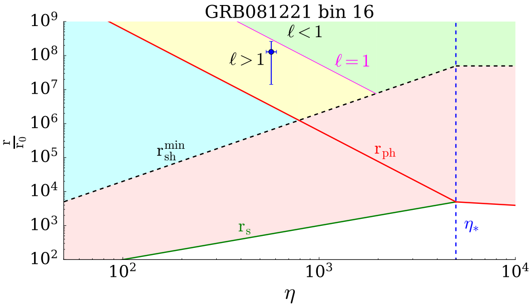
GRB081221 bin 16
$\ell<1$
$\ell>1$
$\ell=1$
r_{sh}^{min}
r_{ph}
r_s
η_*
$\frac{r}{r_0}$
η
10^2 10^3 10^4 10^5 10^6 10^7 10^8 10^9
10^2 10^3 10^4

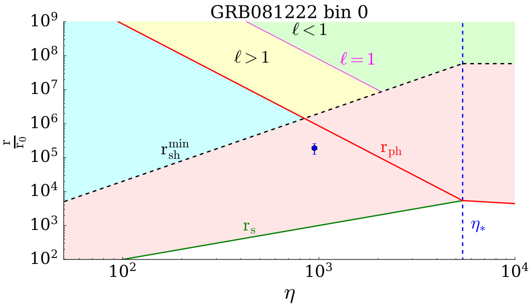
GRB081222 bin 0
$\ell<1$
$\ell>1$
$\ell=1$
r_{sh}^{min}
r_{ph}
r_s
η_*
$\frac{r}{r_0}$
η
10^2 10^3 10^4 10^5 10^6 10^7 10^8 10^9
10^2 10^3 10^4

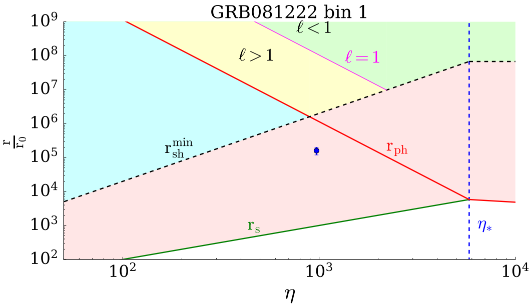
GRB081222 bin 1
$\ell<1$
$\ell>1$
$\ell=1$
r_{sh}^{min}
r_{ph}
r_s
η_*
$\frac{r}{r_0}$
η
10^2 10^3 10^4 10^5 10^6 10^7 10^8 10^9
10^2 10^3 10^4

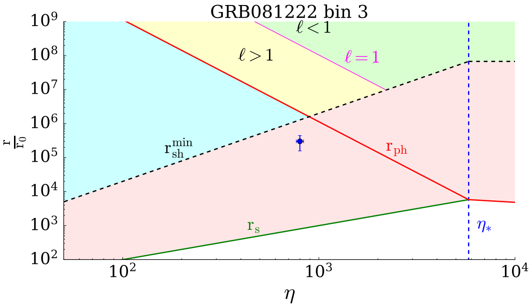
GRB081222 bin 3
$\ell<1$
$\ell>1$
$\ell=1$
r_{sh}^{min}
r_{ph}
r_s
η_*
$\frac{r}{r_0}$
η
10^2 10^3 10^4 10^5 10^6 10^7 10^8 10^9
10^2 10^3 10^4

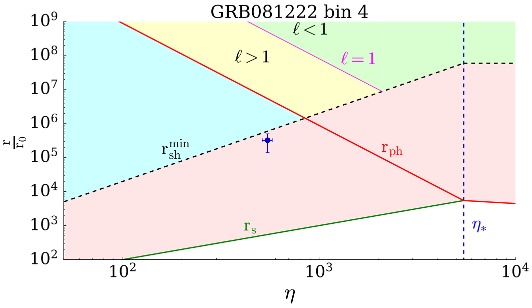
GRB081222 bin 4
$\ell<1$
$\ell>1$
$\ell=1$
r_{sh}^{min}
r_{ph}
r_s
η_*
$\frac{r}{r_0}$
η
10^2 10^3 10^4 10^5 10^6 10^7 10^8 10^9
10^2 10^3 10^4

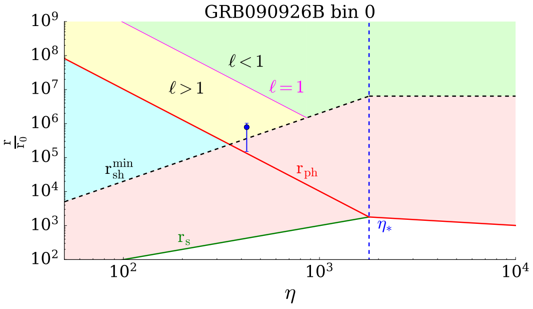
GRB090926B bin 0
10^9 10^8 10^7 10^6 10^5 10^4 10^3 10^2
$\frac{r}{r_0}$
$\ell < 1$
$\ell > 1$
$\ell = 1$
r_{sh}^{min}
r_{ph}
r_s
η_*
10^2 10^3 10^4
η

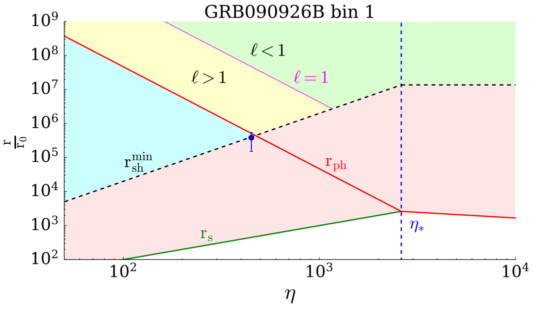
GRB090926B bin 1
10^9 10^8 10^7 10^6 10^5 10^4 10^3 10^2
$\frac{r}{r_0}$
$\ell < 1$
$\ell > 1$
$\ell = 1$
r_{sh}^{min}
r_{ph}
r_s
η_*
10^2 10^3 10^4
η

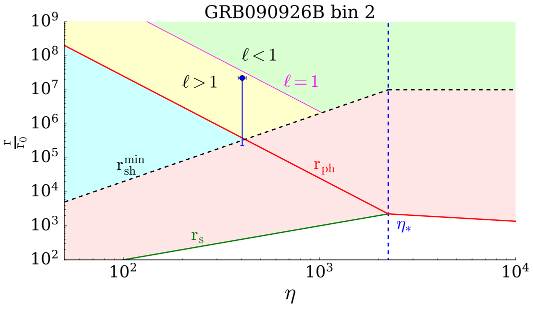
GRB090926B bin 2
10^9 10^8 10^7 10^6 10^5 10^4 10^3 10^2
$\frac{r}{r_0}$
$\ell < 1$
$\ell > 1$
$\ell = 1$
r_{sh}^{min}
r_{ph}
r_s
η_*
10^2 10^3 10^4
η

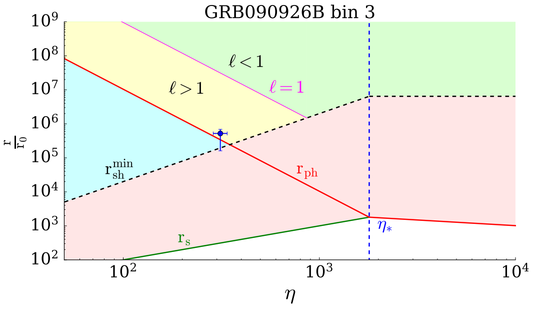
GRB090926B bin 3
10^9 10^8 10^7 10^6 10^5 10^4 10^3 10^2
$\frac{r}{r_0}$
$\ell < 1$
$\ell > 1$
$\ell = 1$
r_{sh}^{min}
r_{ph}
r_s
η_*
10^2 10^3 10^4
η

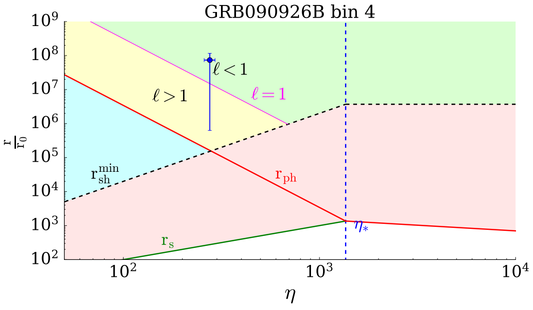
GRB090926B bin 4
10^9 10^8 10^7 10^6 10^5 10^4 10^3 10^2
$\frac{r}{r_0}$
$\ell < 1$
$\ell > 1$
$\ell = 1$
r_{sh}^{min}
r_{ph}
r_s
η_*
10^2 10^3 10^4
η

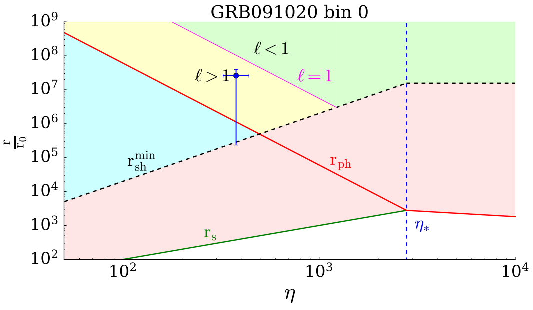
GRB091020 bin 0
10^9 10^8 10^7 10^6 10^5 10^4 10^3 10^2
$\frac{r}{r_0}$
$\ell < 1$
$\ell > 1$
$\ell = 1$
r_{sh}^{min}
r_{ph}
r_s
η_*
10^2 10^3 10^4
η

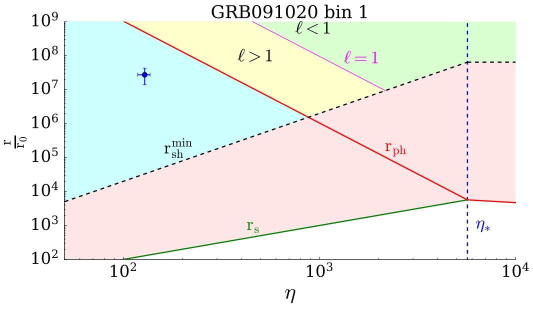
GRB091020 bin 1
10^9 10^8 10^7 10^6 10^5 10^4 10^3 10^2
$\frac{r}{r_0}$
$\ell < 1$
$\ell > 1$
$\ell = 1$
r_{sh}^{min}
r_{ph}
r_s
η_*
10^2 10^3 10^4
η

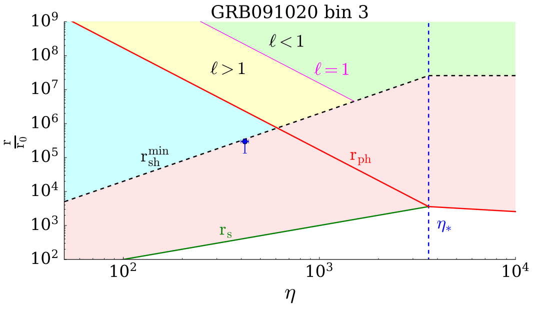
GRB091020 bin 3
10^9 10^8 10^7 10^6 10^5 10^4 10^3 10^2
$\frac{r}{r_0}$
$\ell < 1$
$\ell > 1$
$\ell = 1$
r_{sh}^{min}
r_{ph}
r_s
η_*
10^2 10^3 10^4
η

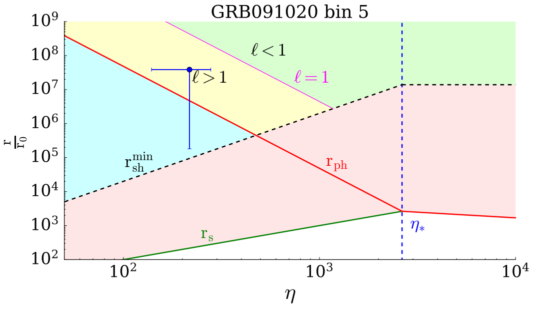
GRB091020 bin 5
10^9 10^8 10^7 10^6 10^5 10^4 10^3 10^2
$\frac{r}{r_0}$
$\ell < 1$
$\ell > 1$
$\ell = 1$
r_{sh}^{min}
r_{ph}
r_s
η_*
10^2 10^3 10^4
η

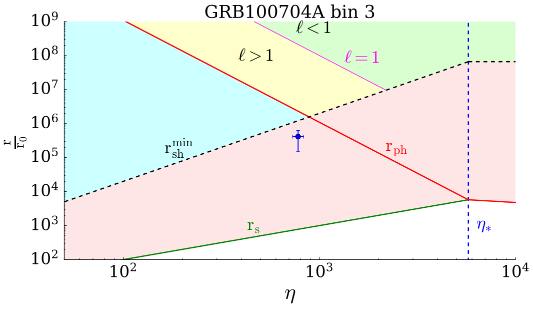
GRB100704A bin 3
10^9 10^8 10^7 10^6 10^5 10^4 10^3 10^2
$\frac{r}{r_0}$
$\ell < 1$
$\ell > 1$
$\ell = 1$
r_{sh}^{min}
r_{ph}
r_s
η_*
10^2 10^3 10^4
η

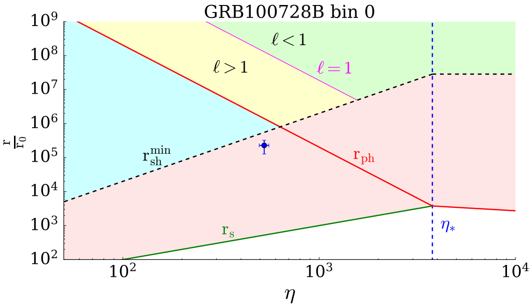
GRB100728B bin 0

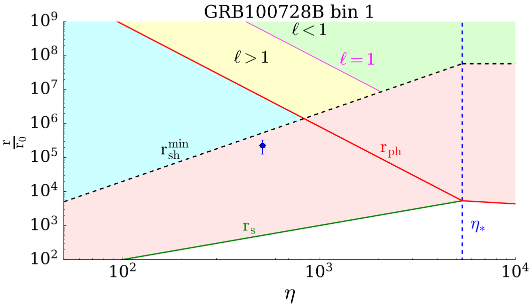
GRB100728B bin 1

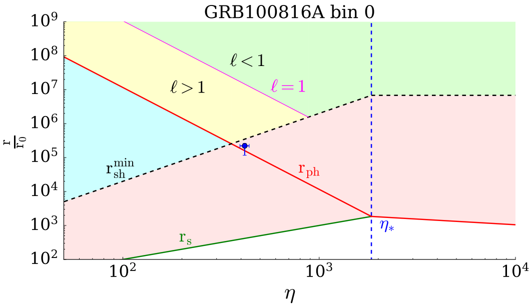
GRB100816A bin 0

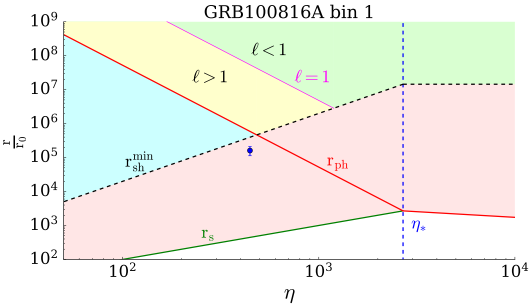
GRB100816A bin 1

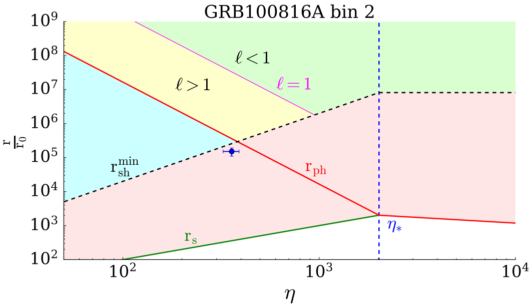
GRB100816A bin 2

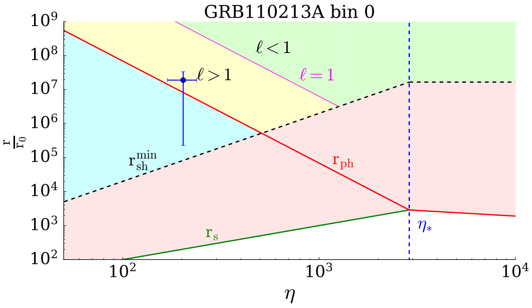
GRB110213A bin 0

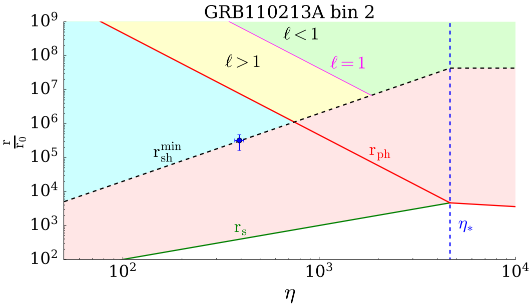
GRB110213A bin 2

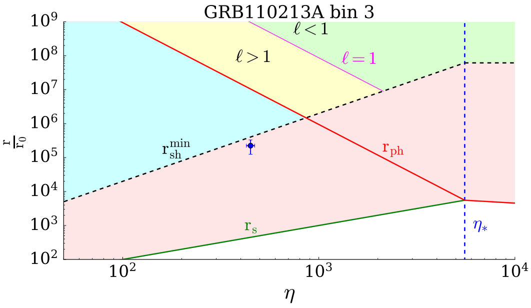
GRB110213A bin 3

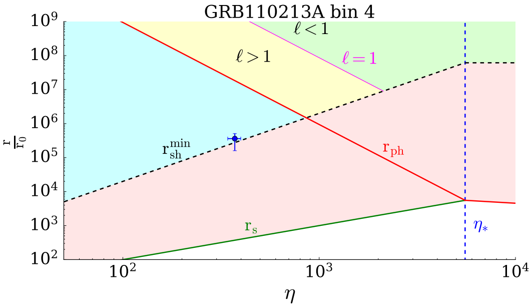
GRB110213A bin 4

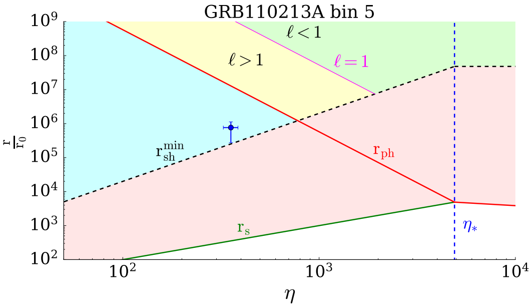
GRB110213A bin 5

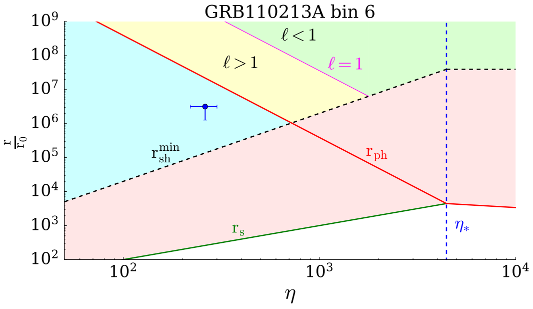
GRB110213A bin 6
$\ell<1$
$\ell>1$
$\ell=1$
r_{sh}^{min}
r_{ph}
r_s
η_*
$\frac{r}{r_0}$
η
10^2
10^3
10^4
10^5
10^6
10^7
10^8
10^9

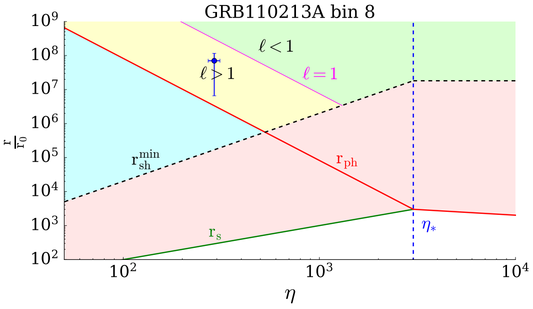
GRB110213A bin 8
$\ell<1$
$\ell>1$
$\ell=1$
r_{sh}^{min}
r_{ph}
r_s
η_*
$\frac{r}{r_0}$
η

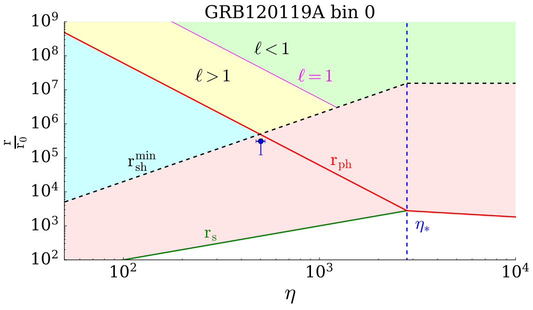
GRB120119A bin 0
$\ell<1$
$\ell>1$
$\ell=1$
r_{sh}^{min}
r_{ph}
r_s
η_*
$\frac{r}{r_0}$
η

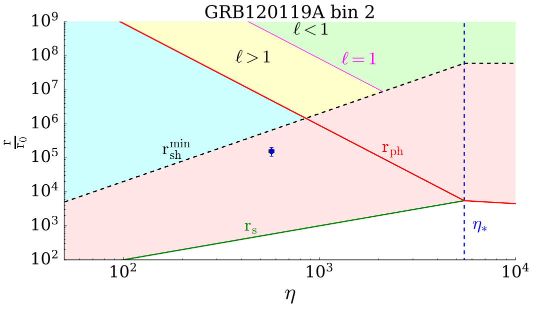
GRB120119A bin 2
$\ell<1$
$\ell>1$
$\ell=1$
r_{sh}^{min}
r_{ph}
r_s
η_*
$\frac{r}{r_0}$
η

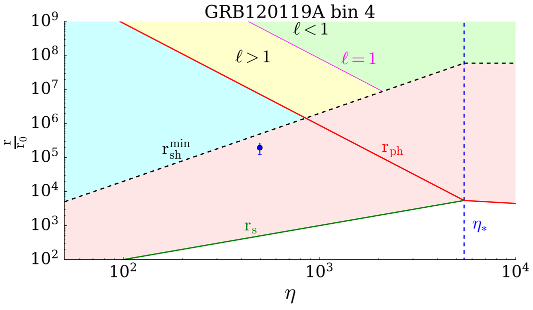
GRB120119A bin 4
$\ell<1$
$\ell>1$
$\ell=1$
r_{sh}^{min}
r_{ph}
r_s
η_*
$\frac{r}{r_0}$
η

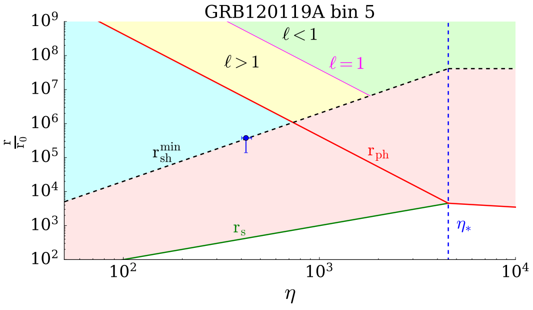
GRB120119A bin 5
$\ell<1$
$\ell>1$
$\ell=1$
r_{sh}^{min}
r_{ph}
r_s
η_*
$\frac{r}{r_0}$
η

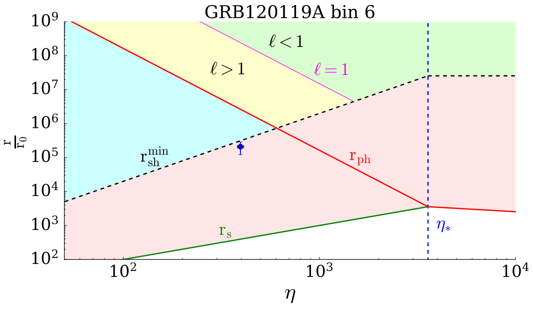
GRB120119A bin 6
$\ell<1$
$\ell>1$
$\ell=1$
r_{sh}^{min}
r_{ph}
r_s
η_*
$\frac{r}{r_0}$
η

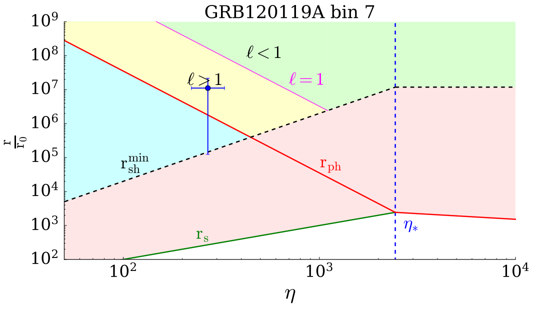
GRB120119A bin 7
$\ell<1$
$\ell>1$
$\ell=1$
r_{sh}^{min}
r_{ph}
r_s
η_*
$\frac{r}{r_0}$
η

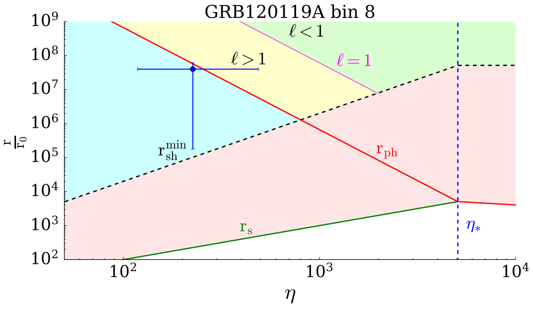
GRB120119A bin 8
$\ell<1$
$\ell>1$
$\ell=1$
r_{sh}^{min}
r_{ph}
r_s
η_*
$\frac{r}{r_0}$
η

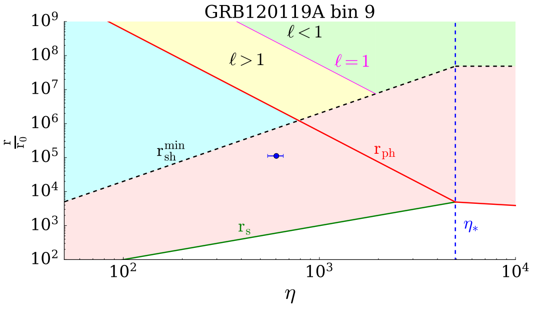
GRB120119A bin 9
$\ell<1$
$\ell>1$
$\ell=1$
r_{sh}^{min}
r_{ph}
r_s
η_*
$\frac{r}{r_0}$
η

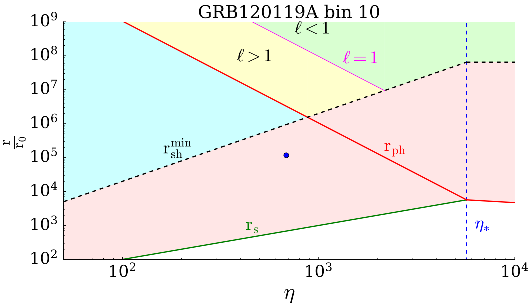
GRB120119A bin 10
$\ell<1$
$\ell>1$
$\ell=1$
r_{sh}^{min}
r_{ph}
r_s
η_*
$\frac{r}{r_0}$
η

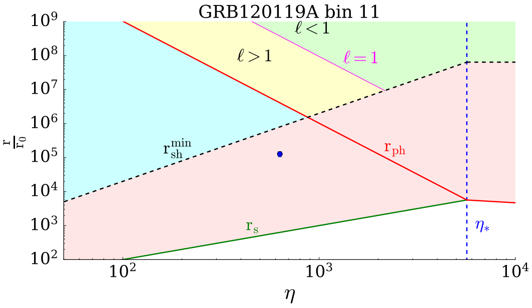
GRB120119A bin 11
$\ell<1$
$\ell>1$
$\ell=1$
r_{sh}^{min}
r_{ph}
r_s
η_*
$\frac{r}{r_0}$
η

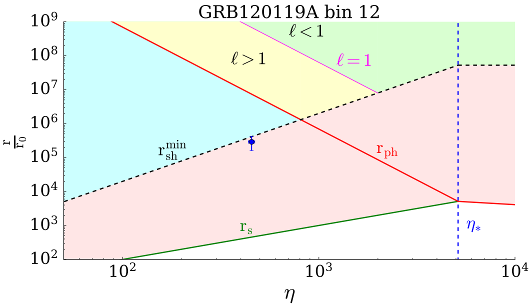
GRB120119A bin 12
$\ell<1$
$\ell>1$
$\ell=1$
r_{sh}^{min}
r_{ph}
r_s
η_*
$\frac{r}{r_0}$
η

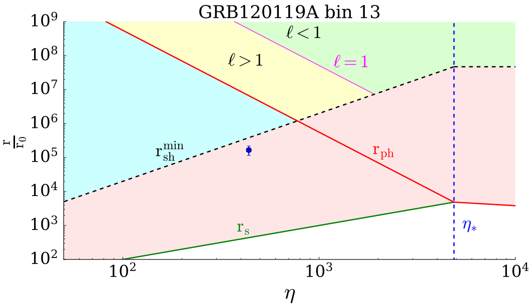
GRB120119A bin 13
$\ell<1$
$\ell>1$
$\ell=1$
r_{sh}^{min}
r_{ph}
r_s
η_*
$\frac{r}{r_0}$
η

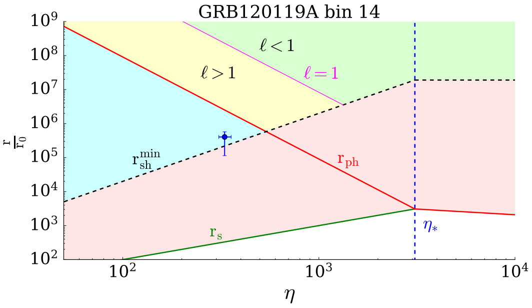
GRB120119A bin 14
$\ell<1$
$\ell>1$
$\ell=1$
r_{sh}^{min}
r_{ph}
r_s
η_*
$\frac{r}{r_0}$
η

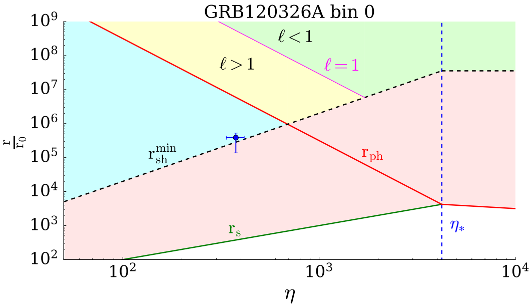
GRB120326A bin 0
$\ell<1$
$\ell>1$
$\ell=1$
r_{sh}^{min}
r_{ph}
r_s
η_*
$\frac{r}{r_0}$
η

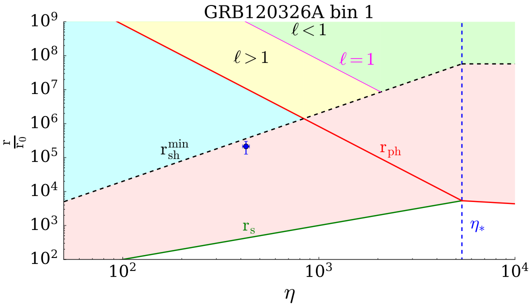
GRB120326A bin 1
$\ell<1$
$\ell>1$
$\ell=1$
r_{sh}^{min}
r_{ph}
r_s
η_*
$\frac{r}{r_0}$
η

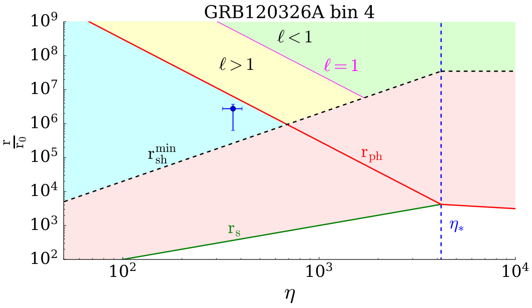
GRB120326A bin 4
$\ell<1$
$\ell>1$
$\ell=1$
r_{sh}^{min}
r_{ph}
r_s
η_*
$\frac{r}{r_0}$
η

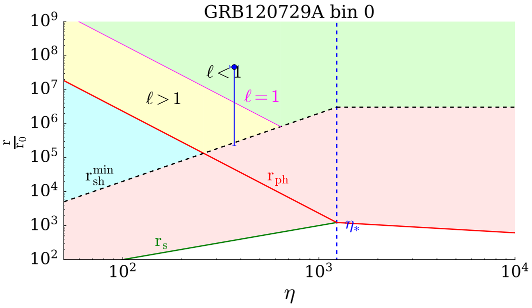
GRB120729A bin 0
$\ell<1$
$\ell>1$
$\ell=1$
r_{sh}^{min}
r_{ph}
r_s
η_*
$\frac{r}{r_0}$
η

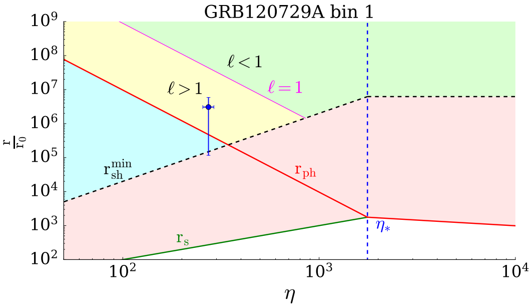
GRB120729A bin 1
$\ell<1$
$\ell>1$
$\ell=1$
r_{sh}^{min}
r_{ph}
r_s
η_*
$\frac{r}{r_0}$
η

GRB120729A bin 2

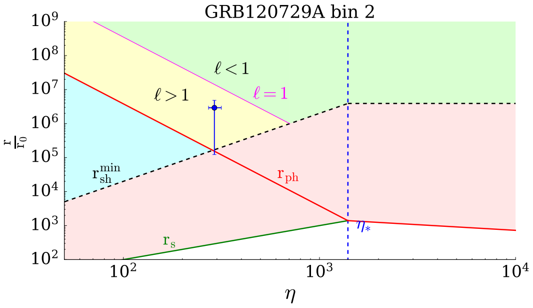

GRB120811C bin 2

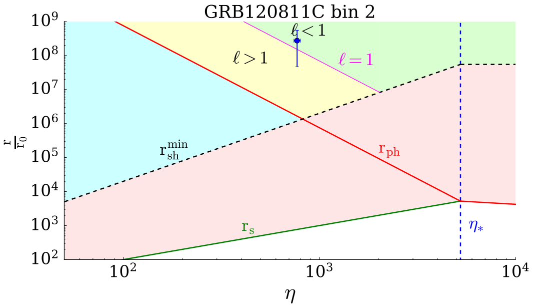

GRB131011A bin 0

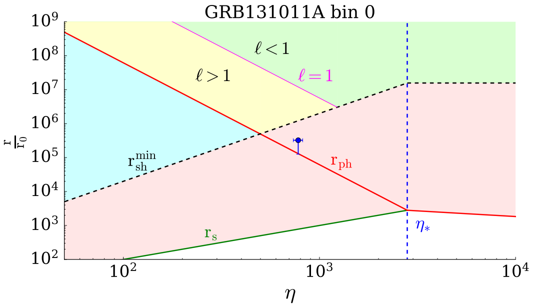

GRB131011A bin 1

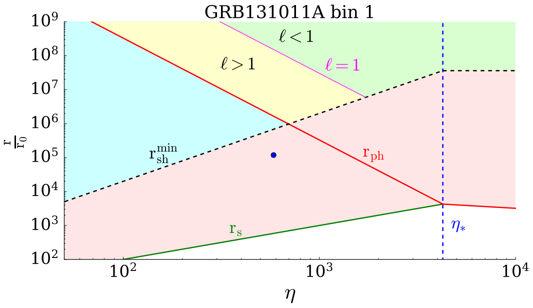

GRB131011A bin 3

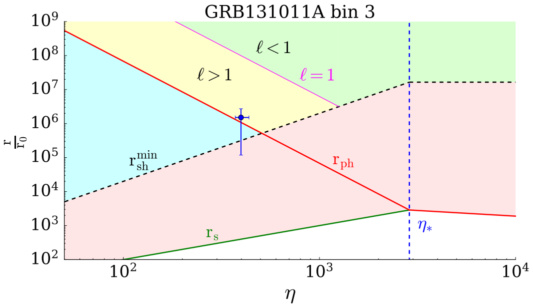

GRB140808A bin 0

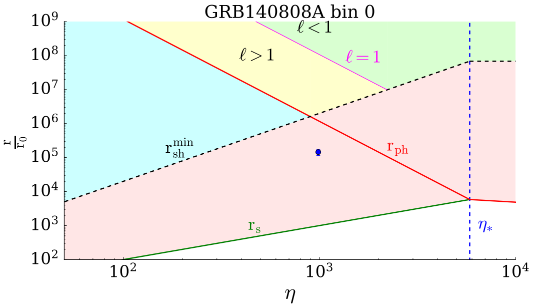

GRB140808A bin 2

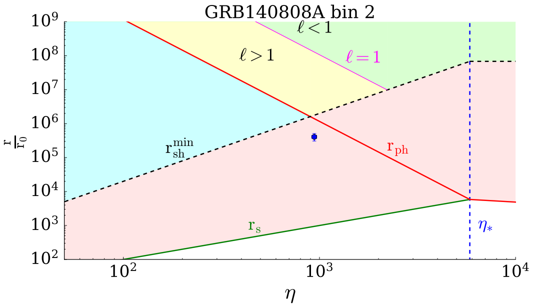

GRB140808A bin 3

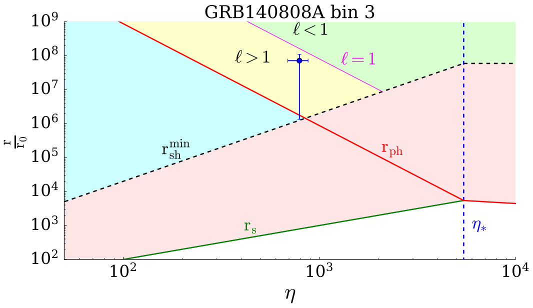

GRB141028A bin 0

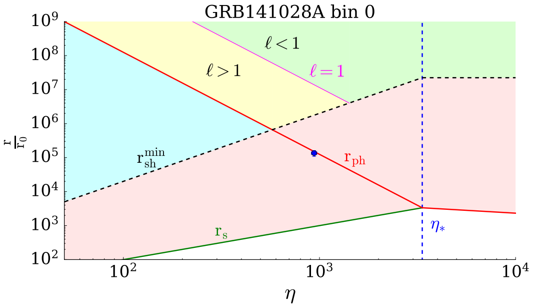

GRB141028A bin 1

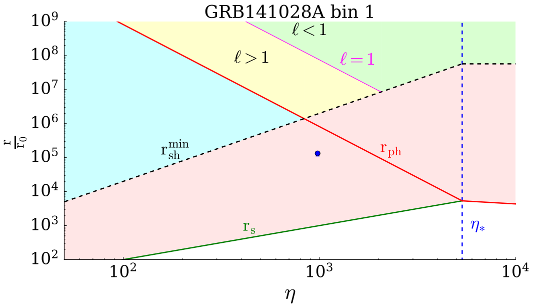

List of Figures

1.1 Examples of GRB lightcurves. 14
1.2 T_{90} distribution for Fermi-GBM. 15
1.3 Schematic of a coded aperture detector. 17
1.4 Example of IPN triangulation. 18
1.5 A schematic of a GRB. 21
1.6 Synchrotron line-of-death. 25
1.7 Example spectra for a dissipative photosphere model. 26
1.8 Effect of the optical depth on the spectral shape for a dissipative photosphere model. 27

2.1 Schematic of the Fermi LAT. 36
2.2 GBM detector array. 37
2.3 Photopeak effective area. 37
2.4 GBM response matrix. 38
2.5 GBM example lightcurve and count data. 39

3.1 Example of a corner plot. 44
3.2 Posterior predictive check example 45

4.1 Example of a BALROG posterior distribution. 49
4.2 Distribution of the systematics for DoL. 50
4.3 BALROG and DoL performance comparison. 51
4.4 Effects of statistical scatter on the localizations. 52
4.5 GRB distribution in spacecraft coordinates. 53
4.6 Standard and template BALROG performance comparison. 53
4.7 Cumulative distribution of the σ value. 54
4.8 Effects of Earth's limb on localization performance. 54
4.9 Effects of the Sun on localization performance. 55
4.10 Detector pairs performance. 55
4.11 Dependence of the localization performance on the spacecraft coordinates. 56
4.12 Dependence of the localization performance on the spacecraft's azimuth angle. 56
4.13 Polar plots for the localization performance of the different GRB subsets. 57
4.14 Performance comparison between the b0 and b1 sides of the spacecraft. . 57
4.15 Cumulative distribution for the σ level of the different GRB subsets. . . . 58
4.16 Global offset distribution. 58
4.17 Comparison between real and simulated datasets. 59
4.18 Systematics and corrections to the cumulative distribution of the σ level. . 60
4.19 Systematics and size of the error region. 60
4.20 Cumulative distribution function of the automated BALROG locations. . . 61
4.21 Impact of wrongly reconstructed locations on E_{peak}. 62

5.1 Spectrum of GRB 090902B. 64
5.2 Marginal distributions for the parameters of a simulated spectrum. 66
5.3 Normalized PPC plot examples. 69
5.4 Example results of the model fits. 70
5.5 Distribution of the optical depth for the fitted spectra. 71
5.6 Histograms displaying the significance for accepted and rejected fits. . . . 71
5.7 Distribution of the fitted parameters. 72
5.8 Distribution of the observed bolometric luminosity and its relation to the luminosity of the fireball. 73
5.9 Distribution of the fitted parameters depending on the luminosity. 73
5.10 Distribution of the fitted parameters depending on the optical depth. . . . 74
5.11 $\Gamma - L_{GRB}$ scatterplot. 75
5.12 $\tau - r_d$ scatterplot. 76
5.13 Global distribution for the photospheric radius. 77
5.14 Example of a $\eta - r/r_0$ phase space diagram. 78
5.15 Distribution of the fit results in the $\eta - r/r_0$ phase space diagram. 79
5.16 Parameter distributions from Ahlgren et al. (2019b). 81

List of Tables

2.1 GBM data products. 39

4.1 DoL spectral templates. 48

5.1 Fit results for a simulated spectrum. 66
5.2 The GRB sample used for the fits. Bursts with LLE data are marked with an asterisk. 68
5.3 List with the analyzed GRBs. 85

Bibliography

Aartsen, M. G. et al. “An All-sky Search for Three Flavors of Neutrinos from Gamma-ray Bursts with the IceCube Neutrino Observatory.” ApJ, 824(2):115 (2016).

Aartsen, M. G. et al. “The IceCube Neutrino Observatory: instrumentation and online systems.” *Journal of Instrumentation*, 12(3):P03012 (2017).

Abbott, B. P. et al. “Observation of gravitational waves from a binary black hole merger.” *Phys. Rev. Lett.*, 116:061102 (2016).

Abbott, B. P. et al. “Gravitational Waves and Gamma-Rays from a Binary Neutron Star Merger: GW170817 and GRB 170817A.” ApJ, 848:L13 (2017).

Abdo, A. A. et al. “Fermi Observations of GRB 090902B: A Distinct Spectral Component in the Prompt and Delayed Emission.” ApJ, 706(1):L138–L144 (2009).

Ackermann, M. et al. “The First Fermi-LAT Gamma-Ray Burst Catalog.” ApJS, 209(1):11 (2013).

Ahlgren, B., Larsson, J., Nymark, T., Ryde, F. and Pe’er, A. “Confronting GRB prompt emission with a model for subphotospheric dissipation.” MNRAS, 454(1):L31–L35 (2015).

Ahlgren, B. et al. “Investigating Subphotospheric Dissipation in Gamma-Ray Bursts Using Joint Fermi-Swift Observations.” ApJ, 880(2):76 (2019a).

Ahlgren, B. et al. “Testing a model for subphotospheric dissipation in GRBs: fits to Fermi data constrain the dissipation scenario.” MNRAS, 485(1):474–497 (2019b).

Ajello, M. et al. “A Decade of Gamma-Ray Bursts Observed by Fermi-LAT: The Second GRB Catalog.” ApJ, 878(1):52 (2019).

Andrae, R., Schulze-Hartung, T. and Melchior, P. “Dos and don’ts of reduced chi-squared.” (2010).

Ascenzi, S. et al. “A luminosity distribution for kilonovae based on short gamma-ray burst afterglows.” MNRAS, 486(1):672–690 (2019).

Atwood, W. B. et al. “The Large Area Telescope on the Fermi Gamma-Ray Space Telescope Mission.” ApJ, 697(2):1071–1102 (2009).

Band, D. et al. “BATSE Observations of Gamma-Ray Burst Spectra. I. Spectral Diversity.” ApJ, 413:281 (1993).

Barthelmy, S. D. et al. “The Burst Alert Telescope (BAT) on the SWIFT Midex Mission.” Space Sci. Rev., 120:143–164 (2005).

Bégué, D., Burgess, J. M. and Greiner, J. “The Peculiar Physics of GRB 170817A and Their Implications for Short GRBs.” ApJ, 851(1):L19 (2017).

Beloborodov, A. M. “Collisional mechanism for gamma-ray burst emission.” *Monthly Notices of the Royal Astronomical Society*, 407(2):1033–1047 (2010).

Beloborodov, A. M. and Mészáros, P. “Photospheric Emission of Gamma-Ray Bursts.” Space Sci. Rev., 207(1-4):87–110 (2017).

Berlato, F., Greiner, J. and Burgess, J. M. “Improved Fermi-GBM GRB Localizations Using BALROG.” ApJ, 873(1):60 (2019).

Betancourt, M. “A conceptual introduction to hamiltonian monte carlo.” (2017).

Bissaldi, E. et al. “Ground-based calibration and characterization of the Fermi gamma-ray burst monitor detectors.” *Experimental Astronomy*, 24(1-3):47–88 (2009).

Blandford, R. D. and McKee, C. F. “Fluid dynamics of relativistic blast waves.” *Physics of Fluids*, 19:1130–1138 (1976).

Burgess, J. M. “Is spectral width a reliable measure of GRB emission physics?” A&A, 629:A69 (2019).

Burgess, J. M., Ryde, F. and Yu, H.-F. “Taking the band function too far: a tale of two α’s.” MNRAS, 451(2):1511–1521 (2015).

Burgess, J. M., Yu, H.-F., Greiner, J. and Mortlock, D. J. “Awakening the BALROG: BAyesian Location Reconstruction Of GRBs.” MNRAS, 476(2):1427–1444 (2018).

Burgess, J. M. et al. “Time-resolved GRB polarization with POLAR and GBM. Simultaneous spectral and polarization analysis with synchrotron emission.” A&A, 627:A105 (2019).

Burgess, J. M. et al. “Gamma-ray bursts as cool synchrotron sources.” *Nature Astronomy*, 4:174–179 (2020).

Burrows, A. and Lattimer, J. M. “Neutrinos from SN 1987A.” ApJ, 318:L63 (1987).

Burrows, D. N. et al. “The swift x-ray telescope: status and performance.” In “UV, X-Ray, and Gamma-Ray Space Instrumentation for Astronomy XV,” volume 6686 of Proc. SPIE, page 668607 (2007).

Connaughton, V. et al. “Localization of Gamma-Ray Bursts Using the Fermi Gamma-Ray Burst Monitor.” ApJS, 216(2):32 (2015).

Coppin, P. and van Eijndhoven, N. “IceCube Search for High-Energy Neutrinos Produced in the Precursor Stages of Gamma-ray Bursts.” In “36th International Cosmic Ray Conference (ICRC2019),” volume 36 of *International Cosmic Ray Conference*, page 859 (2019).

Coroniti, F. V. “Magnetically Striped Relativistic Magnetohydrodynamic Winds: The Crab Nebula Revisited.” ApJ, 349:538 (1990).

Costa, E. et al. “Discovery of an X-ray afterglow associated with the γ-ray burst of 28 February 1997.” Nature, 387(6635):783–785 (1997).

Dermer, C. D. and Menon, G. *High Energy Radiation from Black Holes: Gamma Rays, Cosmic Rays, and Neutrinos* (2009).

Dicke, R. H. “Scatter-Hole Cameras for X-Rays and Gamma Rays.” ApJ, 153:L101 (1968).

Eichler, D., Livio, M., Piran, T. and Schramm, D. N. “Nucleosynthesis, neutrino bursts and γ-rays from coalescing neutron stars.” Nature, 340(6229):126–128 (1989).

Feroz, F., Hobson, M. and Bridges, M. “MultiNest: an efficient and robust Bayesian inference tool for cosmology and particle physics.” *Mon. Not. Roy. Astron. Soc.*, 398:1601–1614 (2009).

Fishman, G. J. and Meegan, C. A. “Gamma-Ray Bursts.” ARA&A, 33:415–458 (1995).

Gabry, J., Simpson, D., Vehtari, A., Betancourt, M. and Gelman, A. “Visualization in bayesian workflow.” *J. R. Stat. Soc. A*, 182:389–402 (2019).

Galama, T. J. et al. “On the possible association of SN 1998bw and GRB 980425.” A&AS, 138:465–466 (1999).

Gehrels, N. and Mészáros, P. “Gamma-Ray Bursts.” *Science*, 337(6097):932 (2012).

Gelman, A. “A bayesian formulation of exploratory data analysis and goodness-of-fit testing*.” *International Statistical Review*, 71(2):369–382 (2003).

Giannios, D. “Prompt emission spectra from the photosphere of a GRB.” A&A, 457(3):763–770 (2006).

Giannios, D. and Spruit, H. C. “The role of kink instability in Poynting-flux dominated jets.” A&A, 450(3):887–898 (2006).

Gill, R., Granot, J. and Kumar, P. “Linear polarization in gamma-ray burst prompt emission.” MNRAS, 491(3):3343–3373 (2020).

Goldstein, A. et al. “An Ordinary Short Gamma-Ray Burst with Extraordinary Implications: Fermi-GBM Detection of GRB 170817A.” ApJ, 848(2):L14 (2017).

Goldstein, A. et al. “Evaluation of Automated Fermi GBM Localizations of Gamma-ray Bursts.” *arXiv e-prints*, arXiv:1909.03006 (2019).

Golkhou, V. Z., Butler, N. R. and Littlejohns, O. M. “The Energy Dependence of GRB Minimum Variability Timescales.” ApJ, 811(2):93 (2015).

Goodman, J. “Are gamma-ray bursts optically thick?” ApJ, 308:L47 (1986).

Gottlieb, O., Nakar, E., Piran, T. and Hotokezaka, K. “A cocoon shock breakout as the origin of the γ-ray emission in GW170817.” MNRAS, 479(1):588–600 (2018).

Granot, J. “Gamma-Ray Bursts from Magnetic Reconnection: Variability and Robustness of Light Curves.” ApJ, 816(2):L20 (2016).

Greiner, J. et al. “A very luminous magnetar-powered supernova associated with an ultra-long γ-ray burst.” Nature, 523(7559):189–192 (2015).

Harrison, F. A. et al. “Optical and Radio Observations of the Afterglow from GRB 990510: Evidence for a Jet.” ApJ, 523(2):L121–L124 (1999).

Heise, J., Zand, J. I., Kippen, R. M. and Woods, P. M. “X-Ray Flashes and X-Ray Rich Gamma Ray Bursts.” In E. Costa, F. Frontera and J. Hjorth, editors, “Gamma-ray Bursts in the Afterglow Era,” page 16 (2001).

Hjorth, J. et al. “A very energetic supernova associated with the γ-ray burst of 29 March 2003.” Nature, 423(6942):847–850 (2003).

Hurley, K. et al. "The Interplanetary Network Supplement to the Fermi GBM Catalog of Cosmic Gamma-Ray Bursts." ApJS, 207(2):39 (2013).

IceCube Collaboration et al. "Neutrino emission from the direction of the blazar TXS 0506+056 prior to the IceCube-170922A alert." *Science*, 361(6398):147–151 (2018).

Kasliwal, M. M. et al. "Illuminating gravitational waves: A concordant picture of photons from a neutron star merger." *Science*, 358(6370):1559–1565 (2017).

Katz, J. I. "Low-Frequency Spectra of Gamma-Ray Bursts." ApJ, 432:L107 (1994).

Kippen, R. M. et al. "Instrument Response Modeling and Simulation for the GLAST Burst Monitor." In S. Ritz, P. Michelson and C. A. Meegan, editors, "The First GLAST Symposium," volume 921 of *American Institute of Physics Conference Series*, pages 590–591 (2007).

Kirk, J. G., Guthmann, A. W., Gallant, Y. A. and Achterberg, A. "Particle acceleration at ultrarelativistic shocks: An eigenfunction method." *The Astrophysical Journal*, 542(1):235–242 (2000).

Kobayashi, S., Piran, T. and Sari, R. "Can Internal Shocks Produce the Variability in Gamma-Ray Bursts?" ApJ, 490:92 (1997).

Kouveliotou, C. et al. "Identification of Two Classes of Gamma-Ray Bursts." ApJ, 413:L101 (1993).

Levan, A. J. et al. "A New Population of Ultra-long Duration Gamma-Ray Bursts." ApJ, 781(1):13 (2014).

Li, L.-X. and Paczyński, B. "Transient Events from Neutron Star Mergers." ApJ, 507(1):L59–L62 (1998).

Li, T. P. and Ma, Y. Q. "Analysis methods for results in gamma-ray astronomy." ApJ, 272:317–324 (1983).

MAGIC Collaboration et al. "Teraelectronvolt emission from the γ-ray burst GRB 190114C." *arXiv e-prints*, arXiv:2006.07249 (2020).

Medvedev, M. V. "Theory of "Jitter" Radiation from Small-Scale Random Magnetic Fields and Prompt Emission from Gamma-Ray Burst Shocks." ApJ, 540(2):704–714 (2000).

Meegan, C. et al. "The Fermi Gamma-ray Burst Monitor." ApJ, 702(1):791–804 (2009).

Meegan, C. A. et al. "Spatial distribution of γ-ray bursts observed by BATSE." Nature, 355(6356):143–145 (1992).

Mészáros, P. "Gamma-ray bursts." *Reports on Progress in Physics*, 69(8):2259–2321 (2006).

Mészáros, P. "Gamma Ray Bursts as Neutrino Sources." *arXiv e-prints*, arXiv:1511.01396 (2015).

Mészáros, P. and Rees, M. J. "Steep Slopes and Preferred Breaks in Gamma-Ray Burst Spectra: The Role of Photospheres and Comptonization." ApJ, 530(1):292–298 (2000).

Metzger, B. D. et al. "Electromagnetic counterparts of compact object mergers powered by the radioactive decay of r-process nuclei." MNRAS, 406(4):2650–2662 (2010).

Metzger, M. R. et al. “Spectral constraints on the redshift of the optical counterpart to the γ-ray burst of 8 May 1997.” Nature, 387(6636):878–880 (1997).

Mochkovitch, R., Maitia, V. and Marques, R. “Internal Shocks in a Relativistic Wind as a Source for Gamma-Ray Bursts?” Ap&SS, 231(1-2):441–444 (1995).

Narayan, R., Paczynski, B. and Piran, T. “Gamma-Ray Bursts as the Death Throes of Massive Binary Stars.” ApJ, 395:L83 (1992).

Narayana Bhat, P. et al. “The Third Fermi GBM Gamma-Ray Burst Catalog: The First Six Years.” ApJS, 223(2):28 (2016).

Nir, G., Guetta, D., Landsman, H. and Behar, E. “Ultra-high Energy Neutrinos from Gamma-Ray Burst Afterglows Using the Swift-UVOT Data.” ApJ, 817(2):142 (2016).

Paciesas, W. S. et al. “The Fermi GBM Gamma-Ray Burst Catalog: The First Two Years.” ApJS, 199:18 (2012).

Paczynski, B. “Gamma-ray bursters at cosmological distances.” ApJ, 308:L43–L46 (1986).

Paczynski, B. and Rhoads, J. E. “Radio Transients from Gamma-Ray Bursters.” ApJ, 418:L5 (1993).

Paczynski, B. and Xu, G. “Neutrino Bursts from Gamma-Ray Bursts.” ApJ, 427:708 (1994).

Pe’er, A. “Physics of Gamma-Ray Bursts Prompt Emission.” *Advances in Astronomy*, 2015:907321 (2015).

Pe’er, A. and Ryde, F. “Photospheric emission in gamma-ray bursts.” *International Journal of Modern Physics D*, 26(10):1730018-296 (2017).

Pe’er, A. and Waxman, E. “Time-dependent Numerical Model for the Emission of Radiation from Relativistic Plasma.” ApJ, 628(2):857–866 (2005).

Pe’Er, A. et al. “The connection between thermal and non-thermal emission in gamma-ray bursts: general considerations and GRB 090902B as a case study.” MNRAS, 420(1):468–482 (2012).

Pelassa, V., Preece, R., Piron, F., Omodei, N. and Guiriec, S. “The LAT Low-Energy technique for Fermi Gamma-Ray Bursts spectral analysis.” *arXiv e-prints*, arXiv:1002.2617 (2010).

Piran, T. “Gamma-ray bursts and the fireball model.” Phys. Rep., 314(6):575–667 (1999).

Piran, T. “The physics of gamma-ray bursts.” *Reviews of Modern Physics*, 76(4):1143–1210 (2004).

Piran, T. and Granot, J. “Theory of GRB Afterglow.” In E. Costa, F. Frontera and J. Hjorth, editors, “Gamma-ray Bursts in the Afterglow Era,” page 300 (2001).

Planck Collaboration et al. “Planck 2018 results. VI. Cosmological parameters.” *arXiv e-prints*, arXiv:1807.06209 (2018).

Preece, R. D. et al. “The Synchrotron Shock Model Confronts a “Line of Death” in the BATSE Gamma-Ray Burst Data.” ApJ, 506(1):L23–L26 (1998).

Produit, N. et al. “Design and construction of the POLAR detector.” *Nuclear Instruments and Methods in Physics Research A*, 877:259–268 (2018).

Rees, M. J. and Meszaros, P. “Relativistic fireballs - Energy conversion and time-scales.” MNRAS, 258:41 (1992).

Rees, M. J. and Meszaros, P. “Unsteady Outflow Models for Cosmological Gamma-Ray Bursts.” ApJ, 430:L93 (1994).

Roming, P. W. A. et al. “The Swift Ultra-Violet/Optical Telescope (UVOT).” In E. Fenimore and M. Galassi, editors, “Gamma-Ray Bursts: 30 Years of Discovery,” volume 727 of *American Institute of Physics Conference Series*, pages 651–654 (2004).

Sari, R., Piran, T. and Narayan, R. “Spectra and Light Curves of Gamma-Ray Burst Afterglows.” ApJ, 497(1):L17–L20 (1998a).

Sari, R., Piran, T. and Narayan, R. “Spectra and Light Curves of Gamma-Ray Burst Afterglows.” ApJ, 497(1):L17–L20 (1998b).

Sari, R., Piran, T. and Narayan, R. “Spectra and Light Curves of Gamma-Ray Burst Afterglows.” ApJ, 497(1):L17–L20 (1998c).

Scargle, J. D., Norris, J. P., Jackson, B. and Chiang, J. “Studies in Astronomical Time Series Analysis. VI. Bayesian Block Representations.” ApJ, 764(2):167 (2013).

Sironi, L. and Spitkovsky, A. “Relativistic Reconnection: An Efficient Source of Nonthermal Particles.” ApJ, 783(1):L21 (2014).

Soares-Santos, M. et al. “The Electromagnetic Counterpart of the Binary Neutron Star Merger LIGO/Virgo GW170817. I. Discovery of the Optical Counterpart Using the Dark Energy Camera.” ApJ, 848(2):L16 (2017).

Stanek, K. Z. et al. “Spectroscopic Discovery of the Supernova 2003dh Associated with GRB 030329.” ApJ, 591(1):L17–L20 (2003).

Svinkin, Dmitry. “IPN triangulation of GRB 190720A.” (????).

Tanvir, N. R. et al. “A ‘kilonova’ associated with the short-duration γ-ray burst GRB 130603B.” Nature, 500(7464):547–549 (2013).

Tavani, M. “A Shock Emission Model for Gamma-Ray Bursts. II. Spectral Properties.” ApJ, 466:768 (1996).

Thomas, J. K., Moharana, R. and Razzaque, S. “Ultrahigh energy neutrino afterglows of nearby long duration gamma-ray bursts.” Phys. Rev. D, 96(10):103004 (2017).

Thompson, C. “A model of gamma-ray bursts.” MNRAS, 270:480–498 (1994).

Troja, E. et al. “A luminous blue kilonova and an off-axis jet from a compact binary merger at z=0.1341.” *Nature Commun.*, 9:4089 (2018).

Usov, V. V. “Millisecond pulsars with extremely strong magnetic fields as a cosmological source of γ-ray bursts.” Nature, 357(6378):472–474 (1992).

Vianello, G. “The Significance of an Excess in a Counting Experiment: Assessing the Impact of Systematic Uncertainties and the Case with a Gaussian Background.” ApJS, 236(1):17 (2018).

von Kienlin, A. et al. “The Second Fermi GBM Gamma-Ray Burst Catalog: The First Four Years.” ApJS, 211:13 (2014).

von Kienlin, A. et al. “The 4th Fermi-GBM Gamma-Ray Burst Catalog: A Decade of Data.” *arXiv e-prints*, arXiv:2002.11460 (2020).

von Minckwitz, N. “The Accuracy of Gamma Ray Burst Spectra.” (2020).

Vurm, I. and Beloborodov, A. M. “Radiative Transfer Models for Gamma-Ray Bursts.” ApJ, 831(2):175 (2016).

Waxman, E. and Bahcall, J. N. “Neutrino Afterglow from Gamma-Ray Bursts: $\sim 10^{18}$ EV.” ApJ, 541(2):707–711 (2000).

Wilk, M. B. and Gnanadesikan, R. “Probability plotting methods for the analysis of data.” *Biometrika*, 55(1):1–17 (1968).

Yonetoku, D. et al. “Gamma-Ray Burst Polarimeter (GAP) aboard the Small Solar Power Sail Demonstrator IKAROS.” PASJ, 63:625 (2011).

Yonetoku, D. et al. “Magnetic Structures in Gamma-Ray Burst Jets Probed by Gamma-Ray Polarization.” ApJ, 758(1):L1 (2012).

Zhang, B. and Yan, H. “The Internal-collision-induced Magnetic Reconnection and Turbulence (ICMART) Model of Gamma-ray Bursts.” ApJ, 726(2):90 (2011).

Zhang, H., Christie, I. M., Petropoulou, M., Rueda-Becerril, J. M. and Giannios, D. “Inverse Compton signatures of gamma-ray burst afterglows.” MNRAS, 496(1):974–986 (2020).